

CMS Draft Analysis Note

The content of this note is intended for CMS internal use and distribution only

2016/09/09

Head Id: 366206

Archive Id: 344565:366615M

Archive Date: 2016/09/02

Archive Tag: trunk

Search for heavy resonances decaying to top and vector-like quarks in the all hadronic channel at 13 TeV

Emanuele Usai, Ivan Marchesini, and Alexander Schmidt
University of Hamburg

Abstract

Many models predicting a heavy neutral spin-1 resonance also predict the existence of vector-like quarks. A hypothetical resonance might then predominantly decay to these heavy quark partners rather than SM particles.

We present a search for a Z' heavy resonance decaying in a top and a heavy vector-like top partner (T'). The analysis is tailored for the final state where the T' decays in a W boson and a b quark. We focus on the all hadronic channel where both the top and the W quark coming from the T' decay hadronically.

In this kind of searches, the decay products of the top quark and the W boson are highly boosted and cannot be reconstructed as separate jets. Top and boson tagging algorithms are then used to reconstruct the decays.

Jet substructure tools, in addition to b -tagging in boosted topologies, are employed to reduce the QCD multijet background and improve the sensitivity of the analysis.

This box is only visible in draft mode. Please make sure the values below make sense.

PDFAuthor: Emanuele Usai, Iven Marchesini, Alexander Schmidt
PDFTitle: Search for heavy resonances decaying to top and vector-like quarks in the all hadronic channel at 13 TeV
PDFSubject: CMS
PDFKeywords: CMS, physics, heavy boson, vector-like quarks

Please also verify that the abstract does not use any user defined symbols

1 **Contents**

2	1	Introduction	2
3	2	Samples	4
4	3	Selection	10
5	3.1	Primary Vertex	10
6	3.2	Pileup	10
7	3.3	Object IDs	10
8	3.4	Trigger	12
9	3.5	Final selection	13
10	4	Background estimate	26
11	4.1	Top background estimate	26
12	4.2	Non-top background estimate	26
13	5	Systematics	35
14	6	Results	36
15	A	Signal region with other signal samples	50
16	B	Crosschecks	50

DRAFT

1 Introduction

- Many models of new physics predict heavy spin-1 resonances (Z') which have enhanced couplings to the third generation of the Standard Model (SM). These models often predicts the existence of heavy vector-like quarks along with the heavy resonances. In such cases the decay modes of the spin-1 particle to vector-like quarks or vector-like quarks and third generation quarks can be enhanced as well.
- Traditionally, heavy resonance searches focus on SM decay modes. However, depending on the coupling parameters and on the particle's masses, the decay modes containing at least a vector-like quark might be the dominant ones. Hence the need to explore these non-SM decay modes of heavy resonances with dedicated searches like this one.
- Examples of these models are little Higgs models, models with extra dimensions, and composite Higgs models. In addition to these models, these features are often included in many effective lagrangian frameworks trying to parametrize the effect of higher energy physics in terms of a reduced amount of additional particles and couplings.
- A distinctive property of vector-like quarks is that their left-handed and right-handed components transform in the same way under the standard model (SM) electroweak symmetry group $SU(3)_c \times SU(2)_L \times U(1)_Y$. As a consequence, vector-like quarks can obtain mass through direct mass terms in the Lagrangian of the form $m\bar{\psi}\psi$, unlike the SM chiral quark masses that are generated through the Yukawa coupling.
- This paper presents the results of a search for neutral spin-1 heavy resonances decaying in a top and a vector-like T quarks with charge $2/3 e$. Many of the models mentioned above predict predominant decays of the T quark to third generation SM quarks and the three decay modes: tH, tZ, and bW [1].
- Searches for neutral spin-1 heavy resonances with enhanced coupling to the third generation of the SM have been performed by the CMS and ATLAS collaborations (e.g. $Z' \rightarrow t\bar{t}$) setting lower limits from 2.4 to 2.9 TeV depending on the model used.
- Direct searches for T quarks have been performed by the CMS and ATLAS collaborations, setting lower limits on the T quark mass ranging from 715 to 950 GeV, for different T quark branching fractions [2–5].
- The analysis is based on the proton-proton collisions collected during 2015 by the CMS experiment at the LHC at a center-of-mass energy of $\sqrt{s}=13$ TeV. The search targets decays of a Z' boson into a T' quark and an hadronically decaying top quark. The T' quark is further required to decay into an hadronically decaying W boson and a b quark.
- In the kinematic scenarios considered the T' quark does not have a large transverse momentum in relation to its mass, thus its decay products are angularly well separated. However due to the large difference in mass between the W boson and the T' quark, the former receives a large high Lorentz boost and its decay products are not well separated, leading to merged jets. We will employ jet substructure algorithms to reconstruct and identify the W boson coming from the decay of the T' quark. If the mass difference between the Z' boson and the T' quark is large enough the top quark coming from the decay of the Z' also receives a large transverse momentum, and in that case jet substructure techniques and top tagging can be used to identify and reconstruct the hadronic decay of the top quark.
- The most dominant SM background is the QCD multijet process, followed SM top-antitop pair production. While Standard Model pair production processes can be suppressed by using mass

61 requirementd on the reconstructed T' mass, a data-driven background estimate is required for
62 the estimation of the QCD multijet production.

63 **Analysis strategy**

64 Full event reconstruction is pursued. In this analysis, we focus on the all hadronic final state.
65 We reconstruct the top quark and W boson decays using a jet substructure based top tagger
66 and W tagger. B tagging is used to find the b jet coming from the decay of the T'. We use subjet
67 b tagging for further refining the selection of events containing a top quark. By summing the
68 4-vectors of the b tagged jet and the W-tagged jet we obtain the T' candidate. By summing the
69 4-vectors of the T' cantitate and the top tagged jet we obtain the Z' candidate. We cut on the T'
70 mass candidate and use the Z' mass candidate as main observable in the analysis.

71 Events are selected with a cut-based approach, using kinematic event-variables. For the final
72 observable, we estimate the background shape from a sideband region in the recorded data.
73 MC-based correction are applied to the sideband region to reproduce the shape of the back-
74 ground in the signal region. Using the background estimate, expected and observed exclusion
75 significances are calculated for Z' masses in the range of 1500 to 2500 GeV and T quark masses
76 in the range of 700 to 1500 GeV.

DRAFT

77 2 Samples

78 Tab. 2 shows a table of the background MC samples used in this analysis, along with short
 79 names and cross-sections used for normalization. For the normalization of signal samples, as
 80 listed in Tab. 1, a cross section of 1 pb is used, unless stated differently. The $Z' \rightarrow VLQ$ assume a
 81 left-handed, very narrow width T' and a Z' with 1% width unless otherwise stated in the table.
 82 All MC samples are from the MiniAODv2 76X campaign. CMSSW_7_6_3 is used, with the global
 83 tags 76X_dataRun2_v15 and 76X_mcRun2_asymptotic_v12 for data and MC, respectively.

84 Recorded data from the Jet-HT primary dataset are used, see Table 3. The silver JSON lumi
 85 mask is applied¹. We use the HLT_PFHT800 trigger and obtain a luminosity of $\mathcal{L} = 2.690 \text{ fb}^{-1}$.

86 Several simulated signal samples were analyzed. Using MADGRAPH v5.2 [6], we generate
 87 neutral spin-1 resonances (Z') decaying exclusively to a top quark and a up-type heavy vector-
 88 like quark (T'). We choose a 1% width for the Z' resonance and a 1 MeV width for the T'
 89 resonance. The T' quark is generated with left-handed chirality. The choice of width for the
 90 Z' is arbitrary and follows what was previously done for $Z' \gamma t\bar{t}$ searches. The T' width was
 91 chosen to be consistent with direct single and pair VLQ searches

92 We generate signal samples for all the possible final states of the T' : a b quark and a W boson, a
 93 top quark and a Higgs boson, and a top quark and a Z boson. The analysis is optimized for the
 94 decay mode into a b quark and a W boson, however all possible T' decay modes are considered
 95 in the analysis. Several mass hypotheses for the mass of the Z' and the T' are considered
 96 ranging from 1.5 to 2.5 TeV for the Z' and from 0.7 to 1.5 TeV for the T' . The combination of
 97 the masses is chosen so that the mass of the T' is roughly half, two thirds, or five sixths of the
 98 mass of the Z' . See Figure 1 for a schematic view of the Z' and T' masses for the generated
 99 signal samples. This kinematic range is the most interesting for a mixed SM quark and heavy
 100 vector-like quark decay mode, as opposed to full VLQ decay modes. If the mass of the Z' is
 101 (roughly) more than twice the mass of the T' , then the decay mode of the Z' in T' pairs would
 102 be kinematically preferred and dominant with respect to $T't$. So the range where the $Z' \rightarrow T't$
 103 is relevant and interesting lies roughly between $m(Z')/2 < m(T') < m(Z') - m(t)$. The LHR
 104 is due to the fact that $Z' \rightarrow T'T'$ becomes dominant, while the RHT is due to the decay being
 105 kinematically allowed.

106 The signal production is based on a simplified low-energy effective model describing the phe-
 107 nomenology of heavy vector resonances in the minimal composite Higgs model [7].

108 The decay of heavy resonances for signal samples is treated with MADSPIN [8] to correctly
 109 propagate the helicity through the decay products. Higher-order parton radiations up to one
 110 extra partons are included at tree-level. We use PYTHIA 8.2 [9] to model the parton showering
 111 and the MLM algorithm [10] is used for the matching. Differential jet rates are checked for
 112 smoothness to ensure that the matching scale is chosen correctly.

113 A selection of basic distributions of the signal samples at generator level is depicted in Fig. 2,
 114 3. The generator particles in consideration are found starting at the Z' boson. All the decay chain
 115 is reconstructed by using daughter-links.

116 Features of general importance for the event selection are the transverse momentum of the top
 117 quark and the W boson and the angular separation of the decay products.

¹Cert_13TeV_16Dec2015ReReco_Collisions15_25ns_JSON_Silver_v2

Table 1: Signal MonteCarlo samples used in the analysis.

Sample	Dataset	Int. Lumi. (pb^{-1})
TBar	/TT_TuneCUETP8M1_13TeV-powheg-Pythia8_RunIIFall15MiniAODv2-PU25nsData2015v1	117767.67
QCD 500 < HT < 700	/QCD_HT500to700_TuneCUETP8M1_13TeV-madgraphMLM-Pythia8_RunIIFall15MiniAODv2-PU25nsData2015v1	612.6385
QCD 700 < HT < 1000	/QCD_HT700to1000_TuneCUETP8M1_13TeV-madgraphMLM-Pythia8_RunIIFall15MiniAODv2-PU25nsData2015v1	2276.089
QCD 1000 < HT < 1500	/QCD_HT1000to1500_TuneCUETP8M1_13TeV-madgraphMLM-Pythia8_RunIIFall15MiniAODv2-PU25nsData2015v1	4183.32
QCD 1500 < HT < 2000	/QCD_HT1500to2000_TuneCUETP8M1_13TeV-madgraphMLM-Pythia8_RunIIFall15MiniAODv2-PU25nsData2015v1	32833.02
QCD 2000 < HT < Inf	/QCD_HT2000toInf_TuneCUETP8M1_13TeV-madgraphMLM-Pythia8_RunIIFall15MiniAODv2-PU25nsData2015v1	78495.56
Single top t-channel	/ST_t-channel_4f_leptonDecays_13TeV-amcatnlo-Pythia8_TuneCUETP8M1_RunIIFall15MiniAODv2-PU25nsData2015v1	18992240
Single top tW channel	/ST_tW_top_5f_inclusiveDecays_13TeV-powheg-Pythia8_TuneCUETP8M1_RunIIFall15MiniAODv2-PU25nsData2015v1	28089.89
Single antitop tW channel	/ST_tW_antitop_5f_inclusiveDecays_13TeV-powheg-Pythia8_TuneCUETP8M1_RunIIFall15MiniAODv2-PU25nsData2015v1	28073.03
Single top s-channel	/ST_s-channel_4f_leptonDecays_13TeV-amcatnlo-Pythia8_TuneCUETP8M1_RunIIFall15MiniAODv2-PU25nsData2015v1	1001494

Table 2: Background MonteCarlo samples used in the analysis.

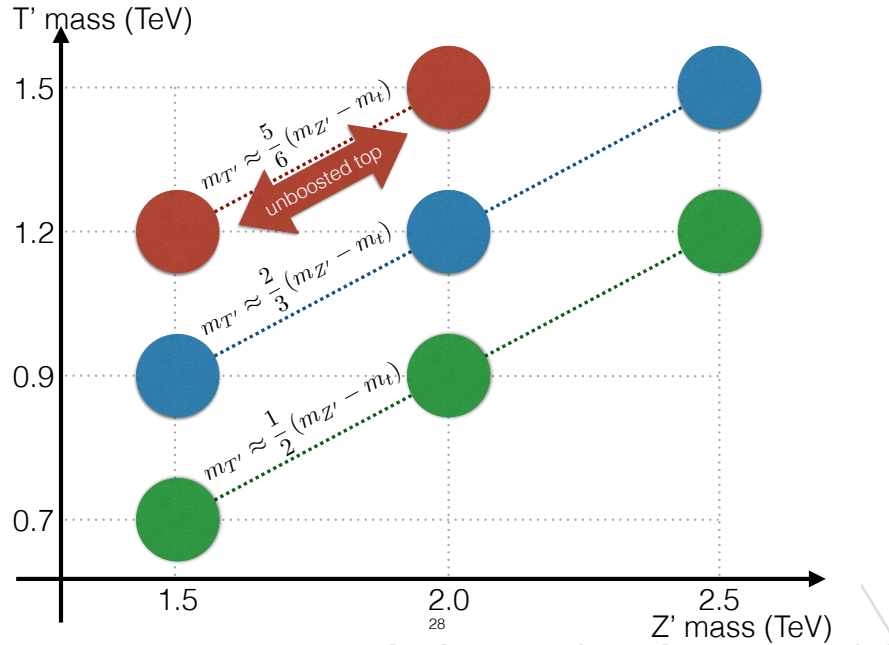


Figure 1: Scheme of the Z' and T' masses for the generated signal samples.

Sample	Dataset	Int. Lumi. (pb^{-1})
JetHT	/JetHT/Run2015C_25ns-16Dec2015-v1/MINIAOD	17.23
JetHT	/JetHT/Run2015D-16Dec2015-v1/MINIAOD	2611.62

Table 3: Data samples used in the analysis.

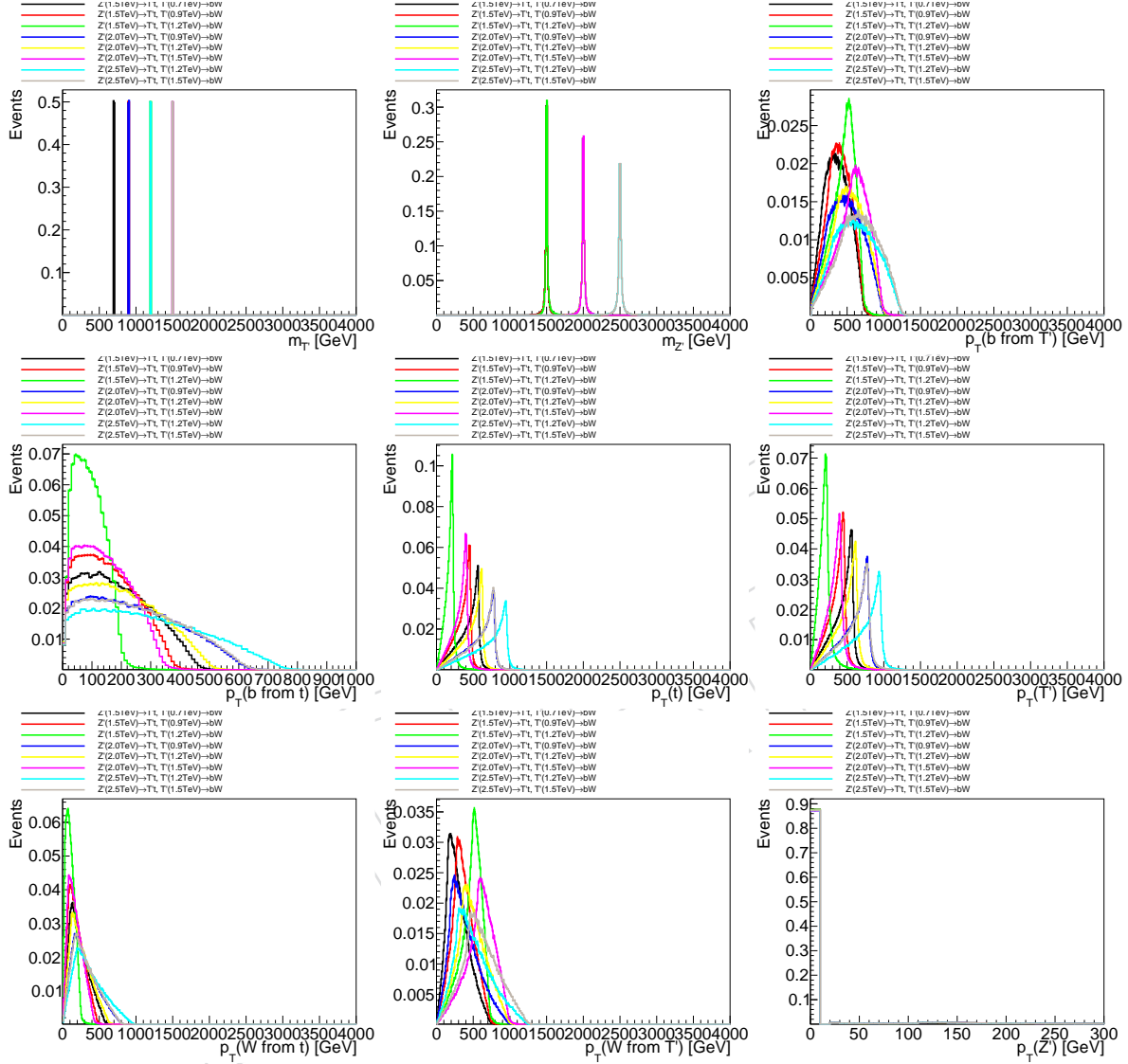


Figure 2: Some GEN-level kinematic distribution for signal samples.

First row, from left to right: mass of the T' , mass of the Z' , p_T of the b quark from the T' .

Second row, from left to right: p_T of the b quark from the t , p_T of the t quark, p_T of the T' .

Third row, from left to right: p_T of the W quark from the t , p_T of the W quark from the T' , p_T of the Z' .

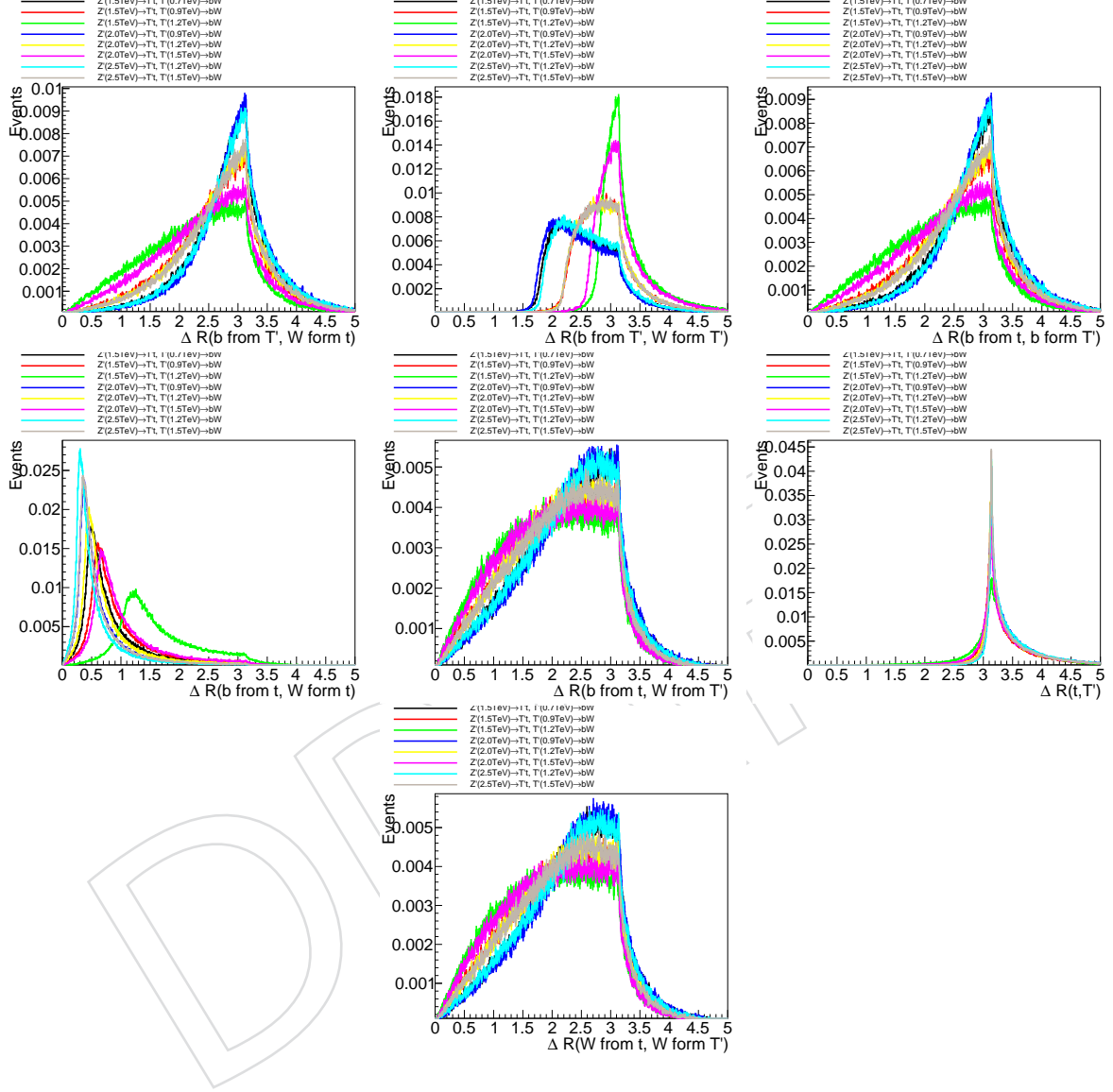


Figure 3: Some GEN-level kinematic distribution for signal samples.

First row, from left to right: ΔR between the b from the T' and the W from the t , ΔR between the W from the T' and the b from the T' , ΔR between the b from the t and the b from the T' .
 Second row, from left to right: ΔR between the W from the t and the b from the t , ΔR between the W from the T' and the b from the t .
 Third row, from left to right: ΔR between the W from the T' and the W from the t .

118 3 Selection

119 3.1 Primary Vertex

120 We reconstruct the primary vertex in each event by clustering tracks using a deterministic an-
 121 nealing algorithm. Only vertices passing the following requirements are considered:

- 122 • $\sqrt{x^2 + y^2} < 2 \text{ cm}$ and $|z| < 24 \text{ cm}$,
- 123 • $N_{DOF} > 4$, where N_{DOF} is the weighted number of tracks used to reconstruct that
 124 vertex.

125 The vertex with the highest $\sum_{\text{tracks}} p_T^2$ is selected as the primary vertex.

126 3.2 Pileup

127 We reweight each MC event as a function of the Number of Primary Vertices so that the num-
 128 ber of true pileup interactions in simulation matches the instantaneous luminosity profile mea-
 129 sured in data. We assume a minimum bias cross-section of 69mb. The distribution of the
 130 number of primary vertices in data and MC after the reweight is applied can be seen in Figure
 131 4.

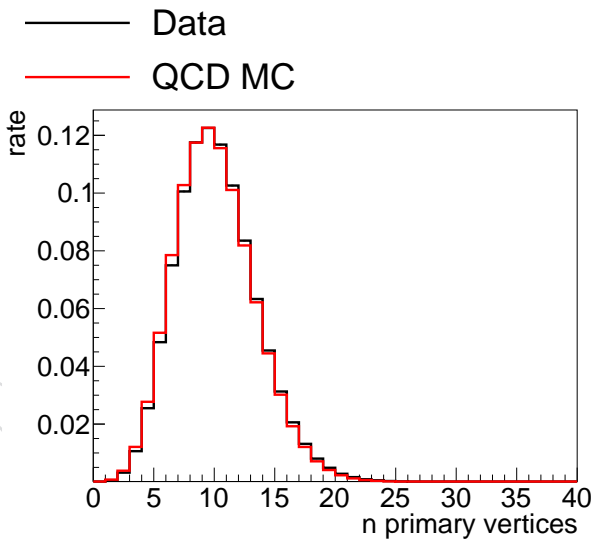


Figure 4: Distribution of the number of primary vertices in data and MC after the pileup reweight is applied

132 3.3 Object IDs

133 The analysis consider only jets in final decay state. We use two different jet collections: one is
 134 the AK4 slimmedJets jet collection taken directly from the MINIAOD event content, the other
 135 is the AK8 Soft Drop jet collection, also obtained directly from MINIAOD.

136 All AK4-jets are required to have a p_T of larger than 30 GeV, must pass the loose PFJet ID and
 137 have $|\eta| < 2.4$. Level 1, 2 and 3 jet corrections (Fall15_25nsV2) are applied² in MC and data,
 138 additionally Level 2 and 3 residual corrections are applied in the data. In order to evaluate
 139 the systematic uncertainty of the jet energy corrections, the analysis is performed individually

²<https://twiki.cern.ch/twiki/bin/view/CMS/JECDATA>

140 with the up and down variation of uncertainty on the corrections applied. Jet energy resolution
 141 smearing is applied³, based on matching between generator and reconstructed jets. As for the
 142 jet corrections, the analysis is rerun for the given up and down variation of uncertainty on the
 143 corrections.

144 AK8 jets are used as source for Top and W candidates, and only used in this analysis if they
 145 have $p_T > 200 \text{ GeV}$ and $|\eta| < 2.4$. Soft drop grooming is applied on the charged-hadron
 146 subtracted (CHS) jets. No Jet ID is applied to AK8 jets.

147 The level 1, 2 and 3 AK8 jet corrections from the same campaign as for the AK4 jets are applied
 148 to the fatjet. For the subjets, the level 2 and 3 AK4 jet-corrections are used. The jet p_T is taken
 149 from the AK8 fatjet, while the soft drop mass is calculated using soft drop subjets.

150 The uncertainty on the AK8 jet corrections (for top and W candidates) and AK4 jets corrections
 151 (for AK4 b-jets and AK8 subjets) leans on the prescription for W tagging⁴. The systematic
 152 uncertainties on the jet corrections of AK8 jet(s), subjet(s), and AK4 b-jet are treated as fully
 153 correlated.

154 Jet energy resolution smearing is applied on AK8 fatjets, based on matching between generator
 155 and reconstructed jets. For the subjets, the AK4 smearing factors are applied

156 B-tagging is applied on AK4 jets and on the softdrop subjets of AK8 jets, where the medium
 157 working point of the CSVv2-algorithm is used [11, 12]. The relevant scale factors ('RunI-
 158 IFall15DR76'⁵) are applied using method 1a⁶. Official 76X subjet b tagging scale factors are
 159 applied. Systematic uncertainties attached to the b-tag scale factors are propagated to the end
 160 result, where the uncertainties for AK4 b tagging and subjet b tagging are considered corre-
 161 lated. Heavy flavour jets (b/c-hadrons) and light flavour jets (u/d/s/g-jets) are treated as
 162 correlated.

163 This analysis uses W tagging to reconstruct the boosted hadronic decay of the W, coming from
 164 the decay of the T' vector-like quark. The W tagger we use is based on AK8 soft drop jets and
 165 is defined as follows:

- 166 • fat jet $p_T > 200 \text{ GeV}$
- 167 • soft drop mass: $70 < m_{SD} < 100 \text{ GeV}$
- 168 • n-subjettiness ratio: $\tau_2/\tau_1 < 0.6$

169 We use a flat rate Data/MC correction scale factor of 0.98 ± 0.03 as derived in JME-16-003.
 170 Uncertainties are propagated as flat rate systematic errors by varying the scale factor value of
 171 1σ . For jets with $p_T > 300 \text{ GeV}$ the uncertainty is increased to 0.048. The scale factor is applied
 172 only when the W-tagged jet is matched to a generator level W. When the AK4 JEC are varied,
 173 the softdrop mass is recalculated. Jet mass calibration correction variation isn't included, but
 174 the latest measurements show it is very small and can be ignored.

175 This analysis uses top tagging to reconstruct the boosted hadronic decay of the top, coming
 176 from the decay of the Z' boson. The top tagger we use is based on AK8 soft drop jets and is
 177 defined as follows:

- 178 • fat jet $p_T > 400 \text{ GeV}$
- 179 • soft drop mass: $110 < m_{SD} < 210 \text{ GeV}$

³<https://twiki.cern.ch/twiki/bin/view/CMS/JetResolution>

⁴<https://twiki.cern.ch/twiki/bin/view/CMS/JetWtagging>

⁵<https://twiki.cern.ch/twiki/bin/viewauth/CMS/BtagRecommendation>

⁶<https://twiki.cern.ch/twiki/bin/viewauth/CMS/BTagSFMethods>

- 180 • n-subjettiness ratio: $\tau_3/\tau_2 < 0.86$
 181 • as a separate category in the analysis we require at least one of the subjets to be b
 182 tagged using the CSVv2 medium operating point

183 This top tagging definition corresponds to the loose “ $\epsilon(B) = 10\%$ SD WP1” official working
 184 point for 74X⁷. Official 76X scale factors for this operating point are applied: a p_T -dependent
 185 scale factor is applied to the t-tagged jet (0.85 for $p_T < 550$ GeV, 1.08 for $p_T > 550$ GeV).

186 3.4 Trigger

187 We are performing an all hadronic analysis in the boosted regime. Many highly-energetic jets
 188 will be present in the final state. Given that the Z' masses we are probing for start at 1.5 TeV,
 189 we consider the HLT_PFHT800 trigger for our analysis. The trigger requires the trigger-level
 190 particle-flow HT to be greater than 800 GeV. The HT variable is reconstructed summing the p_T
 191 of AK4 jets clustered from trigger-level particle-flow components. We expect this condition to
 192 be satisfied by the vast majority of the events we want to select and analyze. Thus we do not
 193 consider any jet substructure all-hadronic trigger to complement the base HT trigger.

194 We perform trigger studies to assess, firstly, where to set the offline HT cut to reject the trigger
 195 efficiency turn-on, and secondly DATA-MC trigger efficiency corrections, if needed at all. To
 196 be able to properly measure the trigger efficiency in DATA we need a base independent trigger
 197 to pre-select our events. We use this base triggers: HLT_PFHT650, this is a prescaled, lower
 198 threshold version of the trigger used in the analysis. A cross-check is performed using this
 199 other base trigger: HLT_Mu45_eta2p1. This leptonic trigger is completely independent from
 200 the hadronic trigger we are using, however due to its nature, by preselecting events with this
 201 trigger we contaminate the background composition with processes that aren’t present in our
 202 analysis.

203 To obtain proper trigger efficiency curves we have to relax the analysis cuts, we measure trigger
 204 efficiency against the following analysis-like selections:

- 205 1. one top-tagged jet ($p_T > 150$ GeV) and one W-tagged jet ($p_T > 150$ GeV)
- 206 2. one top-tagged jet ($p_T > 400$ GeV) and one W-tagged jet ($p_T > 200$ GeV)
- 207 3. one top-tagged jet ($p_T > 150$ GeV), one W-tagged jet ($p_T > 150$ GeV), one medium b-
 208 tagged jet ($p_T > 100$ GeV, $\Delta R(b\text{-jet},\text{top-jet}), \Delta R(b\text{-jet},W\text{-jet}) > 0.8$)
- 209 4. one top-tagged jet ($p_T > 400$ GeV), one W-tagged jet ($p_T > 200$ GeV), one medium b-
 210 tagged jet ($p_T > 100$ GeV, $\Delta R(b\text{-jet},\text{top-jet}), \Delta R(b\text{-jet},W\text{-jet}) > 0.8$)
- 211 5. one top-tagged jet ($p_T > 150$ GeV) with one medium b-tagged subjet, one W-tagged jet
 212 ($p_T > 150$ GeV), one medium b-tagged jet ($p_T > 100$ GeV, $\Delta R(b\text{-jet},\text{top-jet}), \Delta R(b\text{-jet},W\text{-jet}) > 0.8$)
- 214 6. one top-tagged jet ($p_T > 400$ GeV) with one medium b-tagged subjet, one W-tagged jet
 215 ($p_T > 200$ GeV), one medium b-tagged jet ($p_T > 100$ GeV, $\Delta R(b\text{-jet},\text{top-jet}), \Delta R(b\text{-jet},W\text{-jet}) > 0.8$)

217 The trigger efficiency is defined as the ratio of:

- 218 • Denominator: all events passing the base trigger and the pseudo-analysis selection.

⁷<https://twiki.cern.ch/twiki/bin/view/CMS/JetTopTagging>

- 219 • Numerator: all events passing the denominator selection and firing the HLT_PFT800
 220 trigger.

221 For this study we use the data, $t\bar{t}$ and MC samples defined in section 2 and Table 2. In addition,
 222 the SingleMu data samples are used for the crosscheck with the HLT_Mu45_eta2p1 trigger. We
 223 compare the trigger efficiency of data with the $t\bar{t}$ MC sample, the QCD MC sample and their
 224 sum using the proper cross section weights.

225 The trigger efficiency is shown in function of the HT variable, defined as the sum of the p_T of
 226 all the AK4 jets with $p_T > 50$ GeV and $|\eta| < 2.3$, in Figs. 6 and 8. Additionally we show the
 227 efficiencies in function of the HT_{CA8} variable, defined as the sum of the p_T of the two p_T -leading
 228 AK8 jets, in Figs. 5 and 7.

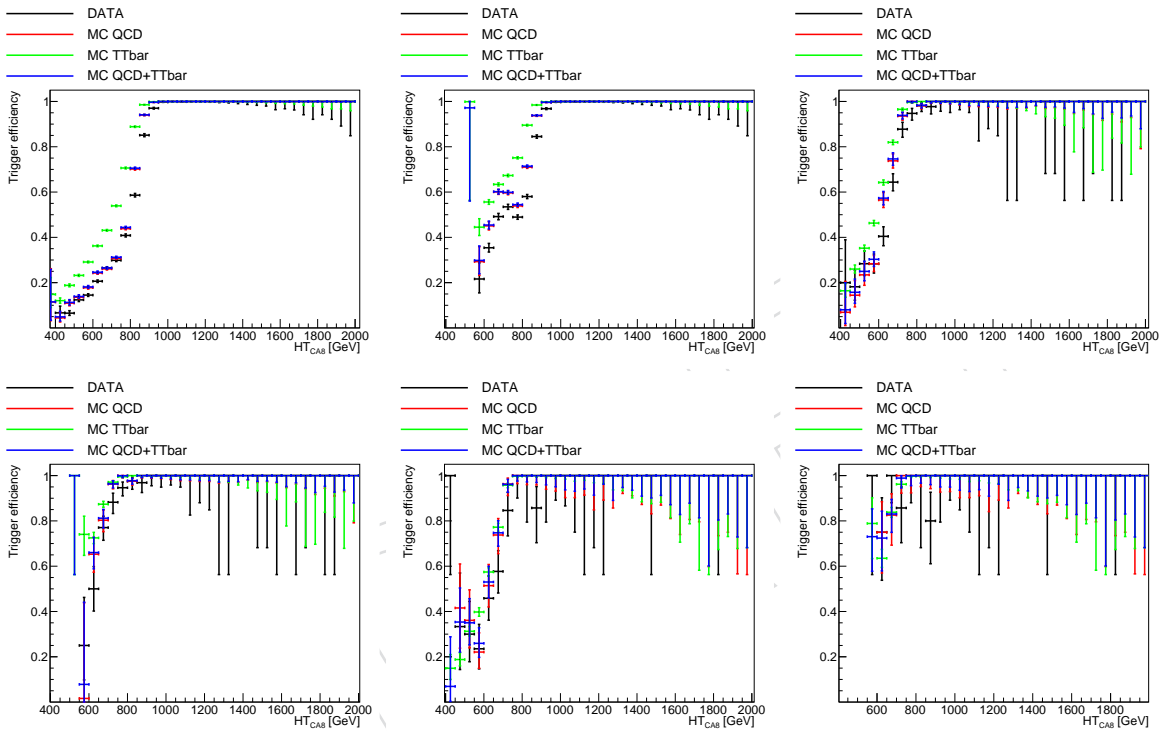


Figure 5: HLT_PFT800 trigger efficiencies for in function of HT_{CA8} on top of HLT_PFT650 for DATA (black), QCD MC (red), TTbar MC (green), MC QCD+TTbar (blue).

First row, from left to right: on top of selection (1), (2), (3).

Second row, from left to right: on top of selection (4), (5), (6).

229 From these trigger studies we conclude that an HT cut above 850 GeV is a good choice to reject
 230 the trigger efficiency turn on, no trigger scale factors are demmed necessary by this analysis,
 231 and we decide to assign a flat 3% uncertainty on trigger efficiency.

232 3.5 Final selection

233 We select events in the signal region with the following requirements:

- 234 • one top tagged AK8 jet
- 235 • one W tagged AK8 jet
- 236 • one medium CSVv2 b tagged AK4 jet with $p_T > 100$ GeV, $\Delta R(\text{top jet}, \text{jet}) > 0.8$,
- 237 $\Delta R(\text{W jet}, \text{jet}) > 0.8$

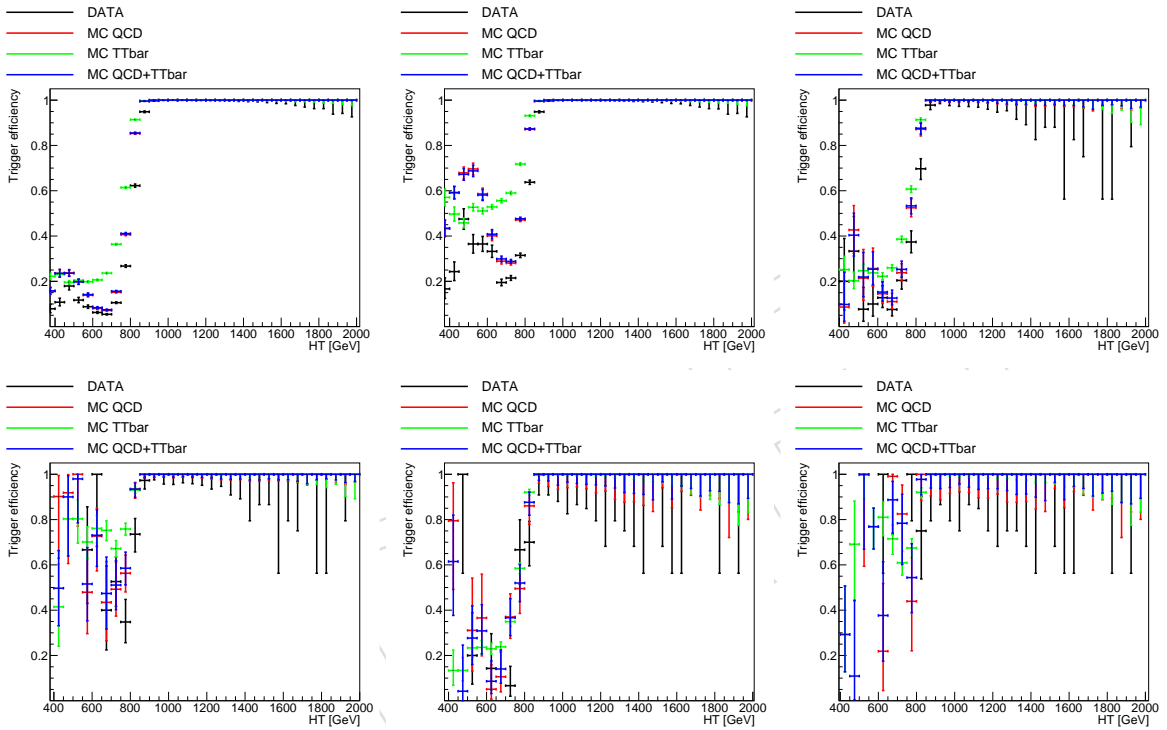


Figure 6: HLT_PFTHT800 trigger efficiencies for in function of HT on top of HLT_PFTHT650 for DATA (black), QCD MC (red), TTbar MC (green), MC QCD+TTbar (blue).
 First row, from left to right: on top of selection (1), (2), (3).
 Second row, from left to right: on top of selection (4), (5), (6).

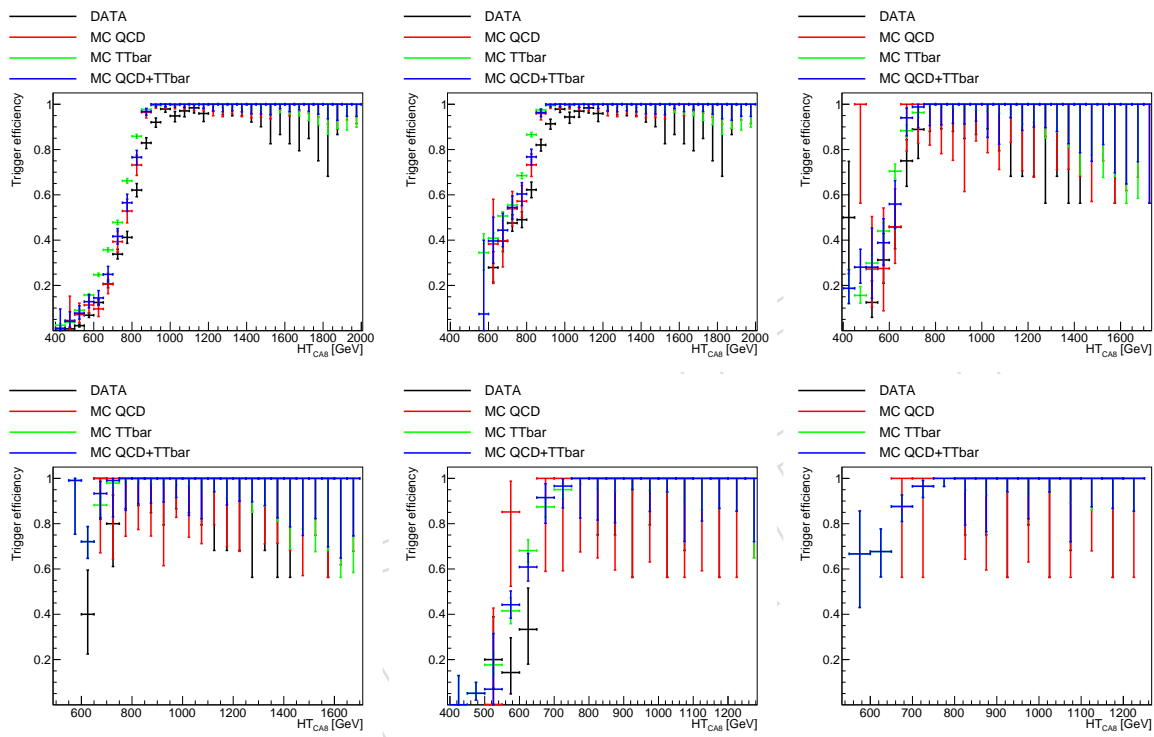


Figure 7: HLT_PFTHT800 trigger efficiencies for in function of HT_{CAA8} on top of HLT_Mu45_eta2p1 for DATA (black), QCD MC (red), TTbar MC (green), MC QCD+TTbar (blue).

First row, from left to right: on top of selection (1), (2), (3).

Second row, from left to right: on top of selection (4), (5), (6).

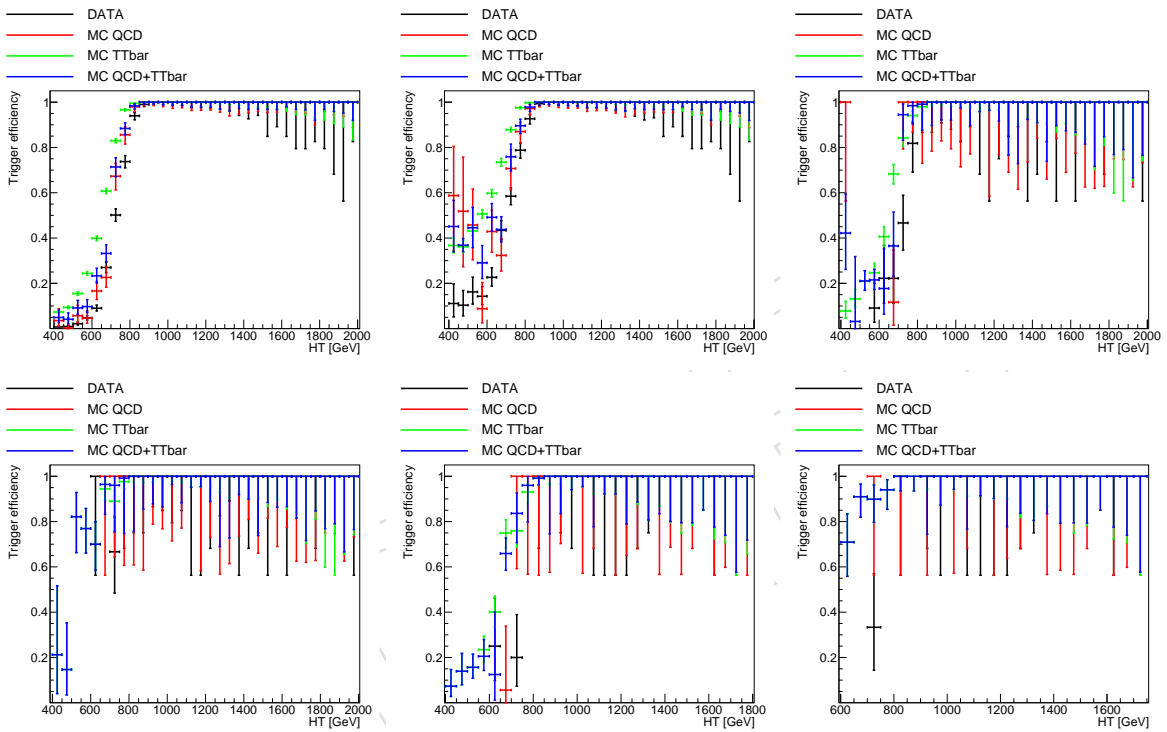


Figure 8: HLT_PFT800 trigger efficiencies for in function of HT on top of HLT_Mu45_eta2p1 for DATA (black), QCD MC (red), TTbar MC (green), MC QCD+TTbar (blue).
 First row, from left to right: on top of selection (1), (2), (3).
 Second row, from left to right: on top of selection (4), (5), (6).

Sample	Eff. 1 b-tag cat.	Eff. 2 b-tag cat.
$Z'(1500 \text{ GeV}) \rightarrow T't, T'(900 \text{ GeV}) \rightarrow Ht$	$(0.55 \pm 0.15)\%$	$(0.75 \pm 0.17)\%$
$Z'(1500 \text{ GeV}) \rightarrow T't, T'(700 \text{ GeV}) \rightarrow Ht$	$(0.65 \pm 0.16)\%$	$(0.93 \pm 0.19)\%$
$Z'(1500 \text{ GeV}) \rightarrow T't, T'(1200 \text{ GeV}) \rightarrow Ht$	$(0.26 \pm 0.10)\%$	$(0.37 \pm 0.12)\%$
$Z'(2000 \text{ GeV}) \rightarrow T't, T'(900 \text{ GeV}) \rightarrow Ht$	$(1.8 \pm 0.3)\%$	$(2.6 \pm 0.3)\%$
$Z'(2000 \text{ GeV}) \rightarrow T't, T'(1200 \text{ GeV}) \rightarrow Ht$	$(2.0 \pm 0.3)\%$	$(2.9 \pm 0.3)\%$
$Z'(2000 \text{ GeV}) \rightarrow T't, T'(1500 \text{ GeV}) \rightarrow Ht$	$(1.7 \pm 0.3)\%$	$(2.2 \pm 0.3)\%$
$Z'(2500 \text{ GeV}) \rightarrow T't, T'(1200 \text{ GeV}) \rightarrow Ht$	$(2.9 \pm 0.3)\%$	$(3.9 \pm 0.4)\%$
$Z'(2500 \text{ GeV}) \rightarrow T't, T'(1500 \text{ GeV}) \rightarrow Ht$	$(3.0 \pm 0.3)\%$	$(4.1 \pm 0.4)\%$
$Z'(1500 \text{ GeV}) \rightarrow T't, T'(700 \text{ GeV}) \rightarrow Zt$	$(0.62 \pm 0.15)\%$	$(0.84 \pm 0.18)\%$
$Z'(1500 \text{ GeV}) \rightarrow T't, T'(900 \text{ GeV}) \rightarrow Zt$	$(0.78 \pm 0.17)\%$	$(0.98 \pm 0.19)\%$
$Z'(1500 \text{ GeV}) \rightarrow T't, T'(1200 \text{ GeV}) \rightarrow Zt$	$(0.50 \pm 0.14)\%$	$(0.54 \pm 0.14)\%$
$Z'(2000 \text{ GeV}) \rightarrow T't, T'(900 \text{ GeV}) \rightarrow Zt$	$(2.4 \pm 0.3)\%$	$(3.1 \pm 0.4)\%$
$Z'(2000 \text{ GeV}) \rightarrow T't, T'(1200 \text{ GeV}) \rightarrow Zt$	$(2.8 \pm 0.3)\%$	$(3.9 \pm 0.4)\%$
$Z'(2000 \text{ GeV}) \rightarrow T't, T'(1500 \text{ GeV}) \rightarrow Zt$	$(2.3 \pm 0.3)\%$	$(2.8 \pm 0.3)\%$
$Z'(2500 \text{ GeV}) \rightarrow T't, T'(1200 \text{ GeV}) \rightarrow Zt$	$(4.3 \pm 0.4)\%$	$(5.4 \pm 0.5)\%$
$Z'(2500 \text{ GeV}) \rightarrow T't, T'(1500 \text{ GeV}) \rightarrow Zt$	$(4.5 \pm 0.4)\%$	$(6.0 \pm 0.5)\%$
$Z'(1500 \text{ GeV}) \rightarrow T't, T'(700 \text{ GeV}) \rightarrow Wb$	$(1.2 \pm 0.2)\%$	$(1.9 \pm 0.3)\%$
$Z'(1500 \text{ GeV}) \rightarrow T't, T'(900 \text{ GeV}) \rightarrow Wb$	$(0.74 \pm 0.17)\%$	$(1.1 \pm 0.2)\%$
$Z'(1500 \text{ GeV}) \rightarrow T't, T'(1200 \text{ GeV}) \rightarrow Wb$	$(0.23 \pm 0.09)\%$	$(0.21 \pm 0.09)\%$
$Z'(2000 \text{ GeV}) \rightarrow T't, T'(900 \text{ GeV}) \rightarrow Wb$	$(2.6 \pm 0.3)\%$	$(3.6 \pm 0.4)\%$
$Z'(2000 \text{ GeV}) \rightarrow T't, T'(1200 \text{ GeV}) \rightarrow Wb$	$(2.1 \pm 0.3)\%$	$(3.0 \pm 0.4)\%$
$Z'(2000 \text{ GeV}) \rightarrow T't, T'(1500 \text{ GeV}) \rightarrow Wb$	$(0.89 \pm 0.18)\%$	$(0.87 \pm 0.18)\%$
$Z'(2500 \text{ GeV}) \rightarrow T't, T'(1200 \text{ GeV}) \rightarrow Wb$	$(3.3 \pm 0.4)\%$	$(3.9 \pm 0.4)\%$
$Z'(2500 \text{ GeV}) \rightarrow T't, T'(1500 \text{ GeV}) \rightarrow Wb$	$(2.8 \pm 0.3)\%$	$(3.6 \pm 0.4)\%$

Table 4: Selection efficiency for the signal in the different categories used in the analysis. Statistical uncertainties are quoted.

- the T' candidate reconstructed as the sum of the 4-vectors of the W tagged jet and the b tagged jet is required to have a mass larger than 500 GeV.
- we introduce two categories: one where the top tagged jet does not have any b tagged subjets (called from now on: 1 b tag or no subjet b tag) and one where at least one of the subjets is b tagged with the CSVv2 medium operating point (called from now on: 2 b tag or subjet b tag).

The number of selected events and the total efficiency is reported in Tab 4

A variety of distributions of kinematic and other relevant variables, at various stages of the selection procedure can be seen in Figs. 9-15. The distribution of the Z' candidate mass in the two signal regions can be seen in Fig 16.

Many of these plots show a poor agreement between Data and prediction. This is due to the fact that the main component of the background is the QCD multijet production that is estimated with a MonteCarlo simulation in these plots. The QCD multijet MonteCarlo is notoriously not reliable in modeling both the normalization and the shape of distributions in these areas of the phase space. A dedicated data-driven procedure to estimate the QCD multijet production in the signal region, for the distribution of the Z' candidate mass will be developed in Section 4.

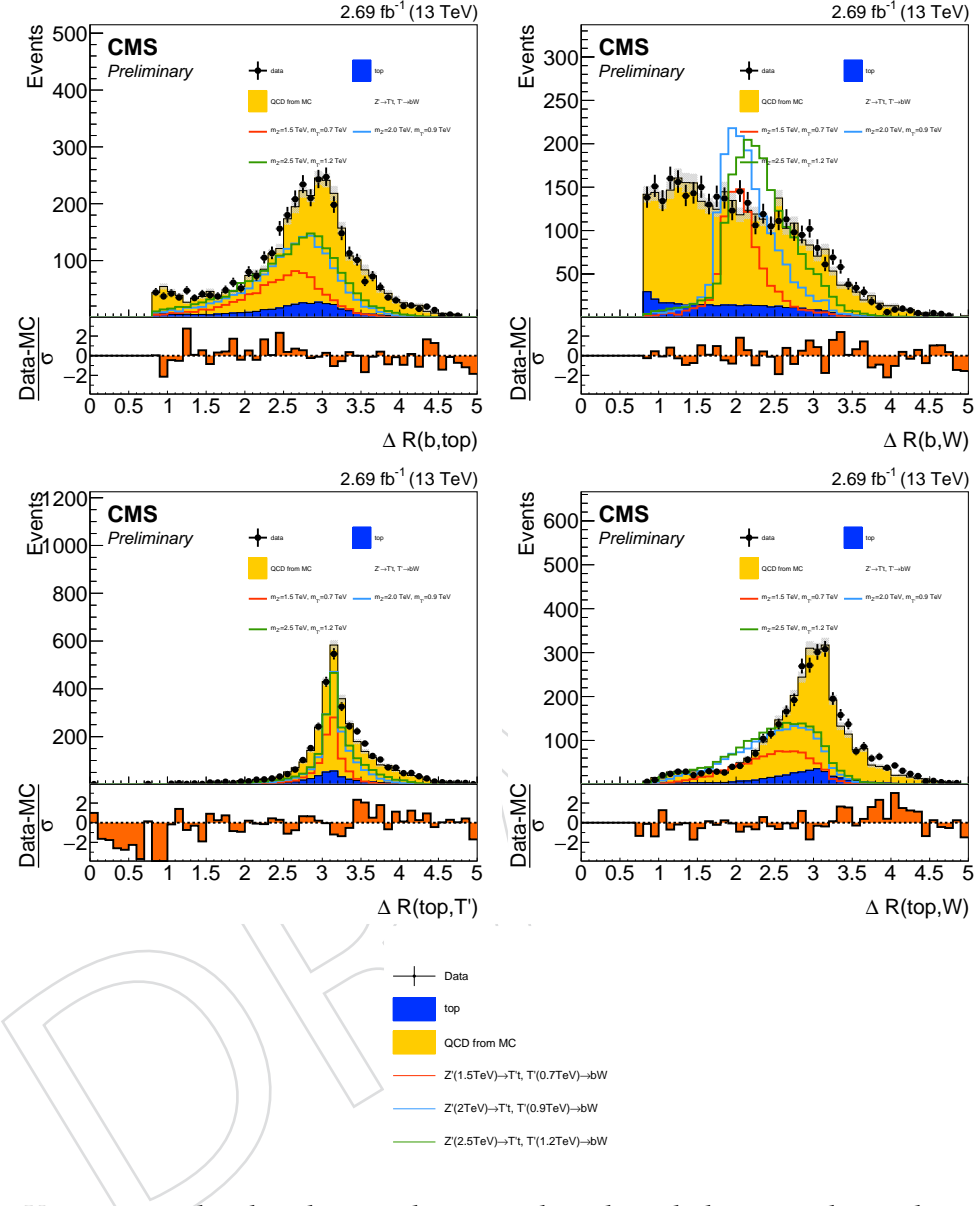


Figure 9: Various angular distributions between the selected objects in the analysis for signal, data, QCD, and $t\bar{t}$ bar. The distributions are plotted before cutting on the T' mass. Signal is normalized to a cross section of 10pb . First row, from left to right: $\Delta R(\text{b jet},\text{top jet})$, $\Delta R(\text{b jet},W \text{ jet})$. Second row, from left to right: $\Delta R(t \text{ jet},T' \text{ candidate})$, $\Delta R(t \text{ jet},W \text{ jet})$.

The poor agreement between Data and prediction is due to the fact that the QCD multijet production is estimated with a MonteCarlo simulation in these plots. The QCD multijet MonteCarlo is not reliable in modeling both the normalization and the shape of distributions in these areas of the phase space. A dedicated data-driven procedure to estimate the QCD multijet production in the signal region, for the distribution of the Z' candidate mass will be developed in Section 4.

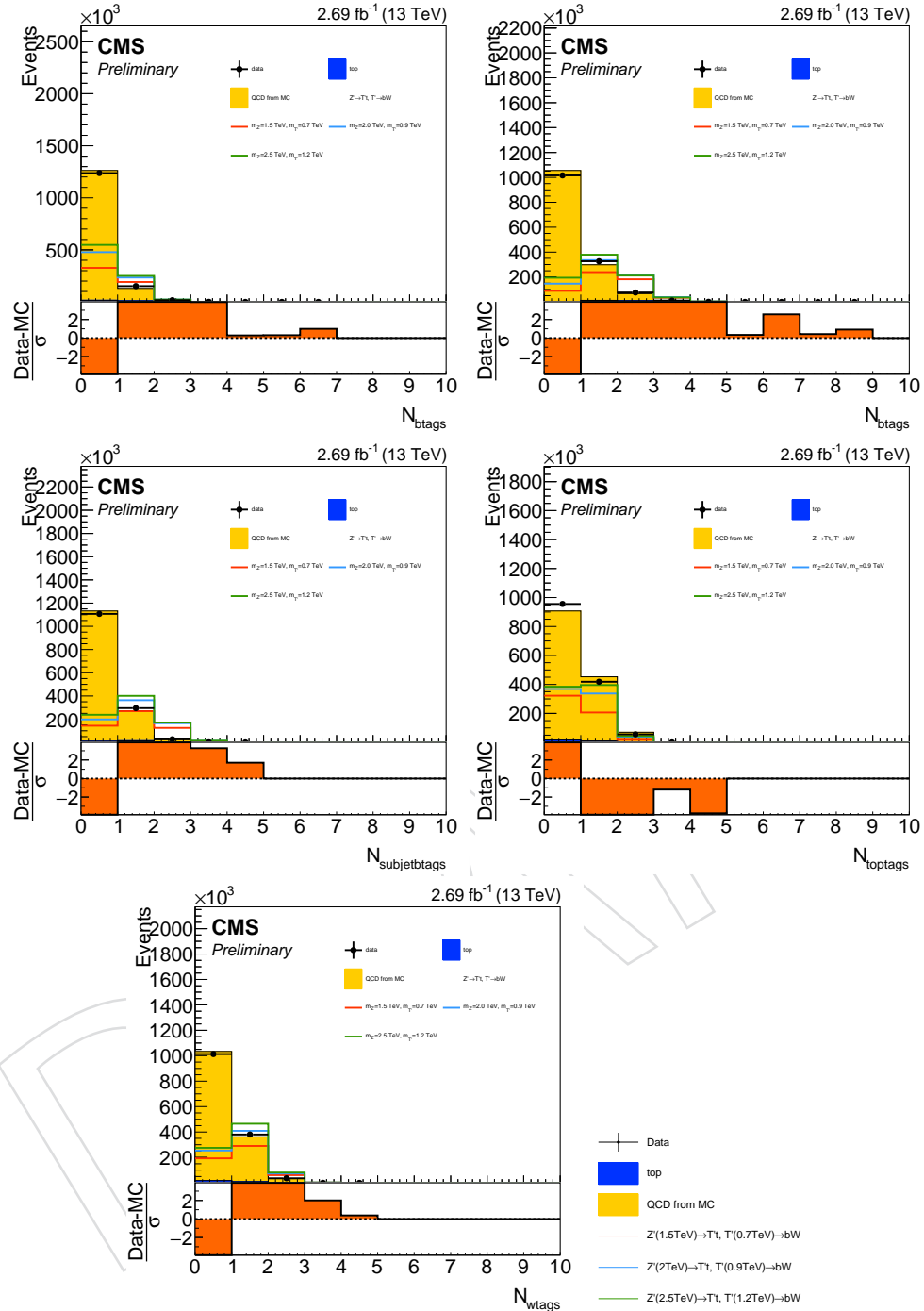


Figure 10: Various per-event counting distributions of the objects in the analysis for signal, data, QCD, and $t\bar{t}$. The distributions are plotted before requiring a top tagged jet and a W tagged jet. Signal is normalized to a cross section of 500pb. For these plots, the QCD background is normalized to the number of data events ($t\bar{t}$ subtracted). First row, from left to right: number of b tagged jets satisfying the ΔR and kinematic requirements ($p_T > 100$ GeV, $\Delta R(b,pt)$ leading fatjet) > 0.8 , $\Delta R(b,pt)$ subleading fatjet) > 0.8 , number of b tagged jets. Second row, from left to right: number of b tagged subjets, number of top tagged jets. Third row: number of W tagged jets.

The poor agreement between Data and prediction is due to the fact that the QCD multijet production is estimated with a MonteCarlo simulation in these plots. The QCD multijet MonteCarlo is not reliable in modeling both the normalization and the shape of distributions in these areas of the phase space. A dedicated data-driven procedure to estimate the QCD multijet production in the signal region, for the distribution of the Z' candidate mass will be developed in Section 4.

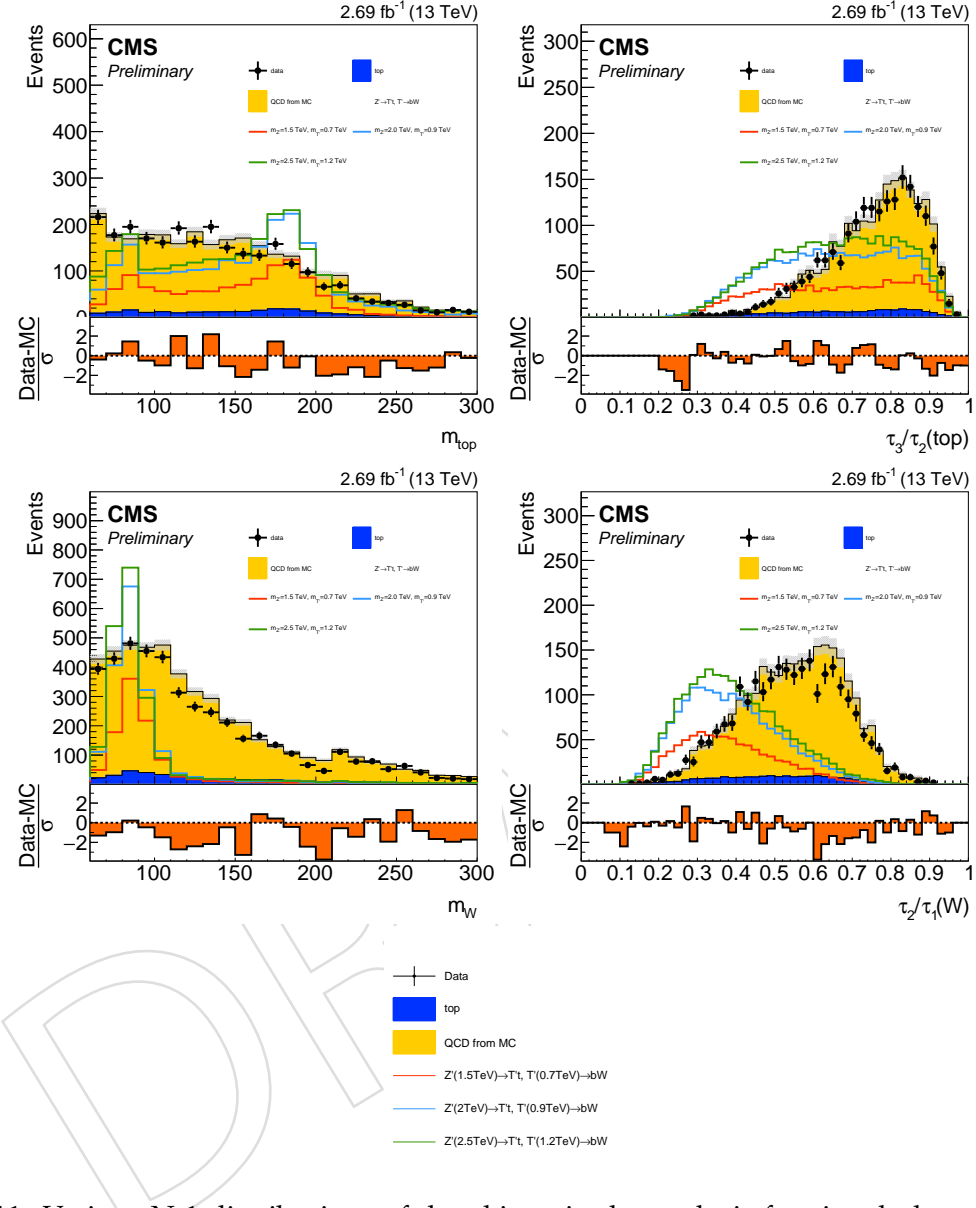


Figure 11: Various N-1 distributions of the objects in the analysis for signal, data, QCD, and ttbar. The distributions are plotted before cutting on the T' mass. Signal is normalized to a cross section of 10 pb. First row, from left to right: top jet softdrop mass, top jet n-subjettiness τ_3/τ_2 . Second row, from left to right: W jet softdrop mass, W jet n-subjettiness τ_2/τ_1 .

The poor agreement between Data and prediction is due to the fact that the QCD multijet production is estimated with a MonteCarlo simulation in these plots. The QCD multijet MonteCarlo is not reliable in modeling both the normalization and the shape of distributions in these areas of the phase space. A dedicated data-driven procedure to estimate the QCD multijet production in the signal region, for the distribution of the Z' candidate mass will be developed in Section 4.

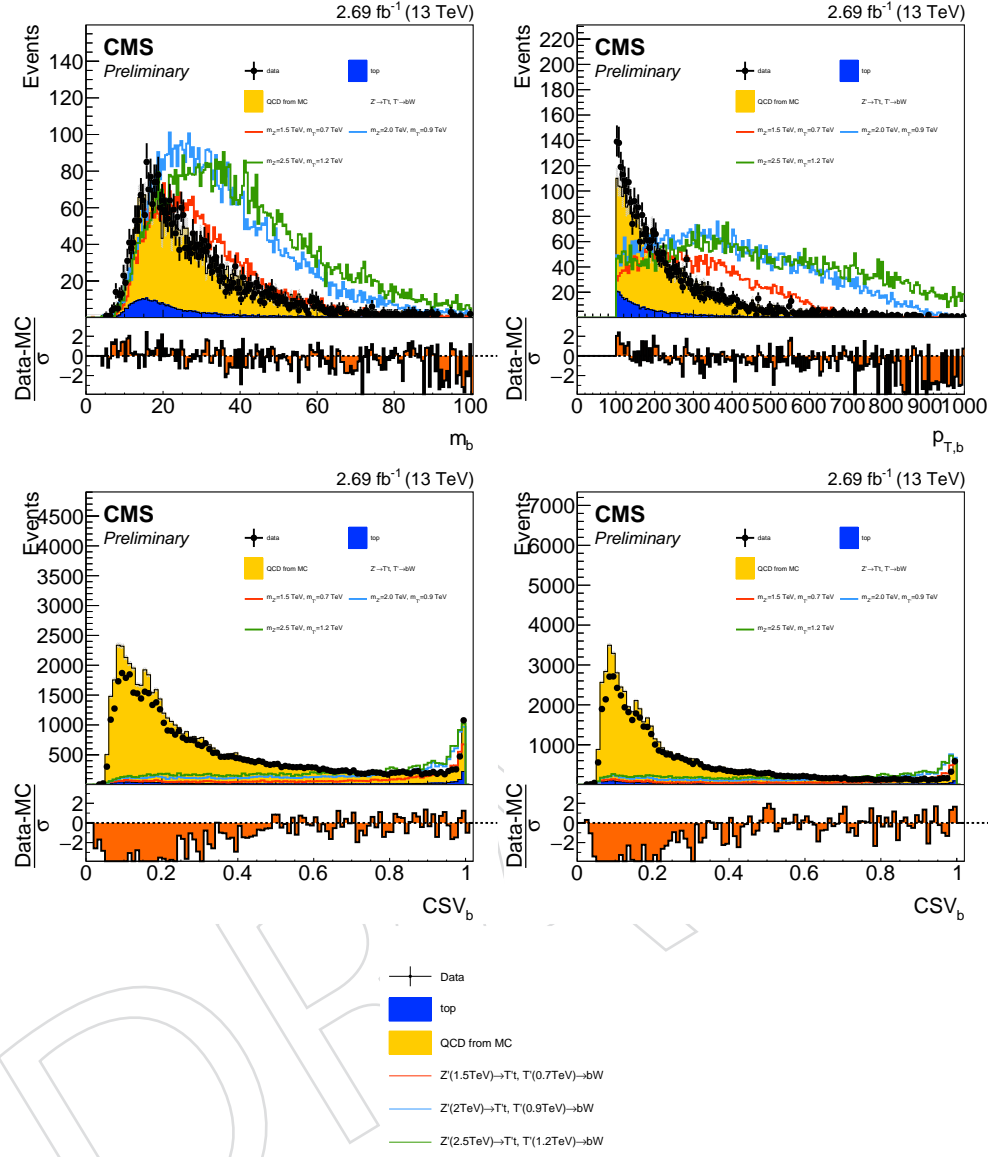


Figure 12: Various distributions of variables related to the b tagged jet. The distributions are plotted before after requiring a top tagged jet and a W tagged jet. First row, from left to right: b jet mass, b jet transverse momentum. Signal is normalized to a cross section of 40 pb. Second row: Left: the CSV discriminator of the jet with the highest CSV discriminator, satisfying the other selection criteria ($p_T, \Delta R$ with respect to large cone jets). Right: the CSV discriminator of the highest- p_T jet satisfying the other selection criteria.

The poor agreement between Data and prediction is due to the fact that the QCD multijet production is estimated with a MonteCarlo simulation in these plots. The QCD multijet MonteCarlo is not reliable in modeling both the normalization and the shape of distributions in these areas of the phase space. A dedicated data-driven procedure to estimate the QCD multijet production in the signal region, for the distribution of the Z' candidate mass will be developed in Section 4.

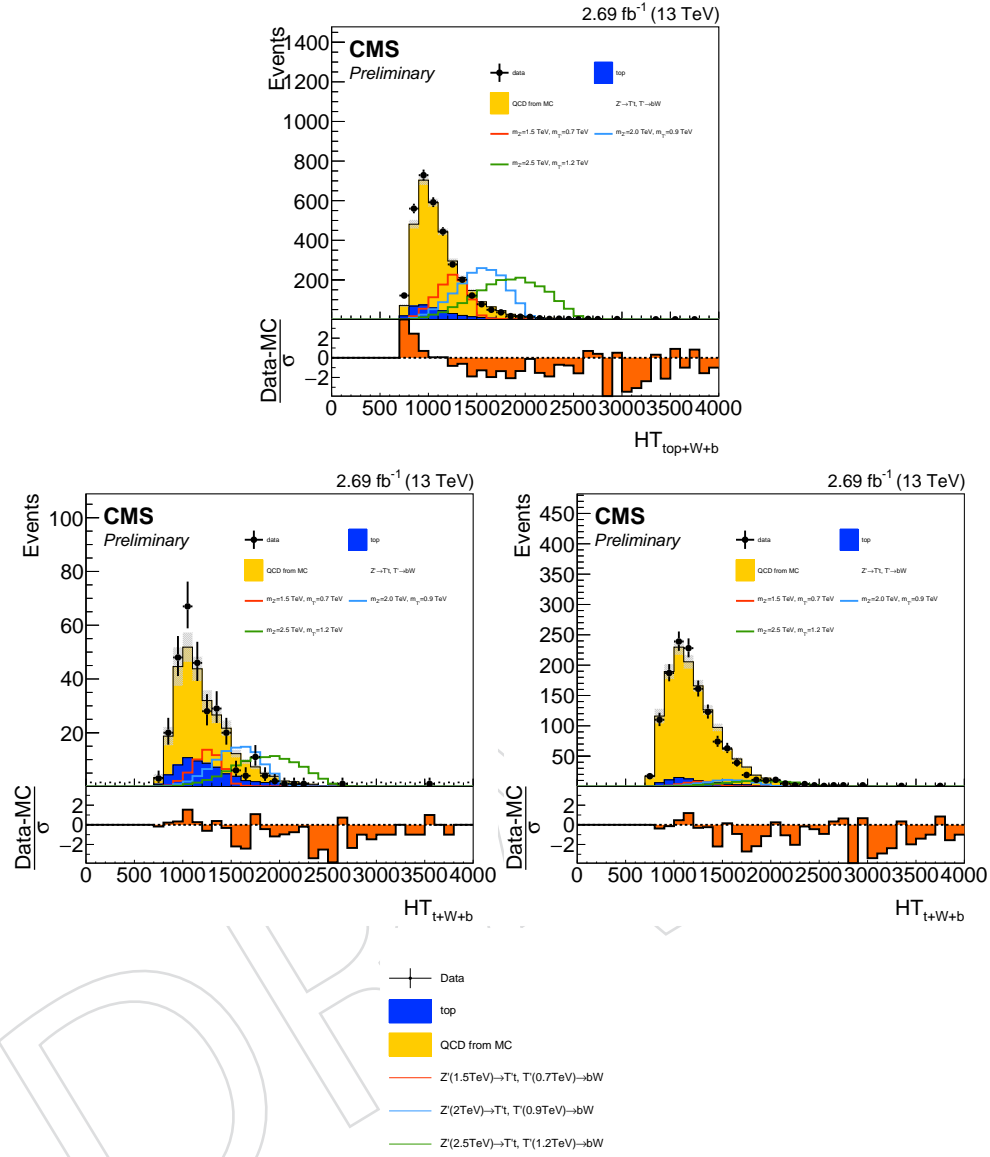


Figure 13: Distribution of HT_{twb} defined as the sum of the p_T of the top tagged jet, the W tagged jet and the b tagged jet. First row: before cutting on the T' mass. Signal normalized to a cross section of 10pb. Second row, from left to right: after cutting on the T' mass in the 2 btag category, after cutting on the T' mass in the 1 btag category. Signal normalized to a cross section of 1pb.

The poor agreement between Data and prediction is due to the fact that the QCD multijet production is estimated with a MonteCarlo simulation in these plots. The QCD multijet MonteCarlo is not reliable in modeling both the normalization and the shape of distributions in these areas of the phase space. A dedicated data-driven procedure to estimate the QCD multijet production in the signal region, for the distribution of the Z' candidate mass will be developed in Section 4.

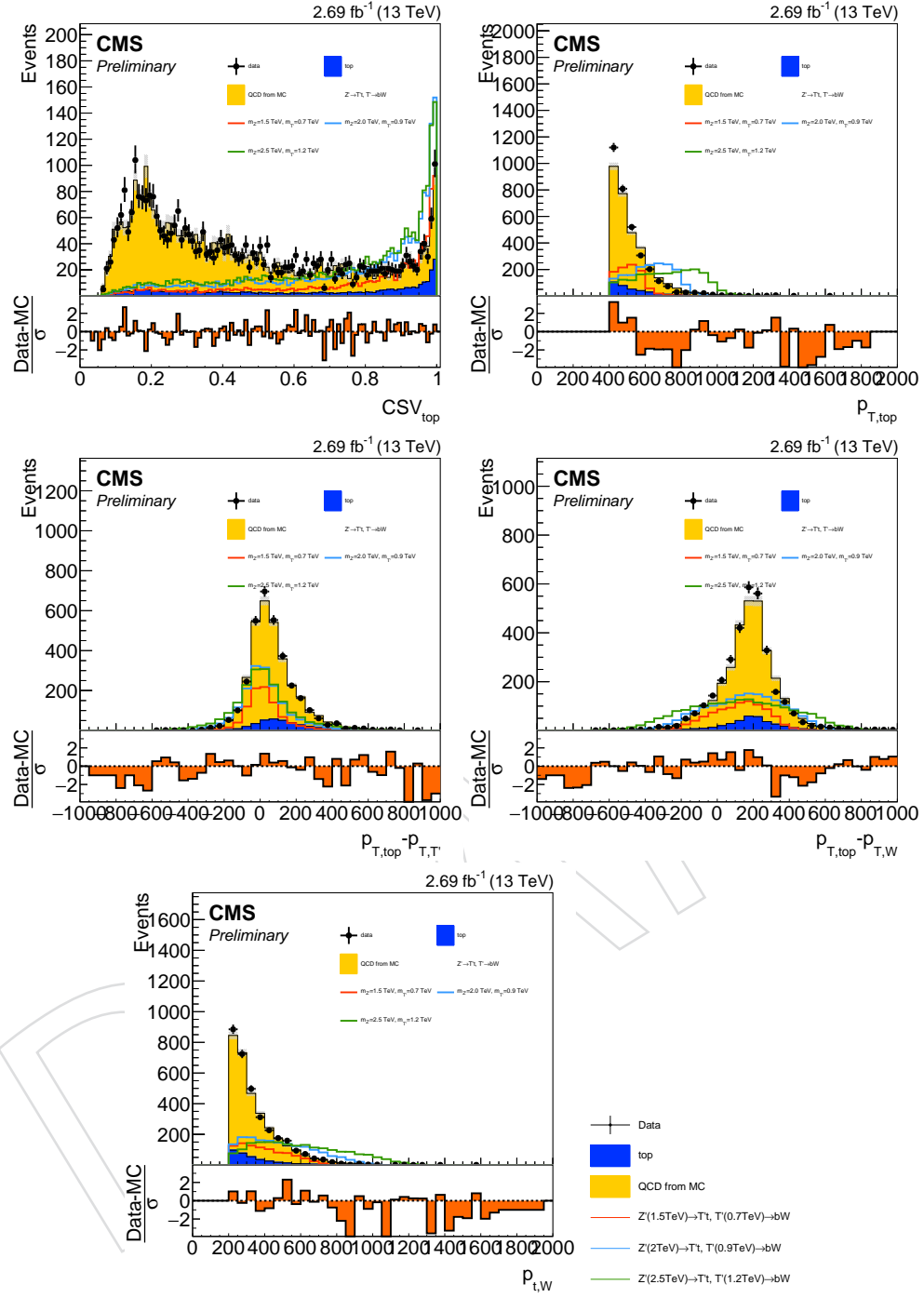


Figure 14: Distribution of various kinematic variables related to the top tagged jet and the W tagged jet. Plotted before the cut on the T' mass. Signal normalized to a cross section of 10pb. First row, from left to right: maximum CSV discriminator of the subjets of the top tagged jet, top tagged jet transverse momentum. Second row, from left to right: $p_{T,top} - (p_{T,W} + p_{T,T'})$, $p_{T,top} - p_{T,W}$. Third row: $p_{T,W}$.

The poor agreement between Data and prediction is due to the fact that the QCD multijet production is estimated with a MonteCarlo simulation in these plots. The QCD multijet MonteCarlo is not reliable in modeling both the normalization and the shape of distributions in these areas of the phase space. A dedicated data-driven procedure to estimate the QCD multijet production in the signal region, for the distribution of the Z' candidate mass will be developed in Section 4.

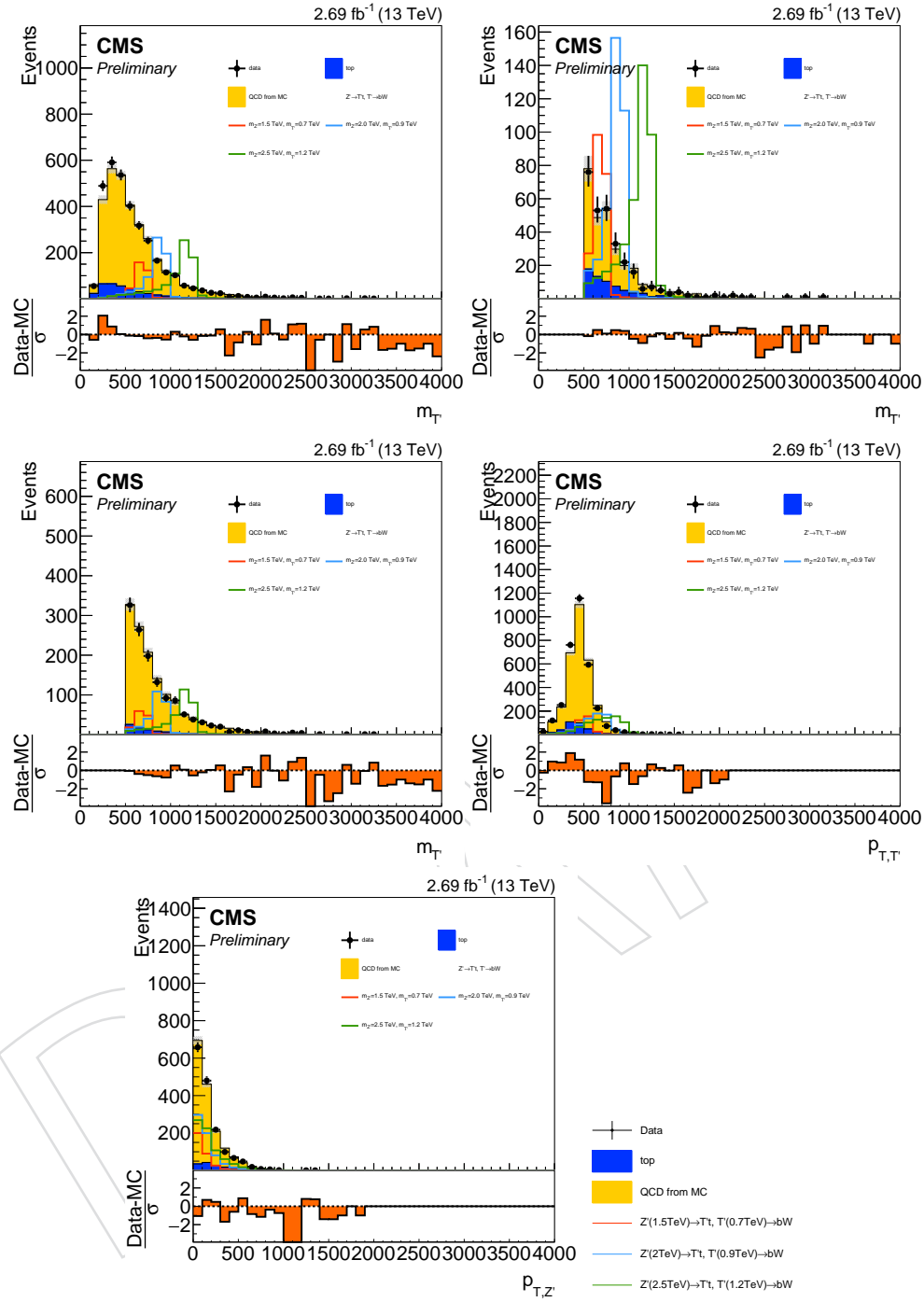


Figure 15: Distribution of various kinematic variables related to the T' candidate. Signal normalized to a cross section of 4 pb. First row, from left to right: T' mass before cutting on it, T' mass in the 2 b tag signal region. Second row, from left to right: T' mass in the 1 b tag signal region, T' transverse momentum. Third row: Z' candidate transverse momentum.

The poor agreement between Data and prediction is due to the fact that the QCD multijet production is estimated with a MonteCarlo simulation in these plots. The QCD multijet MonteCarlo is not reliable in modeling both the normalization and the shape of distributions in these areas of the phase space. A dedicated data-driven procedure to estimate the QCD multijet production in the signal region, for the distribution of the Z' candidate mass will be developed in Section 4.

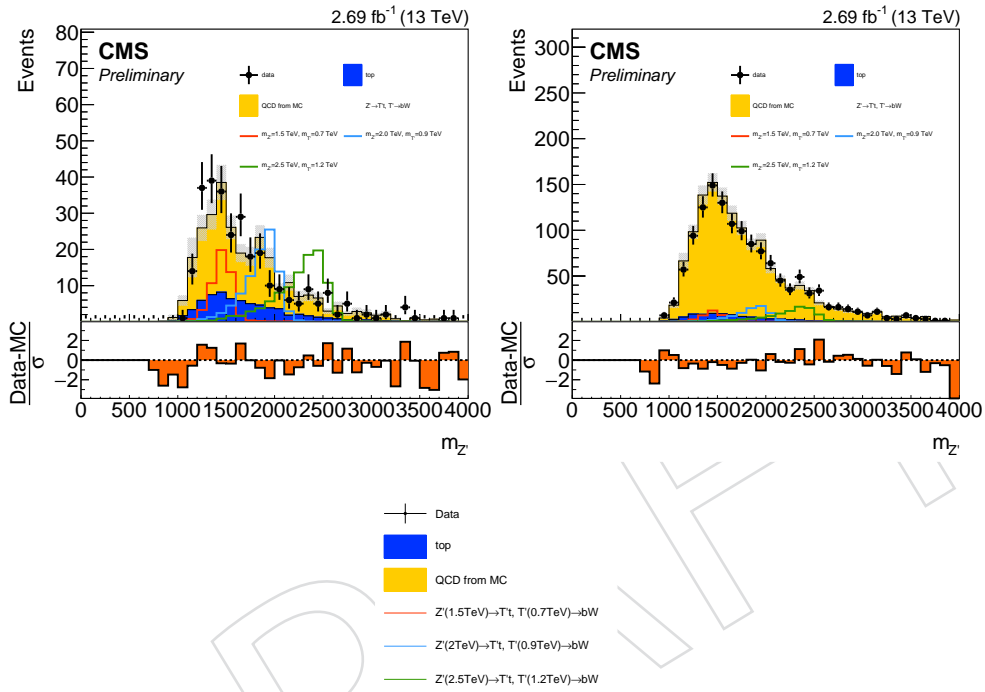


Figure 16: Distribution of the Z' candidate mass in the two signal regions, two b tags (left) and one b tag (right). Signal normalized to a cross section of 1pb. The QCD production is estimated from MonteCarlo in these plots.

The poor agreement between Data and prediction is due to the fact that the QCD multijet production is estimated with a MonteCarlo simulation in these plots. The QCD multijet MonteCarlo is not reliable in modeling both the normalization and the shape of distributions in these areas of the phase space. A dedicated data-driven procedure to estimate the QCD multijet production in the signal region, for the distribution of the Z' candidate mass will be developed in Section 4.

254 4 Background estimate

255 4.1 Top background estimate

256 Due to strong cuts on the invariant mass of the system composed by the W tagged jet and
 257 the b tagged jet (that is, the T' candidate), the signal region collects a very limited amount of
 258 events containing real top quarks with respect to multijet QCD production. This is true even
 259 for the category with 2 b tags, where the top background amounts to less than 10% of the total
 260 background. We decide to estimate the SM top contribution from MC using the ttbar and
 261 single top samples reported in the Samples section.

262 We decide to not apply any top- p_T reweighting to the events of the ttbar MC sample because
 263 the large systematic and statistical uncertainties affecting this minor background covers the
 264 possible shape variation due to the reweight (the renormalization and factorization scale alone
 265 have an impact of 30-44%). This shape variation would also have a minimal impact on the total
 266 background shape.

267 4.2 Non-top background estimate

268 The major background is composed by the Non-top component. In all hadronic analyses like
 269 this one, the main component of this background in multijet QCD production. QCD MC sam-
 270 ples are often not able to properly reproduce the real data in the corners of the phase space
 271 probed by BSM searches, thus we need a data-driven estimate of this background.

272 We use a sideband region defined in this way:

- 273 • a top tagged jet and a W tagged jet selected with the same criteria as the signal region
- 274 • veto on loose CSVv2 b tagged jets with the same kinematic criteria used for the signal
 region. This is the official loose operating point of the CSVv2 algorithm, yielding an
 efficiency of approximately 85%, and a rejection rate of light-flavor jet of 90% [13]
- 275 • an AK4 jet with $p_T > 100$ GeV, $\Delta R(\text{top jet}, \text{jet}) > 0.8$, $\Delta R(\text{W jet}, \text{jet}) > 0.8$, CSVv2
 discriminator smaller than the loose operating point
- 276 • the T' candidate reconstructed as the sum of the 4-vectors of the W tagged jet and
 the anti b tagged jet is required to have a mass larger than 500 GeV.

277 The loose b tag veto is used instead of the medium working point because it reduces the signal
 278 contamination in the sideband region, while having a limited impact on their statistics.

279 The pseudo Z' candidate in the sideband region is obtained by summing the 4-vectors of the
 280 top tagged jet, the W tagged jet, and the additional anti-tagged AK4 jet. The mass distribution
 281 of the Z' candidate can be seen in Fig. 17. Here the QCD has been scaled to match the number
 282 of events in data (taking into account the top background). The sidebands contain ca. 10 times
 283 more background than the signal regions.

284 We want to use the (properly corrected) shape of the sideband region to estimate the shape of
 285 the signal region. A comparison of the two shapes in QCD MC (both normalized to 1) can be
 286 seen in Fig. 18. It can be seen that the shapes of the signal region and the sideband region do
 287 not match perfectly, but there is a trend in the discrepancy that can be modeled. Hence the
 288 need for shape corrections.

289 We plan to derive sideband-to-signal-region corrections from the QCD MC sample and then
 290 apply these correction to the sideband in Data to obtain an estimate of the control region. Fig.
 291 19 shows the ratio of QCD MC in signal over sideband region. The ratio is plotted as a function
 292 of Z mass and is fitted with a parabola. The parabola fits the points well (see fit parameters

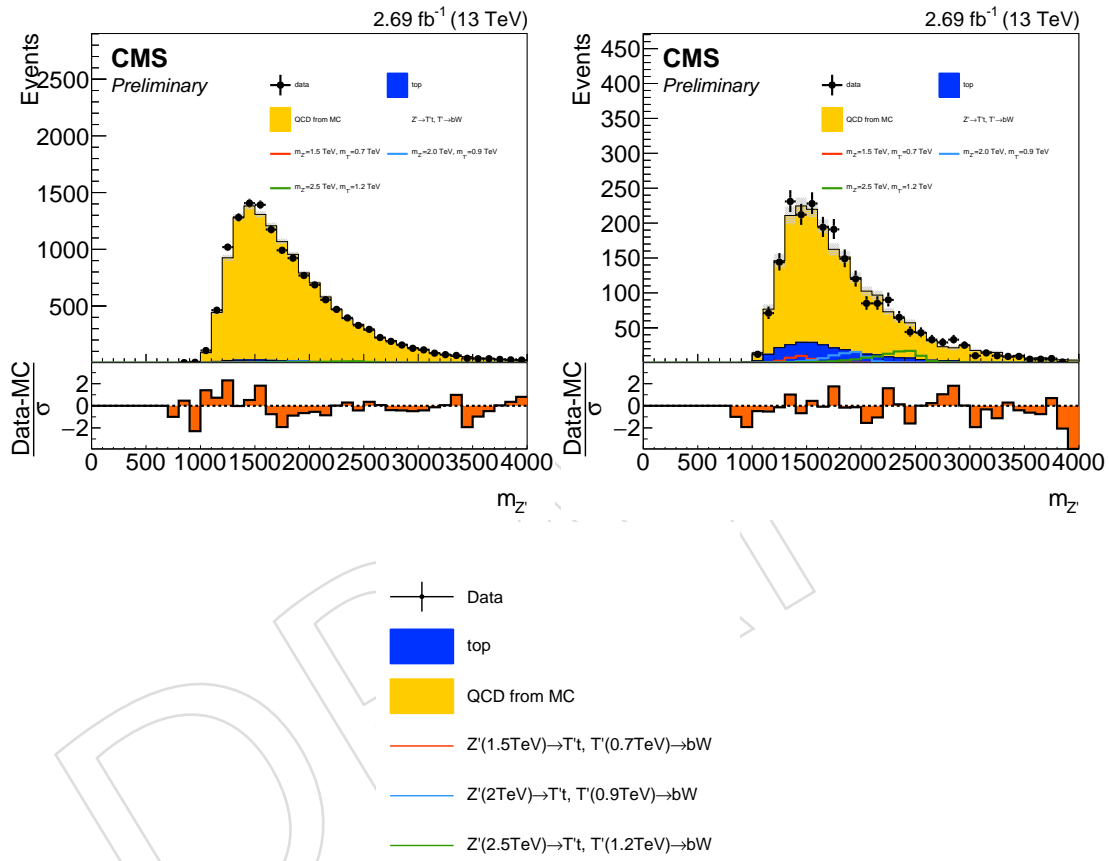


Figure 17: Distribution of the invariant mass of the Z' pseudo-candidate in the sideband region. Left: no subjet b tag, right: the top jet has at least one b tagged subjet. Here the QCD has been scaled to match the number of events (taking into account the top background).

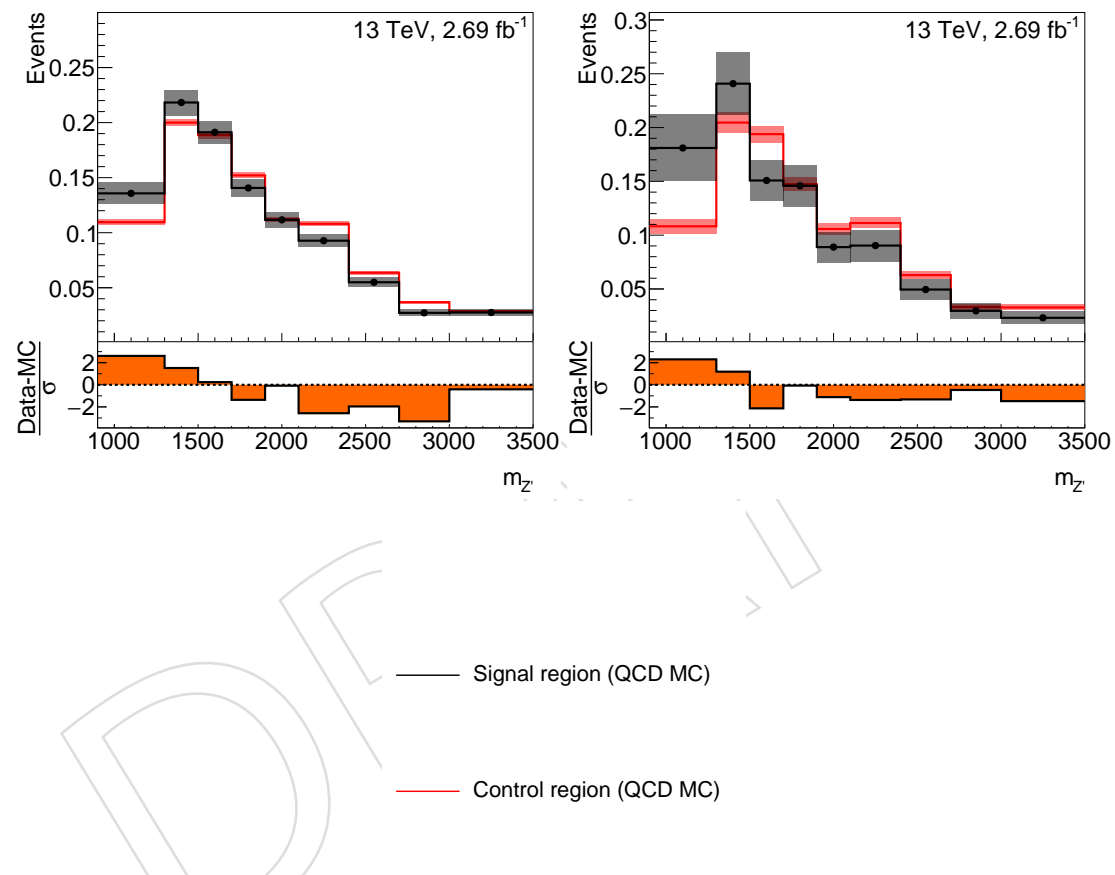


Figure 18: Shape comparison of the Z' mass candidate distribution in the signal region and in the sideband region in QCD MC. Left: no subjet b tag, right: the top jet has at least one b tagged subjet.

297 on the plot) except for the first bin, which is however affected by large uncertainties. We use
 298 the fitted function as the correction factor, that is, we weight each event of the sideband region
 299 with a value corresponding to the point of the parabola the event belongs to. There are two
 300 correction functions for the two categories in the analysis.

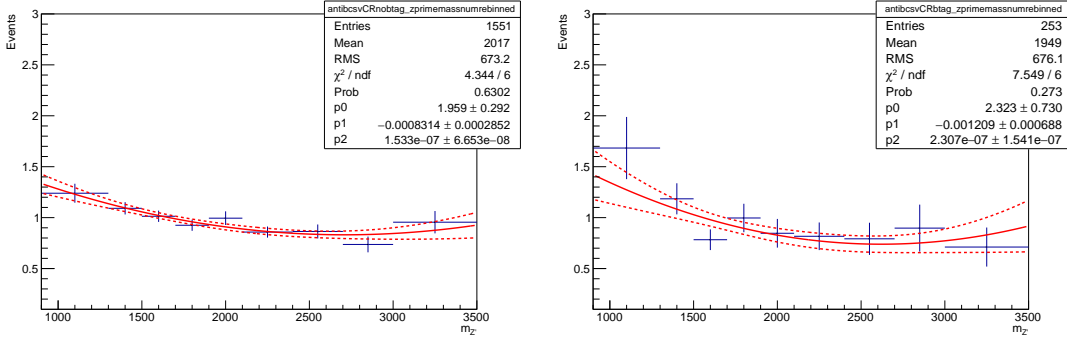


Figure 19: Signal region over sideband region shape ratio for QCD MC. Fitted with a parabola. Left: no subjet b tag, right: the top jet has at least one b tagged subjet.

301 The possibility of a different fitting functional form is explored. Fig. 20 shows the ratio signal
 302 region over sideband region in QCD MC, this time fitted with a straight line. In the current
 303 version of the analysis the systematic uncertainty on the procedure is estimated by using the fit
 304 parameter errors and by comparing the shape weighted with the straight line fit.

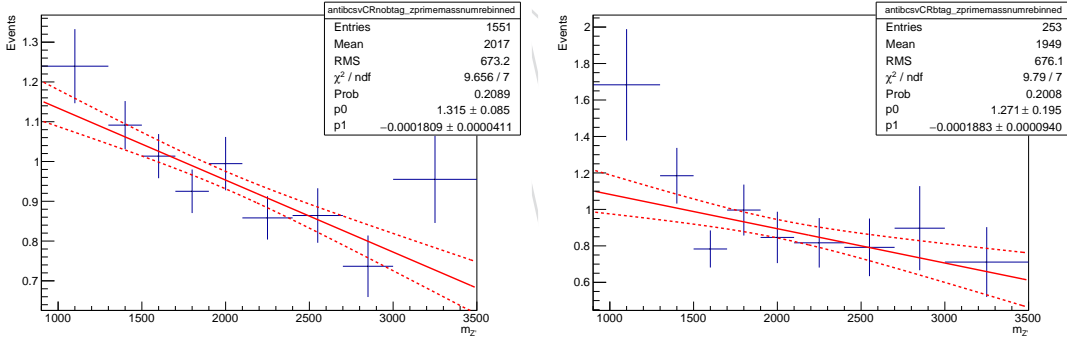


Figure 20: Signal region over sideband region shape ratio. Fitted with a straight line. Left: no subjet b tag, right: the top jet has at least one b tagged subjet.

305 We validate the procedure on QCD MC performing a closure test. We apply the reweight to
 306 the sideband region and compare the corrected shape, with the shape of the signal region. The
 307 result is shown in Fig 21, which show a satisfying agreement between the signal region and the
 308 corrected sideband region shape.

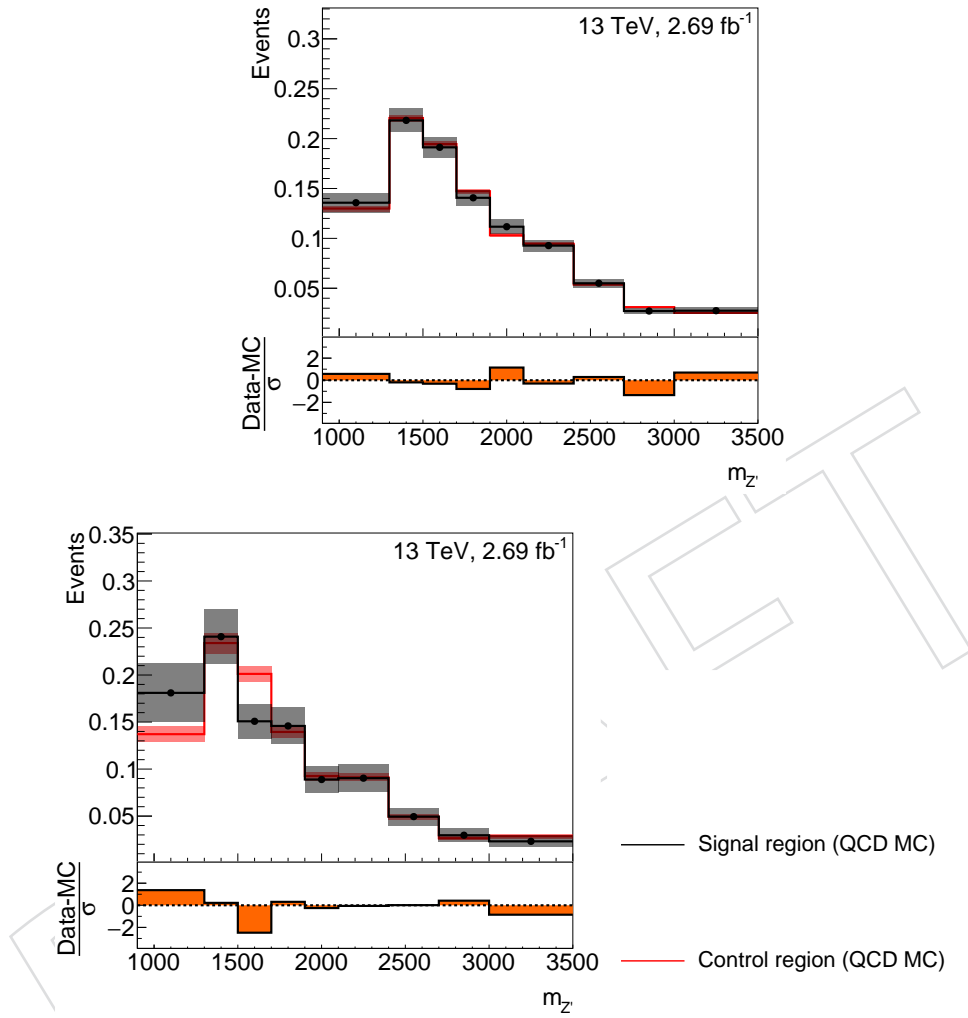


Figure 21: Closure test: comparison of the shape of the signal region (invariant mass of the Z' candidate) with the corrected shape of the sideband region in QCD MC. Left: no subjet b tag, right: the top jet has at least one b tagged subjet.

309 Additionally we also plot in Fig 22 the ratio between the signal region and the corrected side-
 310 band and we fit it with a straight line. The parameters of the line are compatible with a flat
 311 straight line.

312 To study how much the presence of a signal would impact the background estimate, we con-
 313 taminate the QCD MC sideband region with signal normalized to 1pb and propagate it through
 314 the background estimation procedure. We then compare the contaminated background esti-
 315 mate with the observed background in signal region and with the signal (with the same cross
 316 section) observed in the signal region. This is shown in Figs. 23 and 24 for the two categories
 317 and for different signals.

318 In Table 5 we report the contamination percentage of a 1pb signal in the sideband region used

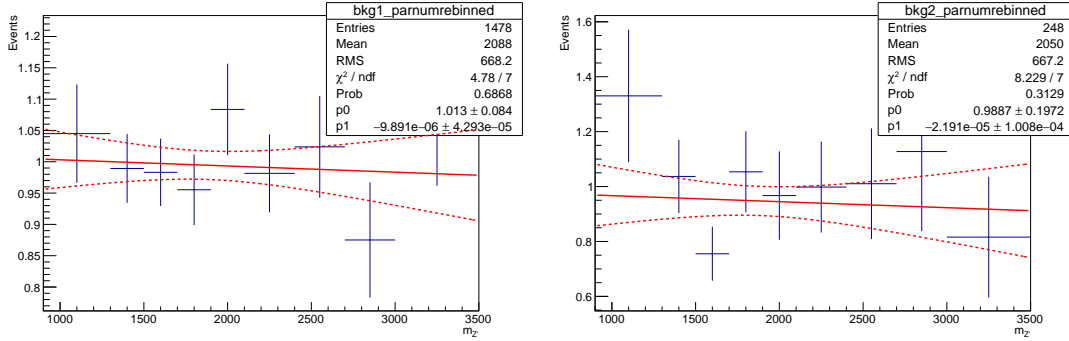


Figure 22: Closure test: ratio between the shape of the signal region (invariant mass of the Z' candidate) and the corrected shape of the sideband region in QCD MC. Fitted with a straight line. Left: no subjet b tag, right: the top jet has at least one b tagged subjet.

Signal	Sig./QCD in sideband 1 btag	Sig./QCD in sideband 2 btag
$Z'(1.5 \text{ TeV}) \rightarrow T't, T'(0.7 \text{ TeV}) \rightarrow bW$	0.14%, 18 sig. ev.	1.59%, 30 sig. ev.
$Z'(2.0 \text{ TeV}) \rightarrow T't, T'(0.9 \text{ TeV}) \rightarrow bW$	0.34%, 45 sig. ev.	3.11%, 57 sig. ev.
$Z'(2.5 \text{ TeV}) \rightarrow T't, T'(1.2 \text{ TeV}) \rightarrow bW$	0.47%, 62 sig. ev.	3.80%, 60 sig. ev.

Table 5: Contamination percentage of a 1pb signal in the sideband region (weighted with the parabola function) used to estimate the background procedure, for different mass points.

319 to estimate the background procedure, for different mass points, in Table 6 we report the ratio
 320 between the scaled and weighted signal in the sideband region and the signal in the sideband
 321 region.

322 To obtain the QCD estimate from the reweighted sideband from Data we subtract the estimated
 323 contribution from top background in the sideband using a MC prediction.

324 The last point before using the background estimate is to fix the normalization. We perform a
 325 MLE fit of the data-driven background plus top background to the signal region in data in the
 326 no-signal hypothesis, using a flat prior for the background normalization nuisance parameter
 327 using the theta package. The fit result is: 0.996 times the normalization obtained from a simple
 328 event number count. The full scale factors are $SF(1 \text{ btag}) = 0.093 \times 0.996$ and $SF(2 \text{ btag}) =$
 329 0.12×0.996 . The fit uncertainty is 2.8%.

330 The distribution of the reconstructed Z' mass in the signal region, using the data-driven back-
 331 ground estimated is shown in Fig 25. These are the final plots used as input for the limit setting
 332 (along with the systematic variations and all the other signals). The errors bar shown for data
 333 are computed using poissonian statistics. The full impact of systematic and statistical errors
 334 are shown in the gray bands for background. The combination of the total error for data and
 335 background is used to compute the uncertainty for the pull in the bottom panel.

Signal	Scaled Sig. SB / Signal SR 1 btag	Scaled Sig. SB / Signal SR 2 btag
$Z'(1.5 \text{ TeV}) \rightarrow T't, T'(0.7 \text{ TeV}) \rightarrow bW$	5.13%	7.19%
$Z'(2.0 \text{ TeV}) \rightarrow T't, T'(0.9 \text{ TeV}) \rightarrow bW$	5.99%	7.71%
$Z'(2.5 \text{ TeV}) \rightarrow T't, T'(1.2 \text{ TeV}) \rightarrow bW$	6.66%	8.71%

Table 6: Ratio between the scaled and weighted signal in the sideband region and the signal in the signal region, for different mass points.

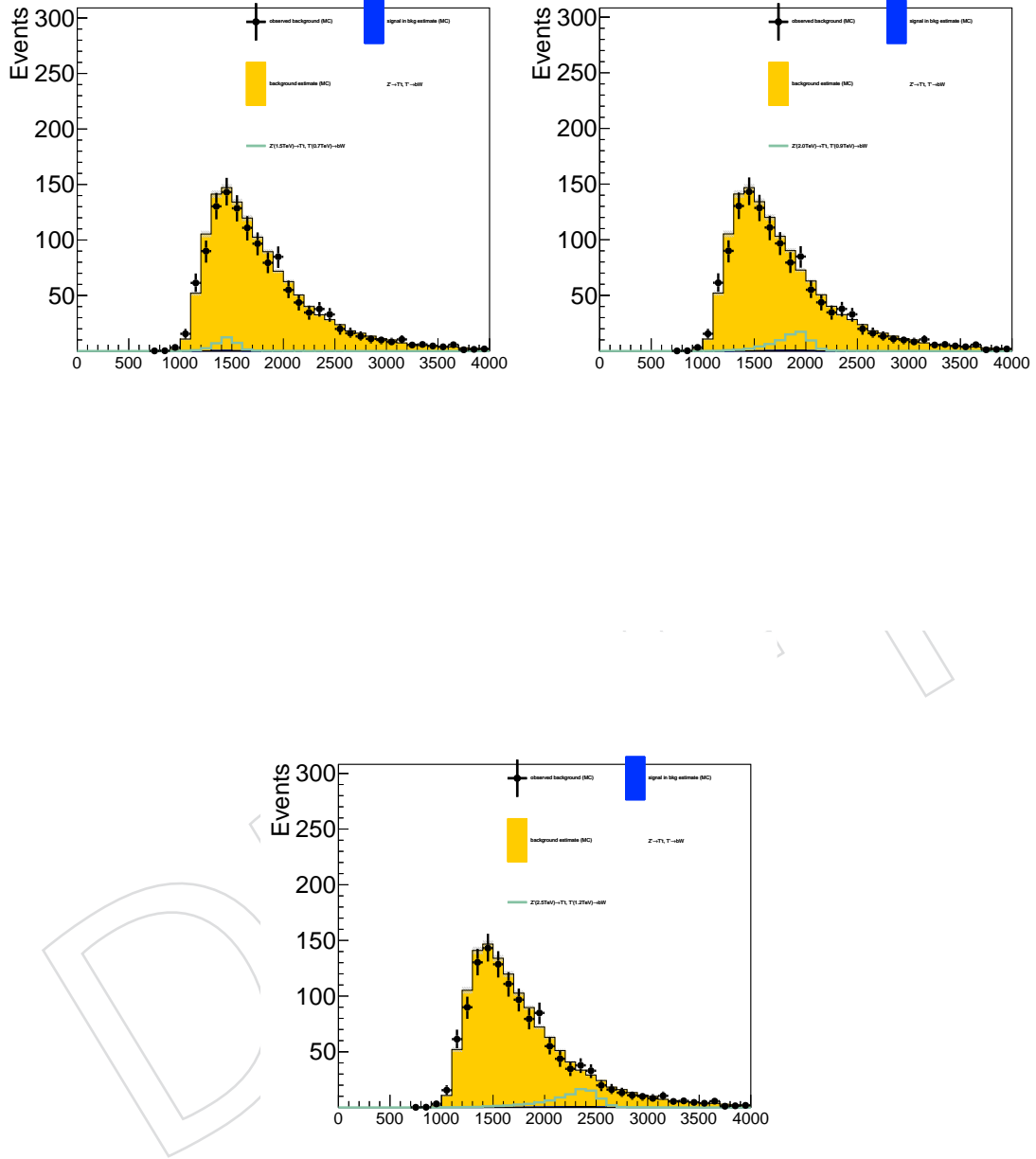


Figure 23: Signal contamination study for the no subjet btag category: the sideband region is contaminated with a 1pb signal (different mass points in the different plots). The signal is propagated through the background estimation procedure. The yellow area is the predicted background component in the signal region coming from QCD, while the blue area is the one coming from the signal in the background estimate. The dots represent the observed background component coming from QCD, while the overlayed green line is the observed signal.

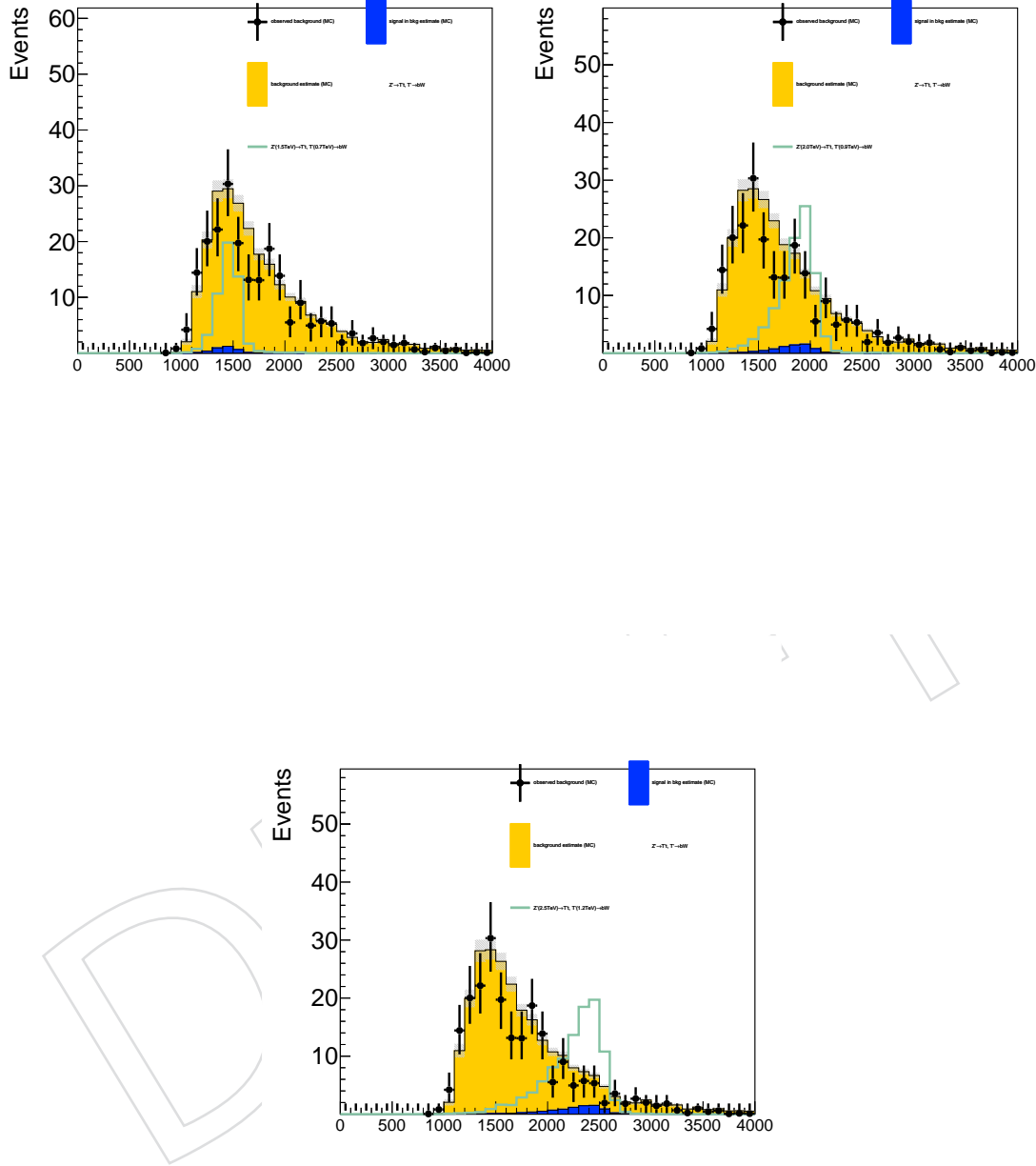


Figure 24: Signal injection study for the subjet btag category: the sideband region is contaminated with a 1pb signal (different mass points in the different plots). The signal is propagated through the background estimation procedure. The yellow area is the predicted background component in the signal region coming from QCD, while the blue area is the one coming from the signal in the background estimate. The dots represent the observed background component coming from QCD, while the overlayed green line is the observed signal.

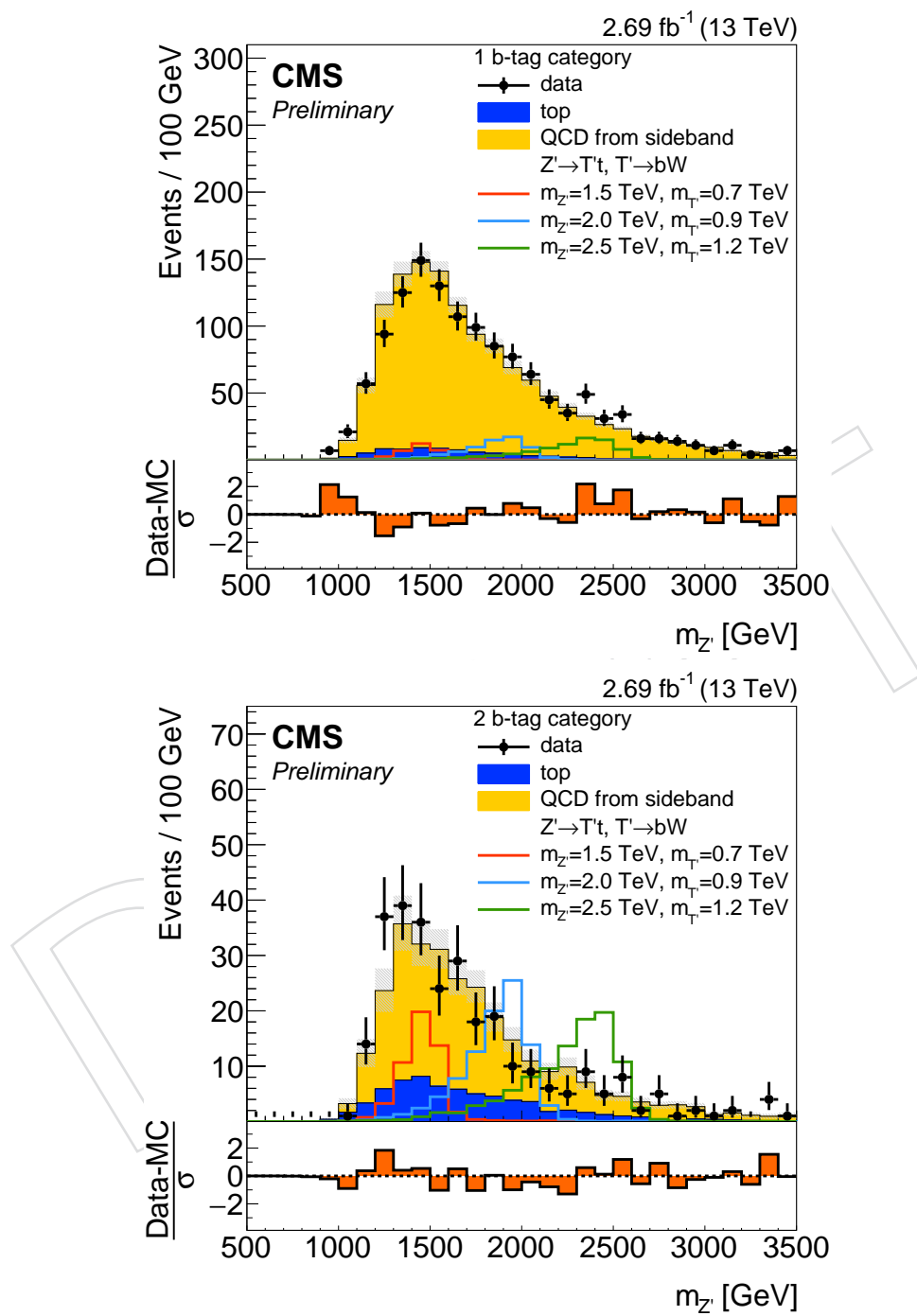


Figure 25: Signal region: invariant mass of the Z' candidate with data-driven non-top background estimate. First row: no subjet btag category, second row: subjet btag category

336 The QCD background estimate is able to model reasonably well other kinematic variables in
 337 the signal region. In Fig 26 the distribution of the T' candidate mass and the HT calculated
 338 as the sum of the p_T of the three jets used in the event is shown after all the full background
 339 estimation procedure.

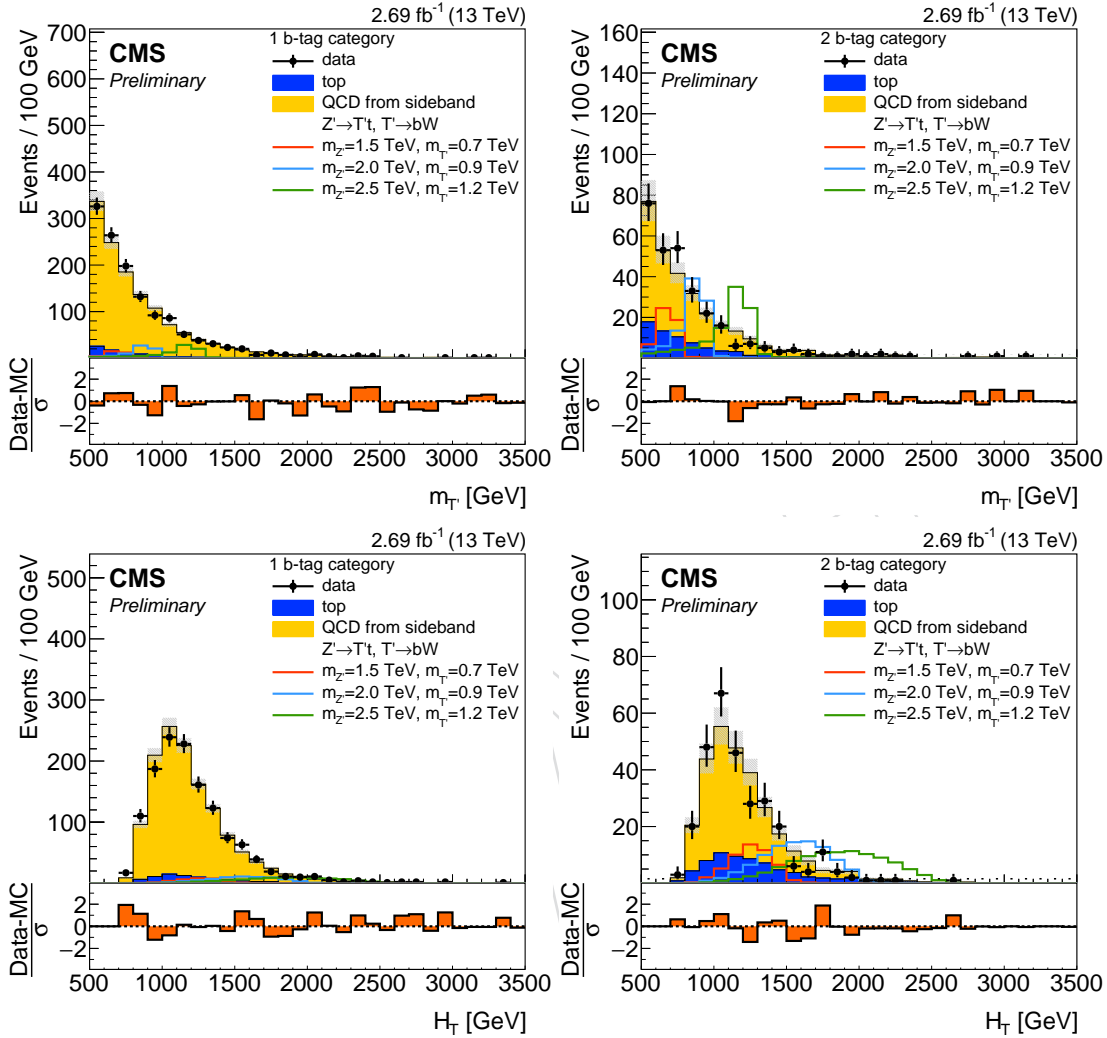


Figure 26: Plots of additional variables in the signal region after the full background estimate procedure: First row: T' candidate invariant mass in the 1 b tag category on the left and the 2 b tag category on the right. Second row: HT calculated as the sum of the p_T of the three jets used in the event in the 1 b tag category on the left and the 2 b tag category on the right.

340 5 Systematics

341 The scope of this section is to describe and summarize the systematic uncertainties propagated.

- 342 • Data-driven multijet background derivation procedure: shape and rate uncertainty.
 343 One sigma variation of the fit parameter errors. Correlation between the fit parameters
 344 is properly taken into account. Additionally the difference between the shape reweighted with the parabola weight function and the straight line function is taken
 345 into account as a systematic separately (shape+rate). The normalization procedure
 346 of the QCD background is assigned a 50% rate uncertainty.
 347

- 348 • Factorization and normalization scale: shape and rate uncertainty. Variation of the
 349 six possible combinations of renormalization and factorization scale ($\mu_{R,up} + \mu_{F,up}$,
 350 $\mu_{R,down} + \mu_{F,down}$, $\mu_{R,avg} + \mu_{F,up}$, $\mu_{R,avg} + \mu_{F,down}$, $\mu_{R,avg} + \mu_{F,up}$, $\mu_{R,avg} + \mu_{F,down}$) ac-
 351 cording to the weight values provided in the MC samples. Subsequently, for every
 352 bin, for every plot, the envelope of the six variations is considered as the up and
 353 down variation. Applied to $t\bar{t}$ and signal samples. Correlated among the signal
 354 region categories.
- 355 • B tagging on AK4 jets: shape and rate uncertainty. Variation of the light and heavy
 356 flavour scale factors by 1σ . Applied to $t\bar{t}$ and signal samples. Correlated among the
 357 signal region categories. Light and heavy flavours correlated. Correlated with subjet
 358 b tagging variation [13].
- 359 • B tagging on subjets: shape and rate uncertainty. Variation of the light and heavy
 360 flavour scale factors by 1σ . Applied to $t\bar{t}$ and signal samples. Correlated among the
 361 signal region categories. Light and heavy flavours correlated. Correlated with AK4
 362 b tagging variation [13].
- 363 • Jet energy calibration: shape and rate uncertainty. Variation of 1σ of the uncertainties
 364 on the calibration scale factors. Applied to $t\bar{t}$ and signal samples. Correlated among
 365 the signal region categories. Correlated between AK4 jets, AK8 jets, and AK8 subjets.
- 366 • Jet energy resolution (jet smearing): shape and rate uncertainty. Variation of 1σ of
 367 the uncertainties on the smearing scale factors. Applied to $t\bar{t}$ and signal samples.
 368 Correlated among the signal region categories. Correlated between AK4 and AK8
 369 jets.
- 370 • Luminosity: 2.7% flat rate uncertainty. Applied to $t\bar{t}$ and signal samples. Correlated
 371 among the signal region categories.
- 372 • Pileup: shape and rate uncertainty. Variation of the pileup cross section from the
 373 base value of 69mb to 65.6mb and 72.5mb. The variation is propagated to the pileup
 374 reweight procedure. Applied to $t\bar{t}$ and signal samples. Correlated among the signal
 375 region categories.
- 376 • Top tagging scale factors: shape and rate uncertainty. Variation of 1σ of the uncer-
 377 tainty on the top tagging scale factors. Applied to $t\bar{t}$ and signal samples. Correlated
 378 among the signal region categories.
- 379 • Trigger: 3% flat rate uncertainty. Applied to $t\bar{t}$ and signal samples. Correlated
 380 among the signal region categories.
- 381 • W tagging scale factors: shape and rate uncertainty. Variation of 1σ of the uncer-
 382 tainty on the top tagging scale factors. Applied to $t\bar{t}$ and signal samples. Correlated
 383 among the signal region categories.
- 384 • PDF: shape and rate uncertainty. RMS of the 100 eigenvalues of the chosen PDF set,
 385 calculated bin by bin.
- 386 • ttbar cross section: 15% rate-only uncertainty.

387 6 Results

- 388 As no excess of events is found in the signal region, we proceed to set cross section limits on
 389 the production of the signal. We use the theta framework to set limits. The bayesian approach
 390 is used. The systematics included are reported in the previous chapter of the note.
- 391 Table 7 report the number of selected events in the signal region categories for Data, and the

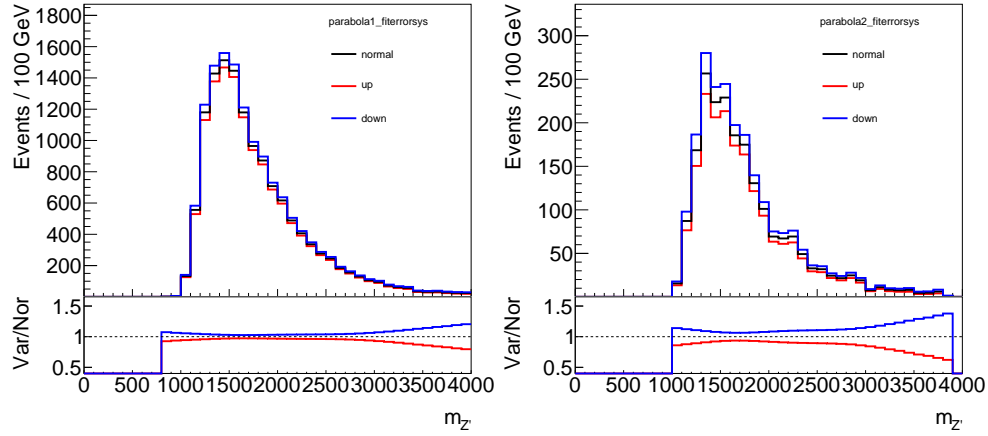


Figure 27: Impact of the QCD background systematic (fit parameter error) for the 1 btag category (left) and the 2 btag category (right).

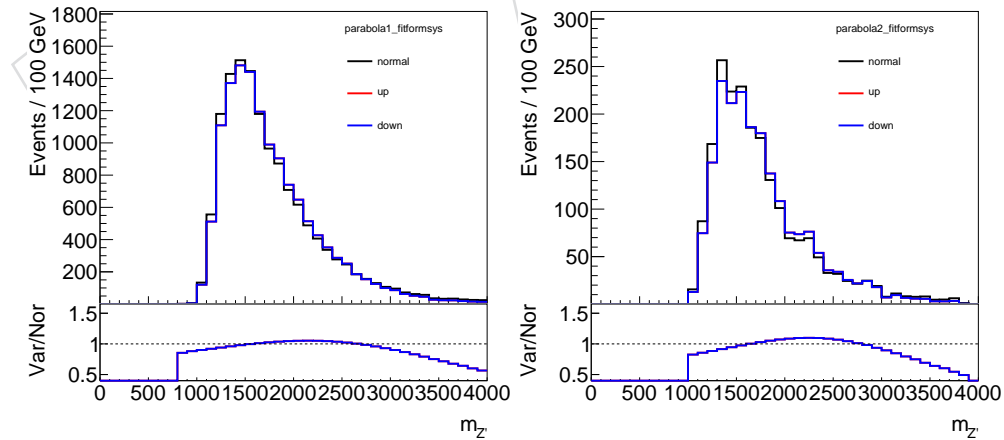


Figure 28: Impact of the QCD background systematic (fit functional form) for the 1 btag category (left) and the 2 btag category (right).

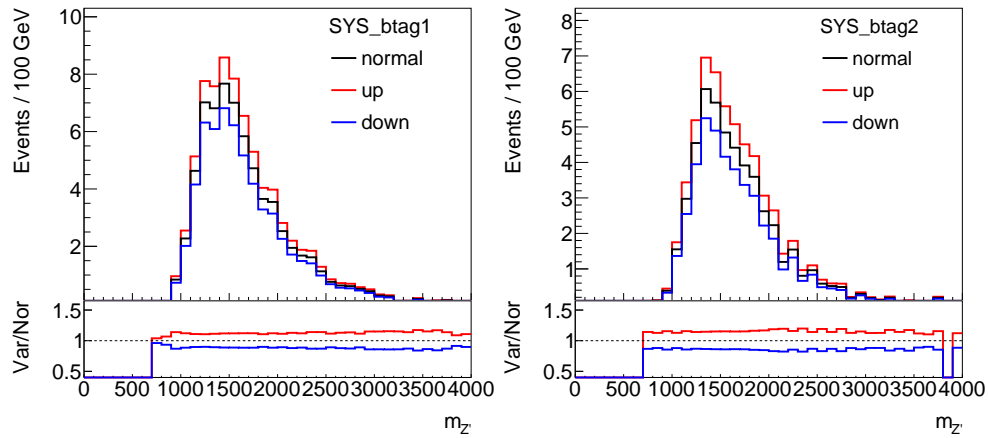


Figure 29: Impact of the btagging systematic on the ttbar MC sample for the 1 btag category (left) and the 2 btag category (right).

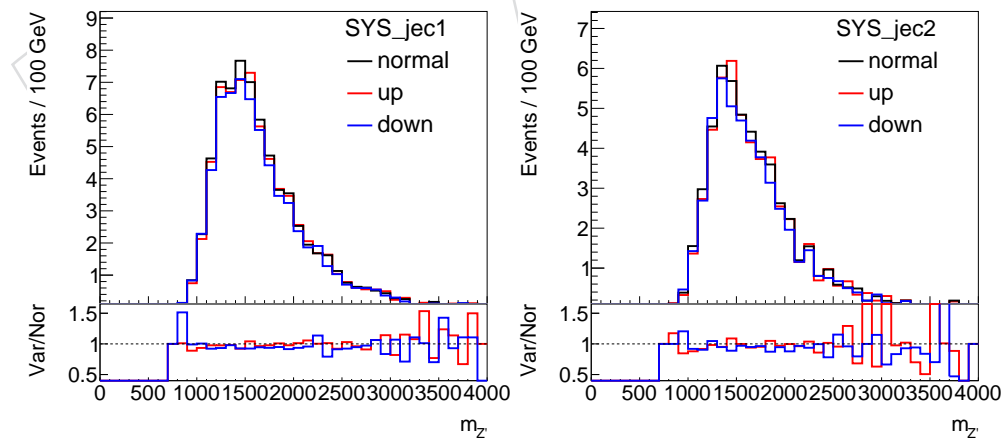


Figure 30: Impact of the JEC systematic on the ttbar MC sample for the 1 btag category (left) and the 2 btag category (right).

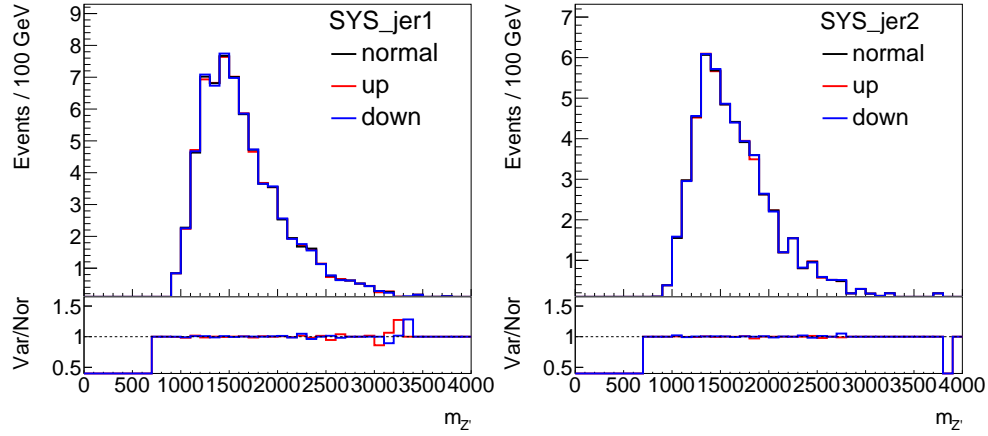


Figure 31: Impact of the JER systematic on the $t\bar{t}$ MC sample for the 1 btag category (left) and the 2 btag category (right).

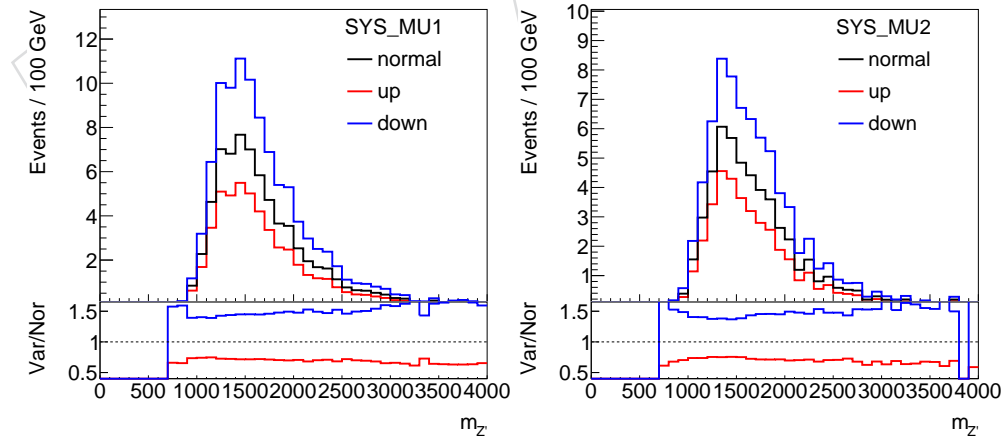


Figure 32: Impact of the renormalization and factorization scale systematic on the $t\bar{t}$ MC sample for the 1 btag category (left) and the 2 btag category (right).

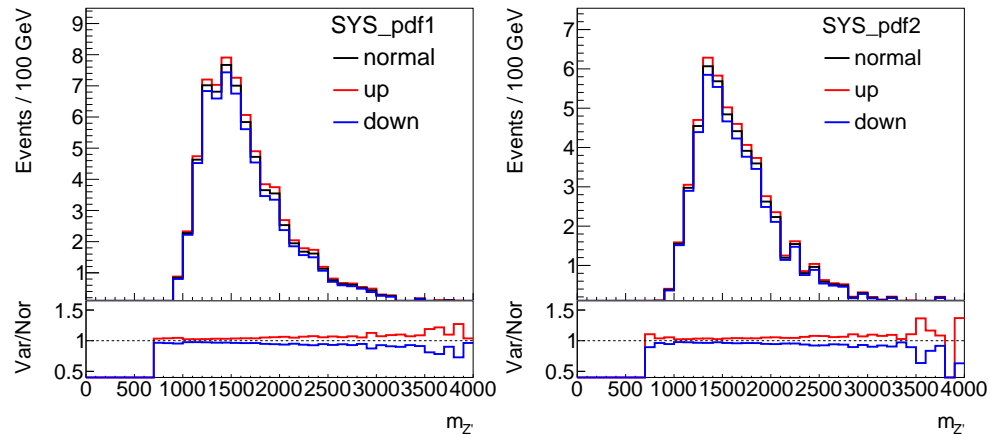


Figure 33: Impact of the PDF systematic on the $t\bar{t}$ MC sample for the 1 btag category (left) and the 2 btag category (right).

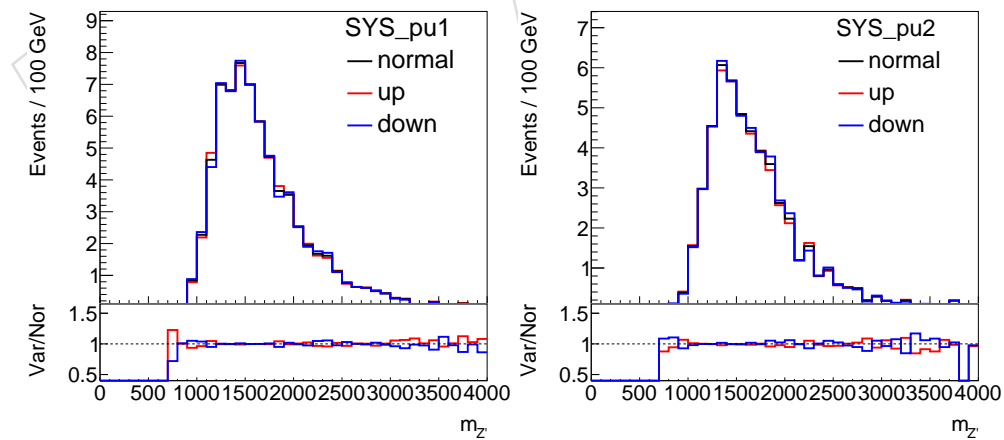


Figure 34: Impact of the pileup reweight systematic on the $t\bar{t}$ MC sample for the 1 btag category (left) and the 2 btag category (right).

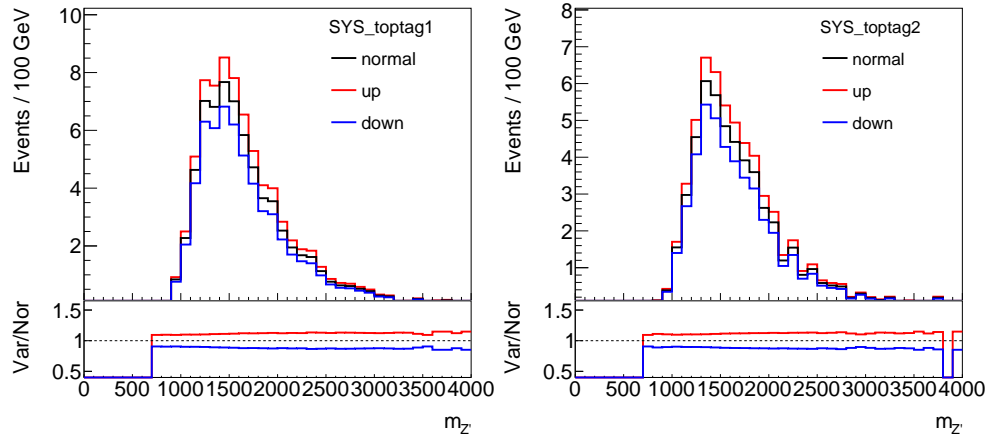


Figure 35: Impact of the Top tagging systematic on the ttbar MC sample for the 1 btag category (left) and the 2 btag category (right).

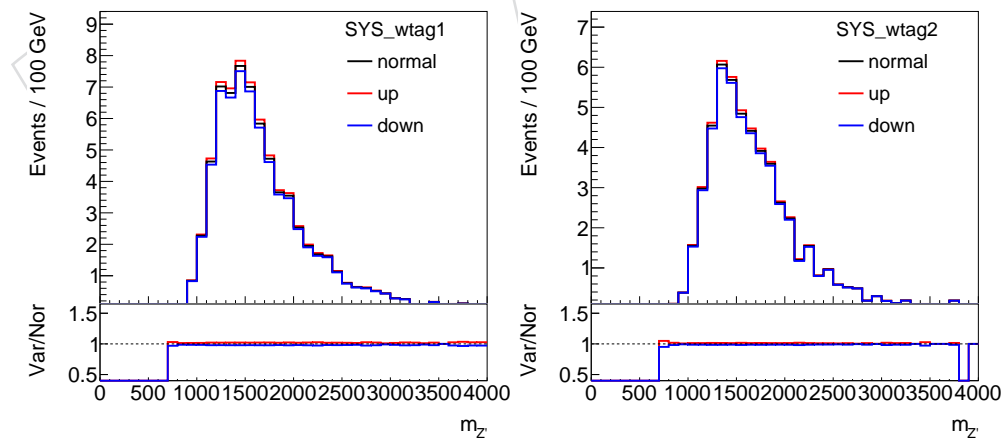


Figure 36: Impact of the W tagging systematic on the ttbar MC sample for the 1 btag category (left) and the 2 btag category (right).

Sample	N. of events 1 b-tag cat.	N. of events 2 b-tag cat.
Multijet QCD	1226^{+59}_{-59}	221^{+22}_{-22}
SM top	83^{+34}_{-26}	68^{+25}_{-20}
Total background	1309^{+68}_{-64}	289^{+33}_{-30}
DATA	1307	289

Table 7: Number of events in the different event categories of the analysis. The uncertainty quoted includes both the statistical and systematic components.

		T' \rightarrow bW signal hypothesis						
Z' mass (TeV)	T' mass (TeV)	Obs. 95% CL limit (pb)	Expected 95% CL limits (pb)					
			-2σ	-1σ	Median	$+1\sigma$	$+2\sigma$	
1.5	0.7	0.80	0.30	0.44	0.66	0.97	1.5	
1.5	0.9	1.5	0.66	0.92	1.4	2.0	3.4	
1.5	1.2	8.6	3.6	5.0	7.7	12	23	
2.0	0.9	0.21	0.16	0.23	0.35	0.55	0.92	
2.0	1.2	0.27	0.23	0.33	0.48	0.73	1.2	
2.0	1.5	0.90	0.81	1.2	1.7	2.9	5.0	
2.5	1.2	0.33	0.11	0.15	0.23	0.38	0.64	
2.5	1.5	0.29	0.11	0.15	0.22	0.37	0.67	

Table 8: Table of expected and observed 95% CL cross section limits, for the T' \rightarrow bW signal hypothesis.

392 various background considered.

393 We report the rate impact for every systematic included in the analysis in Figs 37,38,39.

394 The observed and expected limits and their relative uncertainties can be seen in Tables 8 9 10.

395 We provide the observed and expected cross section limits for all possible branching fraction
396 combinations of the T' in Figs 40,41 No mass limits can be obtained at the moment as there
397 is no generic theory prediction to be used as a benchmark. Developments on this aspect are
398 ongoing.

399 We provide the one-dimensional cross section limits for different Z' masses keeping the T'
400 mass fixed to 1.2 TeV for the $BR(bW) = 100\%$ hypothesis and the $BR = 60\%bW, 20\%tH, 20\%tZ$

		T' \rightarrow tH signal hypothesis						
Z' mass (TeV)	T' mass (TeV)	Obs. 95% CL limit (pb)	Expected 95% CL limits (pb)					
			-2σ	-1σ	Median	$+1\sigma$	$+2\sigma$	
1.5	0.7	3.5	0.93	1.4	2.1	3.2	5.4	
1.5	0.9	2.6	0.73	1.0	1.5	2.4	4.0	
1.5	1.2	11	2.4	3.5	5.2	8.7	15	
2.0	0.9	0.56	0.37	0.52	0.80	1.3	2.2	
2.0	1.2	0.54	0.34	0.50	0.75	1.2	1.8	
2.0	1.5	0.59	0.43	0.61	0.93	1.5	2.7	
2.5	1.2	0.26	0.22	0.32	0.49	0.78	1.4	
2.5	1.5	0.22	0.21	0.29	0.43	0.68	1.3	

Table 9: Table of expected and observed 95% CL cross section limits, for the T' \rightarrow tH signal hypothesis.

process / nuisance parameter	bkgcorr (gauss)	bkgfit (gauss)	btag (gauss)	jec (gauss)	jer (gauss)	lumi (gauss)	mu (gauss)	pdf (gauss)	pu (gauss)	qcd_rate (gauss)	singletop_rate (gauss)	trigger (gauss)	ttbar_rate (gauss)	wtag (gauss)
qcd	-3.63 ± 2.68 (s)	-0.95 ± 0.95 (s)	---	---	---	---	---	---	---	±50.00 (r)	---	---	---	---
signal_1521_1p5_0p7_1p0_0p0_0p0	+0.65 ± 1.03 (s)	-1.65 ± 4.32 (s)	-0.51 ± 0.30 (s)	±2.70 (r)	±2.70 (r)	±5.80 ± 6.05 (s)	---	---	---	-0.56 ± 0.45 (s)	---	+10.51 ± 11.40 (s)	±3.00 (r)	+3.1 ± 4.70 (s)
signal_1522_1p5_0p9_1p0_0p0_0p0	+0.06 ± 1.74 (s)	-2.37 ± 3.82 (s)	-0.05 ± 1.23 (s)	±2.70 (r)	±2.70 (r)	±4.65 ± 7.18 (s)	---	---	---	-1.11 ± 2.18 (s)	---	+8.26 ± 11.43 (s)	±3.00 (r)	+2.72 ± 5.88 (s)
signal_1523_1p5_1p2_1p0_0p0_0p0	+0.79 ± 0.86 (s)	+1.14 ± 0.86 (s)	-0.76 ± 0.99 (s)	±2.70 (r)	±2.70 (r)	±5.63 ± 6.61 (s)	---	---	---	-0.91 ± 1.03 (s)	---	+10.72 ± 12.39 (s)	±3.00 (r)	+3.31 ± 4.97 (s)
signal_1524_2_1p2_1p0_0p0_0p0	+0.11 ± 1.73 (s)	-1.57 ± 2.72 (s)	-0.42 ± 0.14 (s)	±2.70 (r)	±2.70 (r)	±7.63 ± 7.26 (s)	---	---	---	-0.83 ± 0.15 (s)	---	+13.06 ± 13.65 (s)	±3.00 (r)	+4.14 ± 4.73 (s)
signal_1525_2_1p2_1p0_0p0_0p0	+0.11 ± 1.50 (s)	-1.70 ± 3.36 (s)	-0.49 ± 0.25 (s)	±2.70 (r)	±2.70 (r)	±7.63 ± 7.31 (s)	---	---	---	-1.24 ± 0.72 (s)	---	+11.96 ± 12.64 (s)	±3.00 (r)	+4.20 ± 4.85 (s)
signal_1526_2_1p5_1p0_0p0_0p0	+0.10 ± 1.04 (s)	-1.33 ± 4.83 (s)	-0.98 ± 0.90 (s)	±2.70 (r)	±2.70 (r)	±6.94 ± 7.96 (s)	---	---	---	-1.49 ± 0.66 (s)	---	+11.36 ± 13.35 (s)	±3.00 (r)	+3.33 ± 5.33 (s)
signal_1527_2p5_1p2_1p0_0p0_0p0	+0.12 ± 0.83 (s)	-1.81 ± 2.49 (s)	-0.34 ± 0.17 (s)	±2.70 (r)	±2.70 (r)	±9.12 ± 8.34 (s)	---	---	---	-0.38 ± 0.15 (s)	---	+13.58 ± 14.05 (s)	±3.00 (r)	+4.35 ± 4.83 (s)
signal_1528_205_1p5_1p0_0p0_0p0	+0.12 ± 1.96 (s)	-1.09 ± 2.34 (s)	-0.29 ± 0.14 (s)	±2.70 (r)	±2.70 (r)	±9.24 ± 8.33 (s)	---	---	---	-0.58 ± 0.38 (s)	---	+13.40 ± 13.73 (s)	±3.00 (r)	+4.47 ± 4.85 (s)
singletop	+0.75 ± 1.16 (s)	-1.71 ± 2.34 (s)	-1.26 ± 1.27 (s)	±2.70 (r)	±2.70 (r)	±6.4 ± 7.4 (s)	---	---	---	+0.36 ± 2.17 (s)	---	+10.20 ± 12.73 (s)	±3.00 (r)	+2.49 ± 5.02 (s)
ttbar	+0.88 ± 1.89 (s)	-2.56 ± 6.53 (s)	-0.93 ± 0.95 (s)	±2.70 (r)	±2.70 (r)	±4.38 ± 29.15 (s)	+3.29 ± 29.15 (s)	+0.77 ± 4.98 (s)	+0.77 ± 1.00 (s)	---	---	+10.55 ± 12.24 (s)	±3.00 (r)	+1.23 ± 2.92 (s)
	+0.88 ± 1.89 (s)	-2.56 ± 6.53 (s)	-0.93 ± 0.95 (s)	±2.70 (r)	±2.70 (r)	±4.38 ± 29.15 (s)	+3.29 ± 29.15 (s)	+0.77 ± 4.98 (s)	+0.77 ± 1.00 (s)	---	---	+10.55 ± 12.24 (s)	±3.00 (r)	+1.23 ± 2.92 (s)

process / nuisance parameter	bkgcorr (gauss)	bkgfit (gauss)	btag (gauss)	jec (gauss)	jer (gauss)	lumi (gauss)	mu (gauss)	pdf (gauss)	pu (gauss)	qcd_rate (gauss)	singletop_rate (gauss)	trigger (gauss)	ttbar_rate (gauss)	wtag (gauss)
qcd	+9.01 ± 9.01 (s)	-2.74 ± 1.71 (s)	---	---	---	---	---	---	---	±50.00 (r)	---	---	---	---
signal_1521_1p5_0p7_1p0_0p0_0p0	+0.24 ± 1.23 (s)	-1.51 ± 3.76 (s)	-0.63 ± 0.21 (s)	±2.70 (r)	±2.70 (r)	±5.79 ± 5.94 (s)	---	---	---	-0.34 ± 0.25 (s)	---	+10.62 ± 11.39 (s)	±3.00 (r)	+3.93 ± 4.69 (s)
signal_1522_1p5_0p9_1p0_0p0_0p0	+0.11 ± 1.54 (s)	-2.05 ± 5.42 (s)	-1.37 ± 1.07 (s)	±2.70 (r)	±2.70 (r)	±4.86 ± 6.72 (s)	---	---	---	-1.74 ± 0.72 (s)	---	+8.49 ± 10.97 (s)	±3.00 (r)	+3.18 ± 5.65 (s)
signal_1523_1p5_1p2_1p0_0p0_0p0	+0.12 ± 0.68 (s)	-0.38 ± 0.38 (s)	-0.61 ± 0.98 (s)	±2.70 (r)	±2.70 (r)	±8.60 ± 5.65 (s)	---	---	---	-0.24 ± 1.51 (s)	---	+10.76 ± 12.01 (s)	±3.00 (r)	+3.80 ± 5.25 (s)
signal_1524_2_1p5_1p0_0p0_0p0	+0.14 ± 1.53 (s)	-1.69 ± 2.38 (s)	-0.29 ± 0.17 (s)	±2.70 (r)	±2.70 (r)	±7.67 ± 15.15 (s)	---	---	---	-0.97 ± 0.63 (s)	---	+13.19 ± 13.62 (s)	±3.00 (r)	+4.29 ± 4.72 (s)
signal_1525_2_1p2_1p0_0p0_0p0	+0.14 ± 1.67 (s)	-1.01 ± 2.88 (s)	-0.36 ± 0.17 (s)	±2.70 (r)	±2.70 (r)	±7.58 ± 17.22 (s)	---	---	---	-0.48 ± 0.10 (s)	---	+11.98 ± 12.56 (s)	±3.00 (r)	+4.38 ± 4.96 (s)
signal_1526_2_1p5_1p0_0p0_0p0	+0.13 ± 1.43 (s)	-1.50 ± 2.24 (s)	-1.27 ± 0.81 (s)	±2.70 (r)	±2.70 (r)	±6.78 ± 8.05 (s)	---	---	---	-1.24 ± 0.59 (s)	---	+10.81 ± 13.05 (s)	±3.00 (r)	+3.34 ± 5.78 (s)
signal_1527_205_1p2_1p0_0p0_0p0	+0.15 ± 1.47 (s)	-1.44 ± 2.02 (s)	-0.17 ± 0.10 (s)	±2.70 (r)	±2.70 (r)	±9.17 ± 8.22 (s)	---	---	---	-0.46 ± 0.30 (s)	---	+13.69 ± 14.00 (s)	±3.00 (r)	+4.48 ± 4.78 (s)
singletop	+0.18 ± 1.44 (s)	-1.32 ± 2.40 (s)	-0.25 ± 0.17 (s)	±2.70 (r)	±2.70 (r)	±9.15 ± 8.30 (s)	---	---	---	-0.32 ± 0.07 (s)	---	+13.41 ± 13.82 (s)	±3.00 (r)	+4.49 ± 4.90 (s)
ttbar	+0.19 ± 1.39 (s)	-1.87 ± 2.32 (s)	-0.00 ± 0.23 (s)	±2.70 (r)	±2.70 (r)	±4.42 ± 1.17 (s)	---	---	---	-1.17 ± 0.24 (s)	---	+11.77 ± 11.77 (s)	±3.00 (r)	+4.20 ± 3.30 (s)
	+0.19 ± 1.39 (s)	-1.87 ± 2.32 (s)	-0.00 ± 0.23 (s)	±2.70 (r)	±2.70 (r)	±4.42 ± 1.17 (s)	---	---	---	-1.17 ± 0.24 (s)	---	+10.50 ± 12.34 (s)	±3.00 (r)	+4.48 ± 2.32 (s)

Observable 'allhad1btag'

Observable 'allhad2btag'

Figure 37: Rate impact for every systematic included in the analysis for the $T' \rightarrow bW$ samples. Allhad1btag is the 1 b tag category, Allhad2btag is the 2 b tag category. The naming convention used for the signal is the following signal_signal code - Z' mass in TeV - T' mass in TeV - branching fraction in bW - branching fraction in tZ.

Observable 'allhad1btag'															
process / nuisance parameter	bigcorr (gauss)	bkgfit (gauss)	biax (gauss)	jec (gauss)	jer (gauss)	lumi (gauss)	mu (gauss)	pdf (gauss)	pu (gauss)	qcd_rate (gauss)	singletop_rate (gauss)	toptag (gauss)	trigger (gauss)	tbar_rate (gauss)	wtag (gauss)
qcd	+7.59,-3.68 (s)	-0.96+0.95 (s)	---	---	---	---	---	---	±50.00 (r)	---	---	---	---	---	
signal_81_1p5_0p7_0p0_1p0_0p0	---	---	---	---	---	---	---	---	-1.99,-0.03 (s)	---	---	+0.99,-1.78 (s)	±3.00 (r)	---	
signal_82_1p5_0p9_0p0_1p0_0p0	---	---	---	---	---	---	---	---	-2.14,+0.35 (s)	---	---	+0.43,-1.13 (s)	±3.00 (r)	---	
signal_83_1p5_1p2_0p0_1p0_0p0	---	---	---	---	---	---	---	---	+0.11,-0.33 (s)	---	---	+11.03,-12.03 (s)	±3.00 (r)	---	
signal_84_-2_0p9_0p0_1p0_0p0	---	---	---	---	---	---	---	---	-0.57,-0.05 (s)	---	---	+12.61,-13.37 (s)	±3.00 (r)	---	
signal_85_2_1p2_0p0_1p0_0p0	---	---	---	---	---	---	---	---	+0.29,+0.18 (s)	---	---	+12.34,-12.96 (s)	±3.00 (r)	---	
signal_86_2_1p5_0p0_1p0_0p0	---	---	---	---	---	---	---	---	-1.43,-0.46 (s)	---	---	+12.71,-13.65 (s)	±3.00 (r)	---	
signal_87_2p5_1p2_0p0_1p0_0p0	---	---	---	---	---	---	---	---	-1.41,-0.26 (s)	---	---	+13.47,-13.99 (s)	±3.00 (r)	---	
signal_88_2p5_1p5_0p0_1p0_0p0	---	---	---	---	---	---	---	---	-0.59,-0.00 (s)	---	---	+13.57,-14.04 (s)	±3.00 (r)	---	
singletop	---	---	---	---	---	---	---	---	+0.36,-2.17 (s)	---	---	+0.49,-0.02 (s)	---	---	
tbar	---	---	---	---	---	---	---	---	+0.05,-12.24 (s)	---	---	+1.23,-2.92 (s)	---	---	
Observable 'allhad2btag'															
process / nuisance parameter	bigcorr (gauss)	bkgfit (gauss)	biax (gauss)	jec (gauss)	jer (gauss)	lumi (gauss)	mu (gauss)	pdf (gauss)	pu (gauss)	qcd_rate (gauss)	singletop_rate (gauss)	toptag (gauss)	trigger (gauss)	tbar_rate (gauss)	wtag (gauss)
qcd	+9.01,-9.01 (s)	-2.24,+1.71 (s)	---	---	---	---	---	---	±50.00 (r)	---	---	---	---	---	
signal_81_1p5_0p7_0p0_1p0_0p0	---	---	---	---	---	---	---	---	-0.94,-0.54 (s)	---	---	+0.09,-11.55 (s)	±3.00 (r)	---	
signal_82_1p5_0p9_0p0_1p0_0p0	---	---	---	---	---	---	---	---	-1.49,-0.33 (s)	---	---	+9.42,-11.03 (s)	±3.00 (r)	---	
signal_83_1p5_1p2_0p0_1p0_0p0	---	---	---	---	---	---	---	---	+0.72,-1.63 (s)	---	---	+11.01,-11.98 (s)	±3.00 (r)	---	
signal_84_2_0p9_0p0_1p0_0p0	---	---	---	---	---	---	---	---	-0.44,-0.26 (s)	---	---	+12.47,-13.55 (s)	±3.00 (r)	---	
signal_85_2_1p2_0p0_1p0_0p0	---	---	---	---	---	---	---	---	-0.59,-0.25 (s)	---	---	+12.44,-12.91 (s)	±3.00 (r)	---	
signal_86_2_1p5_0p0_1p0_0p0	---	---	---	---	---	---	---	---	-0.54,-0.38 (s)	---	---	+12.76,-13.71 (s)	±3.00 (r)	---	
signal_87_2p5_1p2_0p0_1p0_0p0	---	---	---	---	---	---	---	---	-0.35,-0.27 (s)	---	---	+13.65,-14.04 (s)	±3.00 (r)	---	
signal_88_2p5_1p5_0p0_1p0_0p0	---	---	---	---	---	---	---	---	-0.59,-0.13 (s)	---	---	+13.59,-13.97 (s)	±3.00 (r)	---	
singletop	---	---	---	---	---	---	---	---	+1.42,-1.17 (s)	---	---	+1.17,-0.24 (s)	---	---	
tbar	---	---	---	---	---	---	---	---	+4.11,-2.77 (s)	---	---	+11.77,-11.77 (s)	±3.00 (r)	---	
	+14.42,-15.05 (s)	-2.22,-5.72 (s)	-1.09,-0.85 (s)	±2.70 (r)	+4.11,-2.77 (s)	+3.14,-4.99 (s)	-1.82,-0.30 (s)	---	+10.50,-12.34 (s)	±3.00 (r)	---	+0.48,-2.32 (s)	±15.00 (r)	---	

Figure 38: Rate impact for every systematic included in the analysis for the $T' \rightarrow tH$ samples. Allhad1btag is the 1 b tag category, Allhad2btag is the 2 b tag category. The naming convention used for the signal is the following signal_signal code - Z' mass in TeV - T' mass in TeV - branching fraction in bW - branching fraction in th - branching fraction in tZ.

Observable 'allhad1btag'														
process / nuisance parameter	bkgcorr (gauss)	bkgfit (gauss)	btag (gauss)	jec (gauss)	ier (gauss)	lumi (gauss)	mu (gauss)	pdf (gauss)	pu (gauss)	qcd_rate (gauss)	singletop_rate (gauss)	trigger (gauss)	ttbar_rate (gauss)	wtag (gauss)
qcd	+3.68 -2.63 (s)	-0.95 -0.93 (s)	±50.00 (r)
signal_1_1p5_0p7_0p0_0p0_1p0	+0.62 -11.91 (s)	-1.64 -7.44 (s)	±0.43 -0.16 (s)	±2.70 (r)	±5.50 -6.40 (s)	-0.90 -0.75 (s)	+0.16 -11.71 (s)	±3.00 (r)
signal_2_1p5_0p9_0p0_0p0_1p0	+9.19 -12.06 (s)	-5.22 -7.70 (s)	±2.12 -1.85 (s)	±2.70 (r)	±4.45 -7.34 (s)	-1.48 -2.06 (s)	-5.29 -11.81 (s)	±3.00 (r)
signal_3_1p5_1p2_0p0_0p0_1p0	+6.61 -10.45 (s)	-3.01 -7.62 (s)	±0.92 -0.78 (s)	±2.70 (r)	±5.74 -6.41 (s)	2.54 +1.28 (s)	+0.48 -11.83 (s)	±3.00 (r)
signal_4_2_0p9_0p0_0p0_1p0	+11.71 -11.49 (s)	-3.55 -3.62 (s)	±0.30 -0.64 (s)	±2.70 (r)	±7.73 -7.25 (s)	-1.59 +1.12 (s)	+1.28 -13.37 (s)	±3.00 (r)
signal_5_2_1p2_0p0_0p0_1p0	+0.89 -11.32 (s)	-4.00 -3.92 (s)	±0.57 -0.44 (s)	±2.70 (r)	±7.40 -7.51 (s)	-0.74 -0.49 (s)	+1.18 -12.99 (s)	±3.00 (r)
signal_6_2_1p5_0p0_0p0_1p0	+0.89 -11.50 (s)	-3.22 -4.57 (s)	±0.71 -0.34 (s)	±2.70 (r)	±7.34 -7.63 (s)	-1.24 -0.07 (s)	+1.24 -13.65 (s)	±3.00 (r)
signal_7_2p5_1p2_0p0_0p0_1p0	+2.27 -11.80 (s)	-3.95 -2.63 (s)	±0.23 -0.10 (s)	±2.70 (r)	±9.26 -8.26 (s)	-0.46 +0.37 (s)	+1.68 -13.96 (s)	±3.00 (r)
signal_8_2p5_1p5_0p0_0p0_1p0	+11.64 -11.98 (s)	-4.23 -2.48 (s)	±0.32 -0.25 (s)	±2.70 (r)	±9.11 -8.47 (s)	-0.67 -0.00 (s)	+1.36 -14.00 (s)	±3.00 (r)
singletop	+9.75 -11.71 (s)	-4.69 -5.01 (s)	±1.26 -1.27 (s)	±2.70 (r)	±2.62 -4.74 (s)	+0.36 -2.17 (s)	+10.20 -12.73 (s)	±3.00 (r)
ttbar	+10.88 -11.89 (s)	-2.56 -6.53 (s)	±0.93 -0.95 (s)	±2.70 (r)	±4.38 -29.15 (s)	±3.29 -4.98 (s)	±0.77 -0.00 (s)	+10.85 -12.24 (s)	±3.00 (r)	+1.23 -2.92 (s)	±15.00 (r)

Observable 'allhad2btag'														
process / nuisance parameter	bkgcorr (gauss)	bkgfit (gauss)	btag (gauss)	jec (gauss)	ier (gauss)	lumi (gauss)	mu (gauss)	pdf (gauss)	pu (gauss)	qcd_rate (gauss)	singletop_rate (gauss)	trigger (gauss)	ttbar_rate (gauss)	wtag (gauss)
qcd	+9.01 -9.01 (s)	-2.24 -1.71 (s)	±50.00 (r)
signal_1_1p5_0p7_0p0_0p0_1p0	+13.98 -14.23 (s)	-3.61 -6.25 (s)	±0.78 -0.73 (s)	±2.70 (r)	±5.50 -6.27 (s)	-2.25 +1.13 (s)	+0.29 -11.69 (s)	±3.00 (r)
signal_2_1p5_0p9_0p0_0p0_1p0	+13.10 -14.54 (s)	-5.11 -5.90 (s)	±1.46 -1.20 (s)	±2.70 (r)	±4.90 -6.81 (s)	-1.63 -1.07 (s)	-0.71 -11.24 (s)	±3.00 (r)
signal_3_1p5_1p2_0p0_0p0_1p0	+12.44 -12.29 (s)	-2.32 -5.47 (s)	±0.49 -0.56 (s)	±2.70 (r)	±5.86 -5.98 (s)	+0.49 -2.23 (s)	+0.71 -11.46 (s)	±3.00 (r)
signal_4_2_0p9_0p0_0p0_1p0	+15.07 -14.59 (s)	-4.41 -2.96 (s)	±0.50 -0.31 (s)	±2.70 (r)	±7.54 -7.32 (s)	-1.42 +0.64 (s)	+1.29 -13.62 (s)	±3.00 (r)
signal_5_2_1p2_0p0_0p0_1p0	+14.59 -14.40 (s)	-3.44 -3.37 (s)	±0.58 -0.40 (s)	±2.70 (r)	±7.37 -7.39 (s)	-0.89 -0.10 (s)	+1.05 -13.02 (s)	±3.00 (r)
signal_6_2_1p5_0p0_0p0_1p0	+14.43 -14.67 (s)	-3.70 -3.26 (s)	±0.63 -0.48 (s)	±2.70 (r)	±7.36 -7.60 (s)	-1.14 -0.06 (s)	+1.38 -13.58 (s)	±3.00 (r)
signal_7_2p5_1p2_0p0_0p0_1p0	+16.23 -15.25 (s)	-4.24 -2.05 (s)	±0.26 -0.12 (s)	±2.70 (r)	±9.14 -8.25 (s)	-0.78 -0.43 (s)	+1.68 -14.04 (s)	±3.00 (r)
signal_8_2p5_1p5_0p0_0p0_1p0	+16.00 -15.10 (s)	-3.62 -2.08 (s)	±0.32 -0.10 (s)	±2.70 (r)	±9.14 -8.31 (s)	-0.80 -0.50 (s)	+1.33 -13.96 (s)	±3.00 (r)
singletop	+13.99 -13.02 (s)	-1.87 -2.52 (s)	±0.00 -0.23 (s)	±2.70 (r)	±1.42 -1.17 (s)	-1.17 +0.24 (s)	+1.17 -11.77 (s)	±3.00 (r)
ttbar	+14.42 -15.06 (s)	-2.22 -6.72 (s)	±1.09 -0.65 (s)	±2.70 (r)	±4.11 -2.74 (s)	±3.14 -4.99 (s)	±1.82 -0.30 (s)	+0.50 -12.34 (s)	±3.00 (r)	+0.48 -2.32 (s)	±15.00 (r)

Figure 39: Rate impact for every systematic included in the analysis for the $T' \rightarrow tZ$ samples. Allhad1btag is the 1 b tag category, Allhad2btag is the 2 b tag category. The naming convention used for the signal is the following: signal_code - Z' mass in TeV - T' mass in TeV - branching fraction in bW - branching fraction in tH - branching fraction in ttZ.

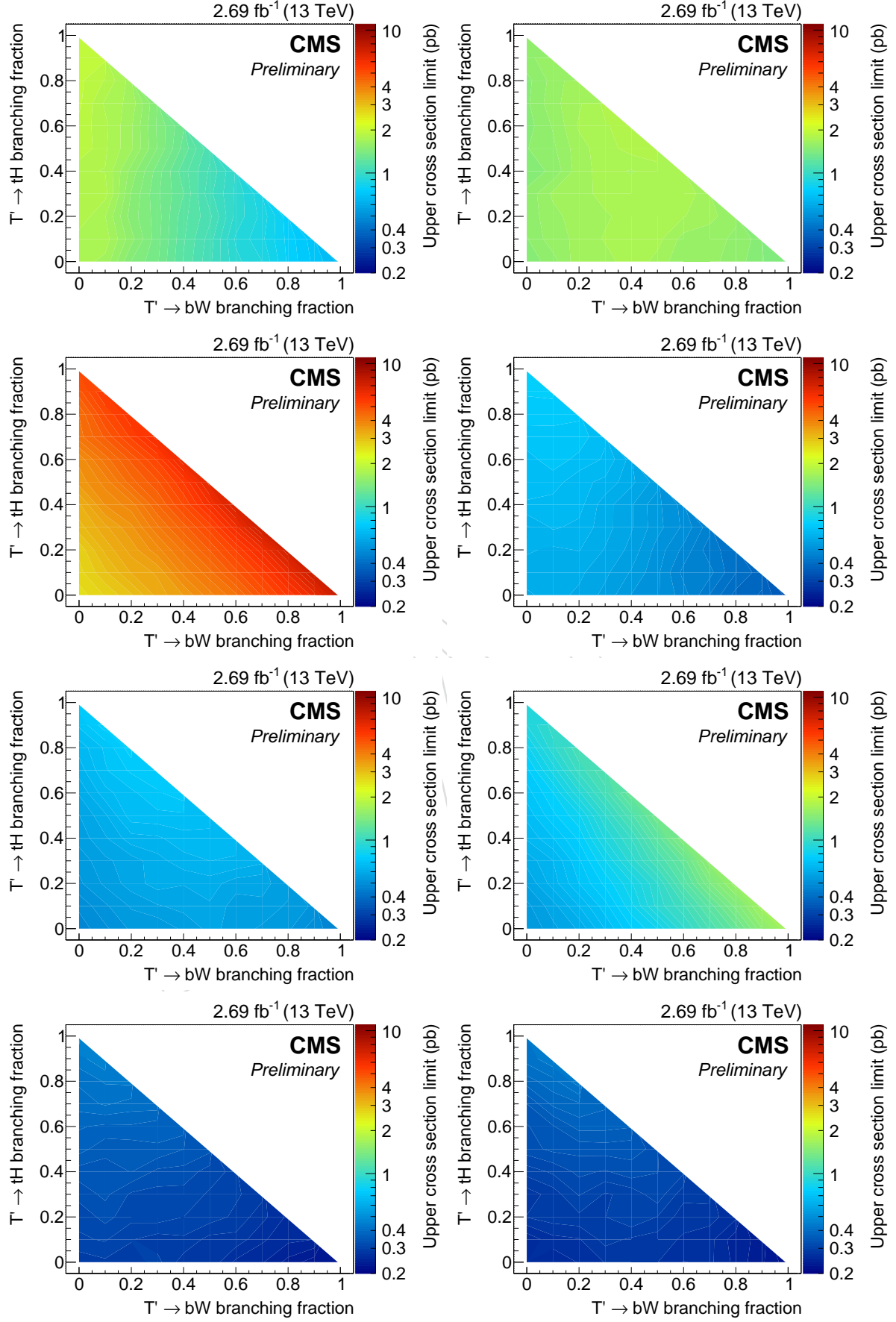


Figure 40: Expected cross section limits for $Z' \rightarrow T't$ for different hypotheses of the Z' mass, the T' mass, and the branching fraction of the T' in bW, tH, tZ .

First row, from left to right: $m_{Z'} = 1.5 \text{ TeV}, m_{T'} = 0.7 \text{ TeV}, m_{Z'} = 1.5 \text{ TeV}, m_{T'} = 0.9 \text{ TeV}$.

Second row, from left to right: $m_{Z'} = 1.5 \text{ TeV}, m_{T'} = 1.2 \text{ TeV}, m_{Z'} = 2.0 \text{ TeV}, m_{T'} = 0.9 \text{ TeV}$.

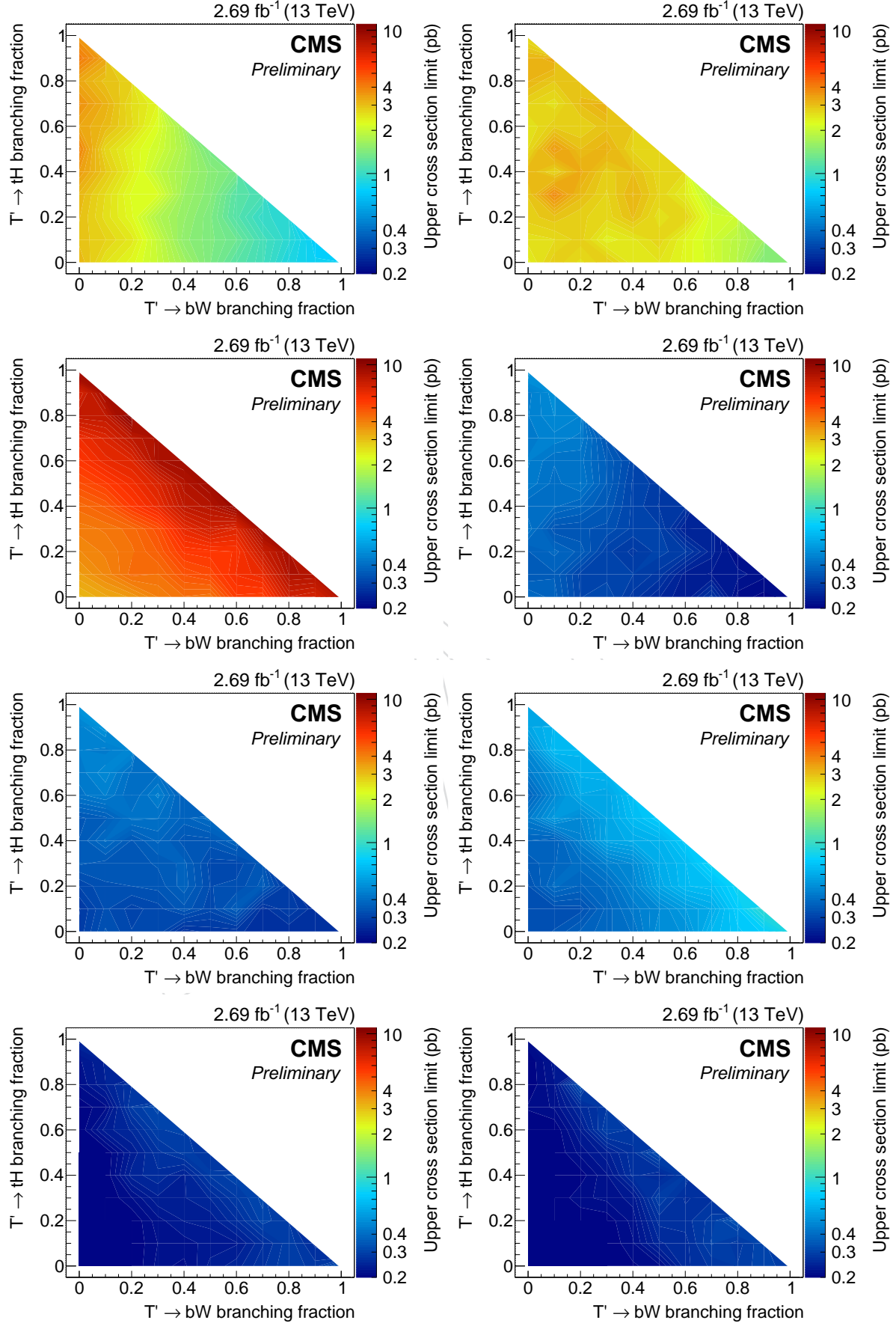


Figure 41: Observed cross section limits for $Z' \rightarrow T't$ for different hypotheses of the Z' mass, the T' mass, and the branching fraction of the T' in bW, tH, tZ .

First row, from left to right: $m_{Z'} = 1.5 \text{ TeV}$, $m_{T'} = 0.7 \text{ TeV}$, $m_{Z'} = 1.5 \text{ TeV}$, $m_{T'} = 0.9 \text{ TeV}$.

Second row, from left to right: $m_{Z'} = 1.5 \text{ TeV}$, $m_{T'} = 1.2 \text{ TeV}$, $m_{Z'} = 2.0 \text{ TeV}$, $m_{T'} = 0.9 \text{ TeV}$

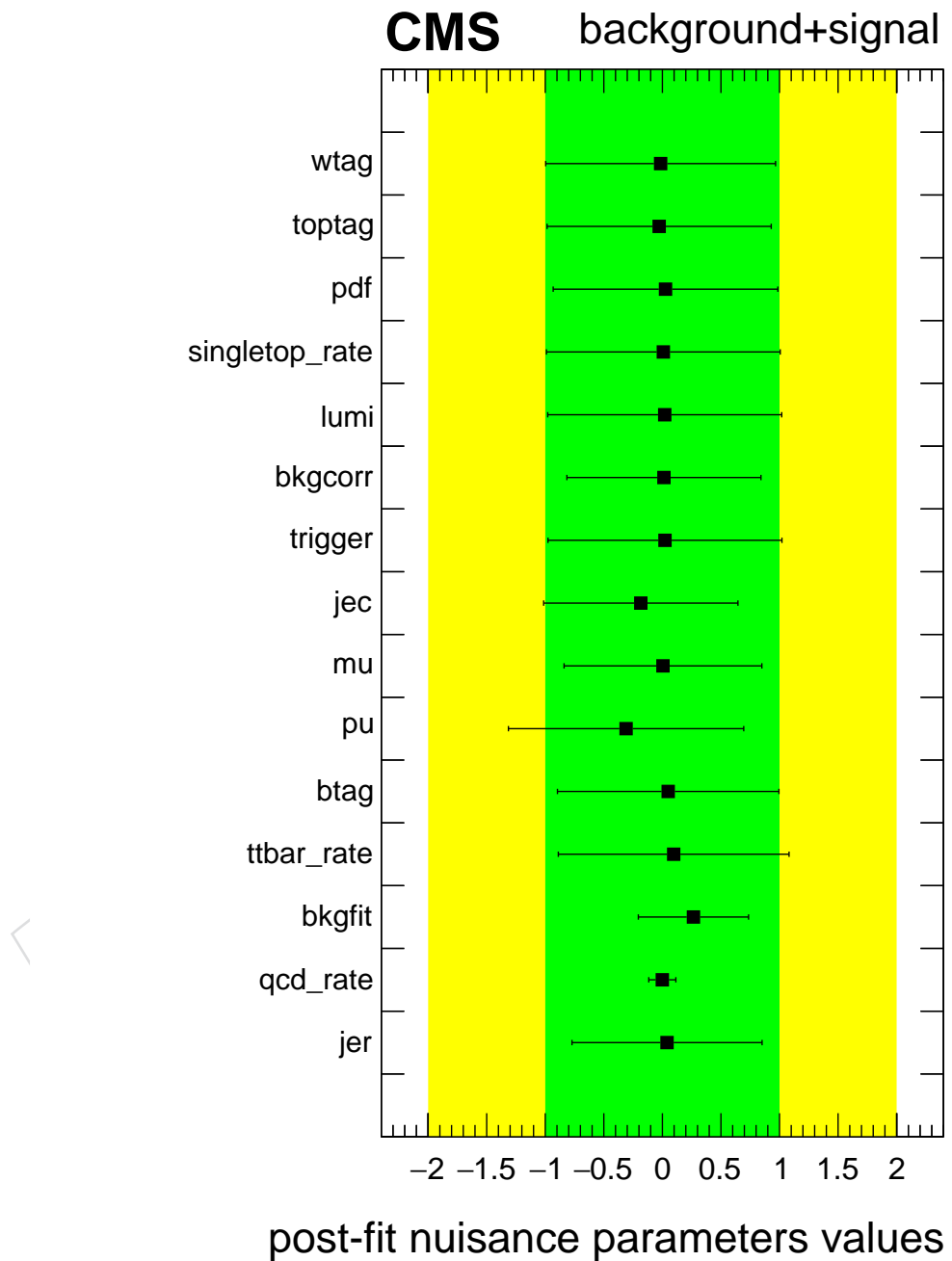


Figure 42: Post-fit nuisance parameters values for the hypothesis of backgorund+signal ($Z'(2TeV) \rightarrow T't, T'(1.2TeV) \rightarrow bW$).

Z' mass (TeV)	T' mass (TeV)	Obs. 95% CL limit (pb)	T' \rightarrow tZ signal hypothesis				
			-2 σ	-1 σ	Median	+1 σ	+2 σ
1.5	0.7	3.1	0.84	1.2	1.7	2.7	4.2
1.5	0.9	2.4	0.67	0.98	1.5	2.3	3.9
1.5	1.2	3.1	1.2	1.7	2.6	4.0	6.1
2.0	0.9	0.40	0.29	0.40	0.59	0.93	1.6
2.0	1.2	0.29	0.23	0.32	0.48	0.74	1.3
2.0	1.5	0.33	0.25	0.34	0.53	0.84	1.3
2.5	1.2	0.18	0.13	0.19	0.29	0.48	0.82
2.5	1.5	0.13	0.12	0.18	0.27	0.43	0.65

Table 10: Table of expected and observed 95% CL cross section limits, for the T' \rightarrow tZ signal hypothesis.

401 hypothesis in Fig 43.

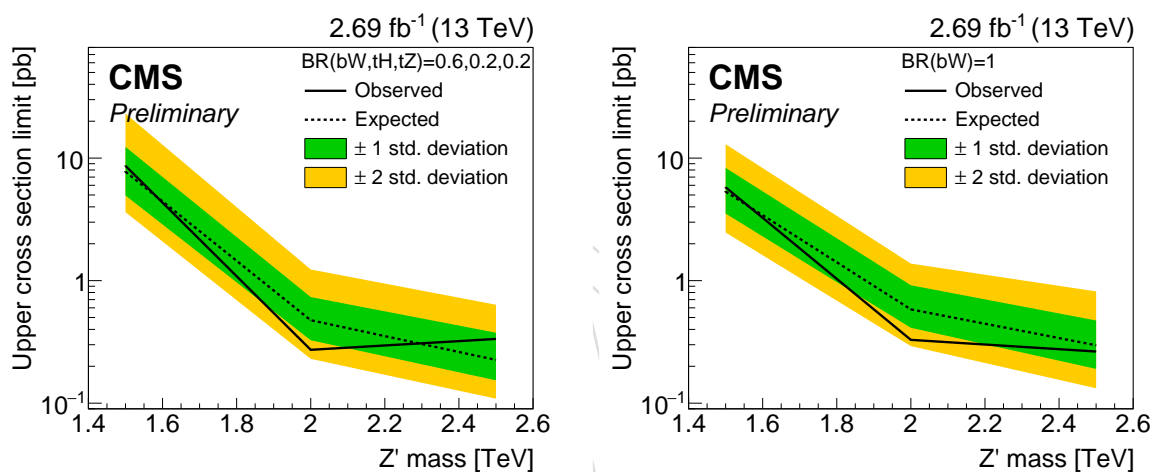


Figure 43: the one-dimensional cross section limits for different Z' masses keeping the T' mass fixed to 1.2 TeV for the $BR(bW) = 100\%$ hypothesis (left) and the $BR = 60\%bW, 20\%tH, 20\%tZ$ hypothesis (right). The continuous line is the observed limit, the dotted line is the expected limit, with the 1 σ (green) and 2 σ (yellow) bands

A Signal region with other signal samples**B Crosschecks**

As a crosscheck we perform the whole background normalization procedure starting from the HT variable rather than $m_{Z'}$, and compare the results with the current procedure. The scale factor for the normalization procedure repeated on the HT variable yields the following results

54.

The differences are smaller than 1% and within the 2.8% MLE fit uncertainty. We repeated the MLE fit in the signal hypothesis, for all the mass points available (bW final state). The difference in the MLE scale factor is minimal, because the fitted signal is very small. The differences with respect to the no signal hypothesis are smaller than 1%. The results can be found here 55.

To make the analysis more solid, in presence of a signal, we increase the QCD normalization prior uncertainty from 2.8% (the MLE fit uncertainty) to 50%. This way the presence of a signal won't affect the QCD normalization in the limit calculation. This change has a negligible effect on the upper expected/observed limits, where the variation is well below 1sigma of the expected limits, as can be seen in the following table 56. This is most likely due to the 1btag category helping in fixing the normalization, while the 2btag category drives the sensitivity.

DRAFT

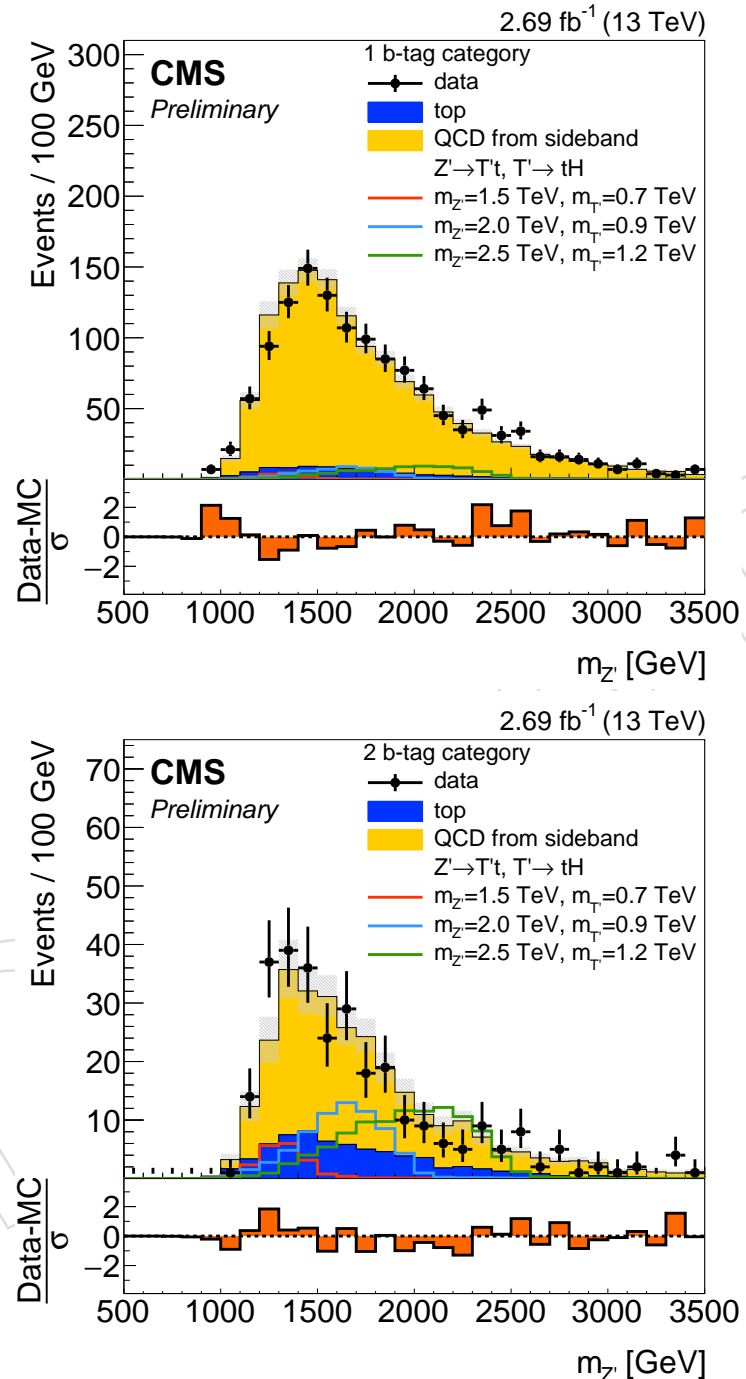


Figure 44: Signal region: invariant mass of the Z' candidate with data-driven non-top background estimate. First row: no subjet btag category, second row: subjet btag category. Signal in the tH final state.

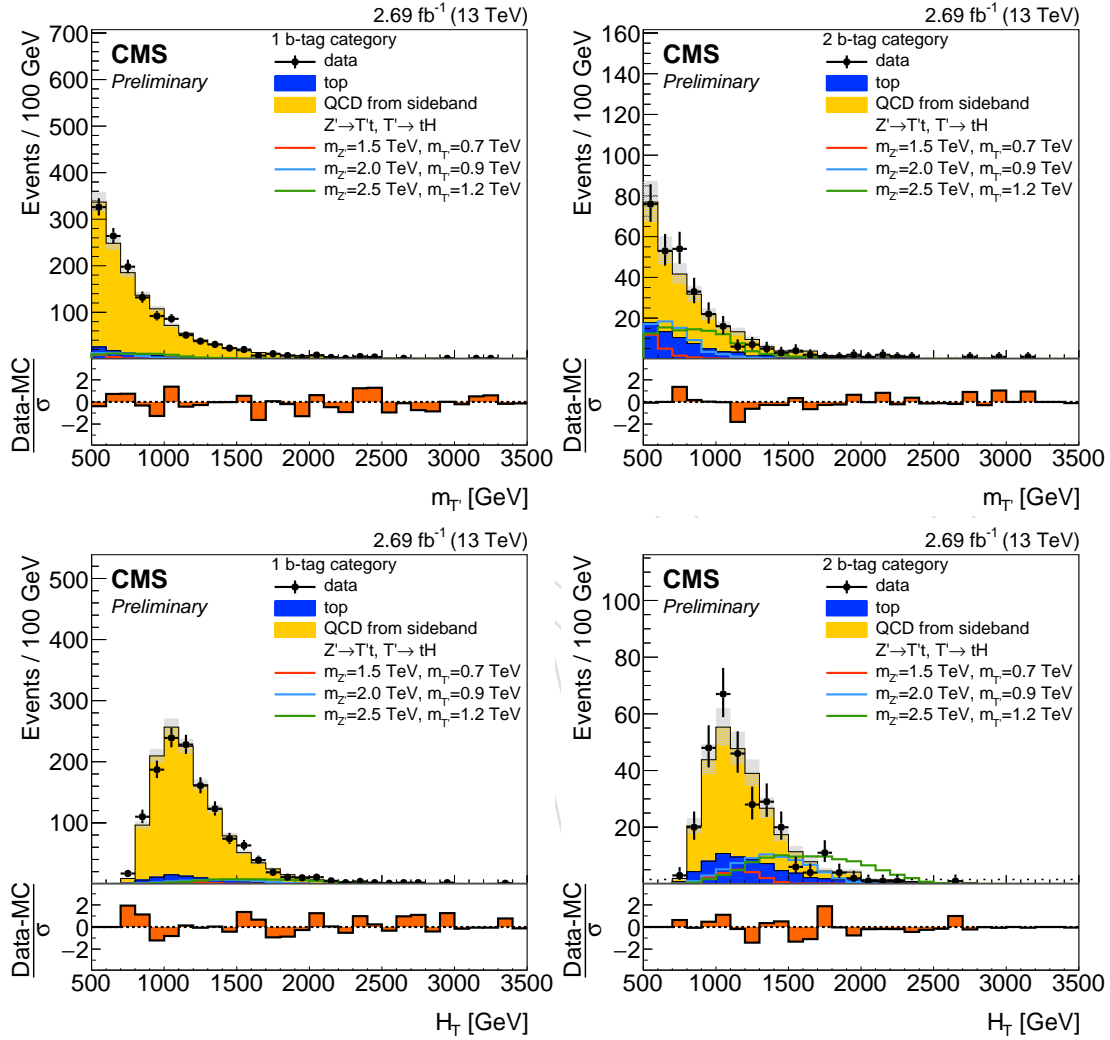


Figure 45: Plots of additional variables in the signal region after the full background estimate procedure: First row: T' candidate invariant mass in the 1 b tag category on the left and the 2 b tag category on the right. Second row: HT calculated as the sum of the p_T of the three jets used in the event in the 1 b tag category on the left and the 2 b tag category on the right. Signal in the tH final state.

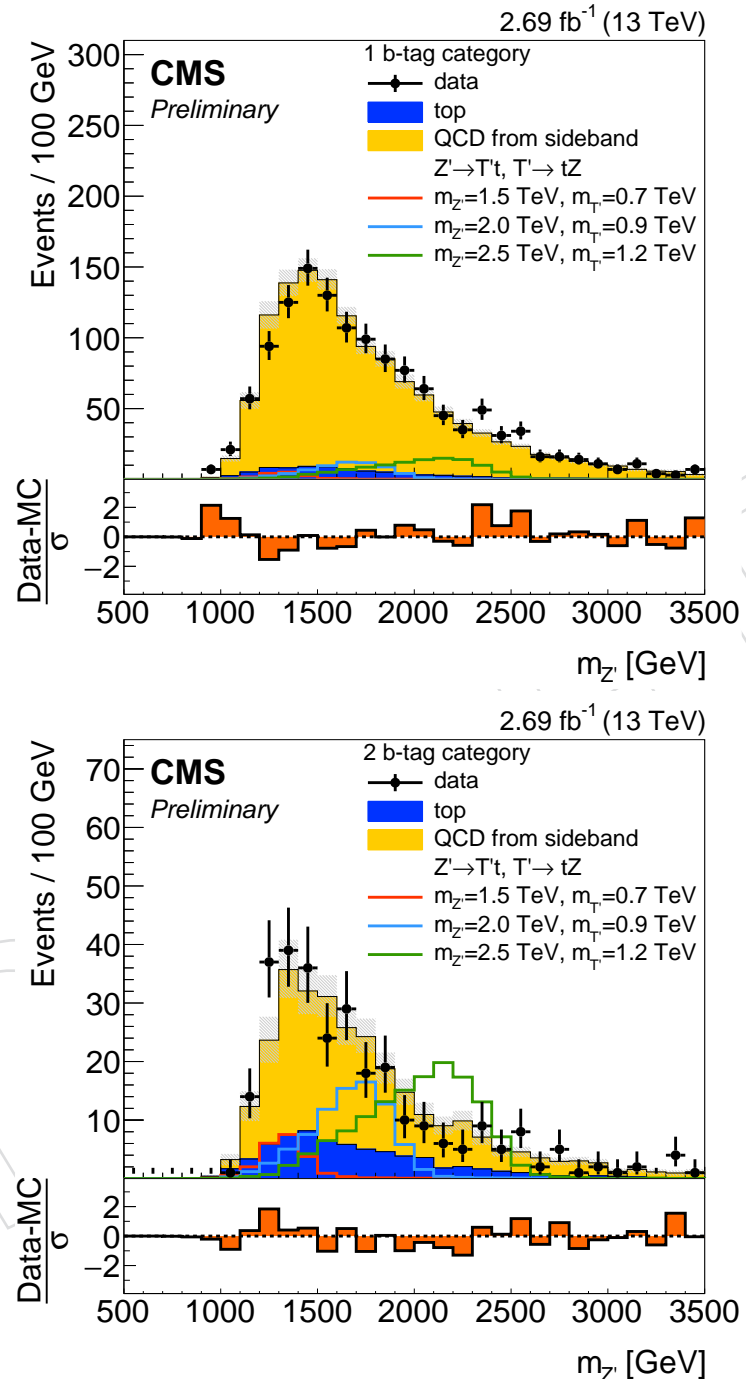


Figure 46: Signal region: invariant mass of the Z' candidate with data-driven non-top background estimate. First row: no subjet btag category, second row: subjet btag category. Signal in the tZ final state.

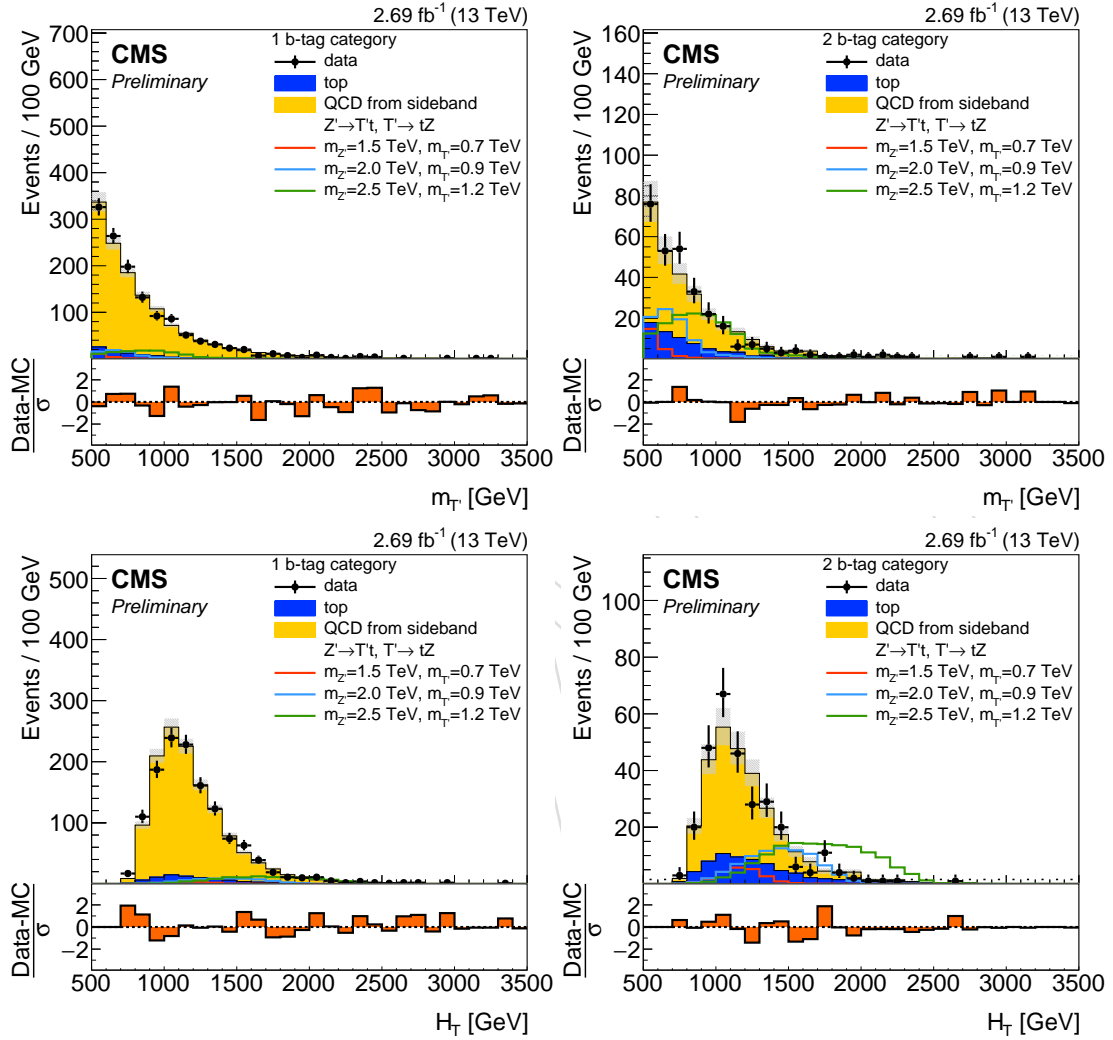


Figure 47: Plots of additional variables in the signal region after the full background estimate procedure: First row: T' candidate invariant mass in the 1 b tag category on the left and the 2 b tag category on the right. Second row: HT calculated as the sum of the p_T of the three jets used in the event in the 1 b tag category on the left and the 2 b tag category on the right. Signal in the tZ final state.

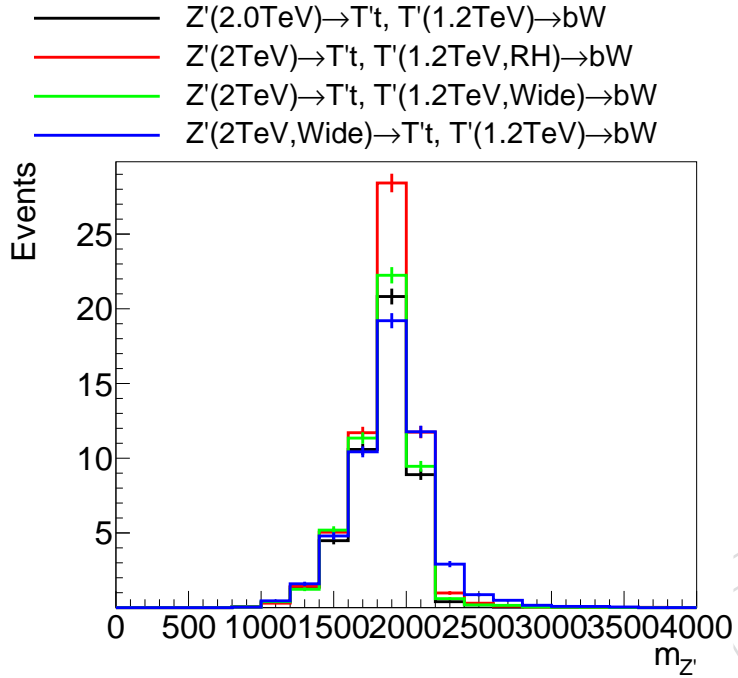


Figure 48: Signal shape for different hypotheses of T' width, Z' width, and T' chirality, bW final state.

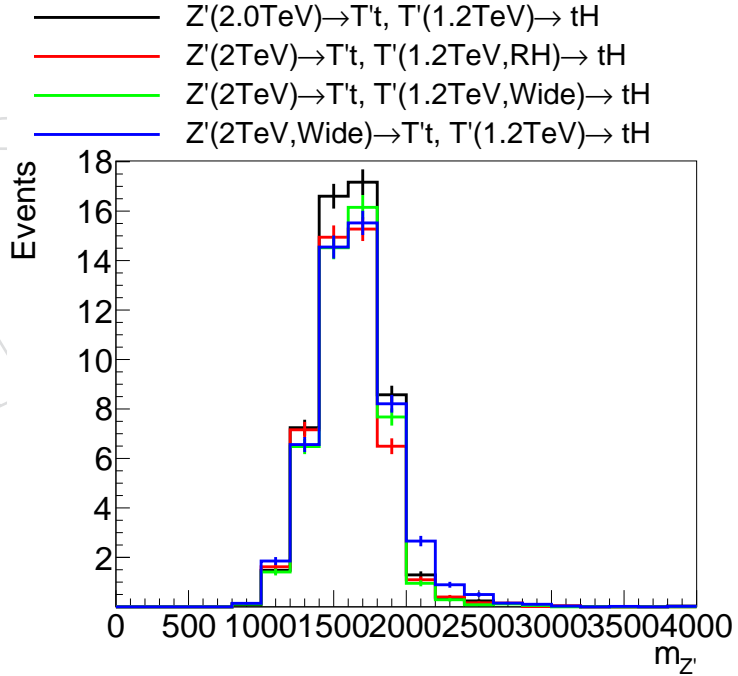


Figure 49: Signal shape for different hypotheses of T' width, Z' width, and T' chirality, tH final state.

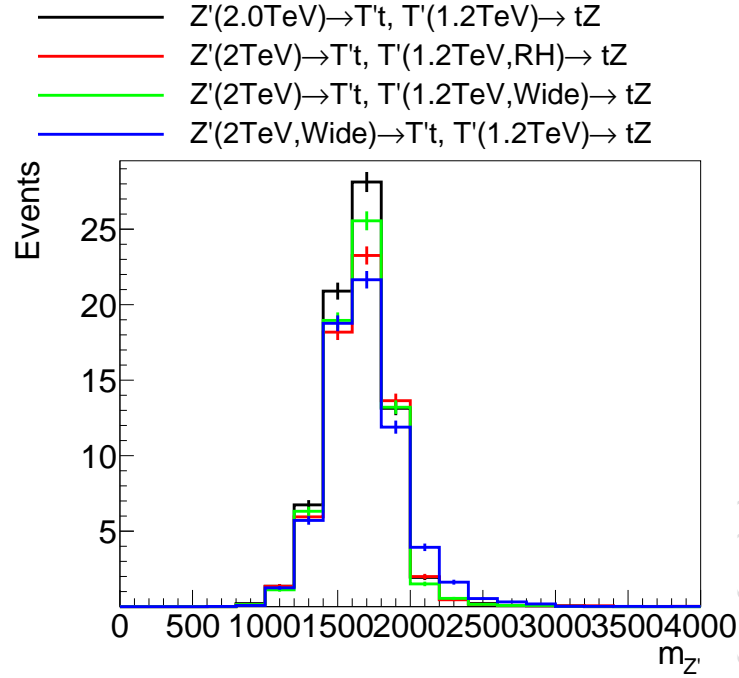


Figure 50: Signal shape for different hypotheses of T' width, Z' width, and T' chirality, tZ final state.

signal process	expected limit	expected limit (central 1sigma)	expected limit (central 2sigma)	observed limit
716	0.675	0.471--0.997	0.348--1.48	0.741 +- 0.0245
717	1.34	0.92--2.09	0.675--3.17	1.38 +- 0.0688
718	7.78	5.31--11.9	3.57--20.7	8.38 +- 0.0661
719	0.35	0.238--0.536	0.171--0.914	0.194 +- 0.00693
720 T' LH	0.47	0.329--0.733	0.24--1.12	0.299 +- 0.00584
721 T' RH	0.336	0.236--0.519	0.174--0.832	0.188 +- 0.00316
722 T' wide	0.466	0.322--0.714	0.228--1.18	0.251 +- 0.00685
723	1.77	1.18--2.76	0.88--4.46	0.879 +- 0.0401
724 Z' wide	0.533	0.348--0.821	0.257--1.29	0.258 +- 0.00308
725	0.215	0.149--0.334	0.102--0.517	0.249 +- 0.00594
726	0.216	0.151--0.318	0.106--0.514	0.263 +- 0.00926

Figure 51: Impact on limits different hypotheses of T' width, Z' width, and T' chirality, bW final state.

$Z'(2 \text{ TeV}) \rightarrow T'(1.2 \text{ TeV})t, T' \rightarrow tH$

signal process	expected limit	expected limit (central 1sigma)	expected limit (central 2sigma)	observed limit
111	1.99	1.35--3.12	0.939--5.01	4.06 +- 0.229
112	1.45	0.991--2.24	0.719--3.66	2.91 +- 0.155
113	5.3	3.46--8.52	2.51--14.5	12.7 +- 1.12
114	0.796	0.543--1.17	0.4--1.97	0.532 +- 0.0143
115 T' LH	0.747	0.501--1.14	0.377--1.88	0.608 +- 0.0436
116 T' RH	0.82	0.558--1.3	0.417--2.09	0.672 +- 0.0236
117 T' wide	0.791	0.563--1.29	0.417--2.12	0.625 +- 0.0194
118	0.933	0.636--1.48	0.461--2.46	0.595 +- 0.0217
119 Z' wide	0.86	0.574--1.35	0.418--2.28	0.656 +- 0.0284
120	0.478	0.32--0.756	0.225--1.21	0.23 +- 0.0139
121	0.442	0.3--0.676	0.222--1.13	0.213 +- 0.00245

Figure 52: Impact on limits different hypotheses of T' width, Z' width, and T' chirality, tH final state.

$Z'(2 \text{ TeV}) \rightarrow T'(1.2 \text{ TeV})t, T' \rightarrow tZ$

signal process	expected limit	expected limit (central 1sigma)	expected limit (central 2sigma)	observed limit
1	1.77	1.22--2.64	0.886--4.1	2.7 +- 0.269
2	1.49	1.01--2.24	0.757--3.65	2.57 +- 0.107
3	2.6	1.77--3.76	1.28--5.83	3.88 +- 0.168
4	0.587	0.399--0.883	0.293--1.41	0.339 +- 0.0114
5 T' LH	0.474	0.331--0.709	0.237--1.09	0.299 +- 0.00981
6 T' RH	0.553	0.388--0.82	0.273--1.29	0.325 +- 0.0229
7 T' wide	0.495	0.354--0.759	0.261--1.16	0.323 +- 0.016
8	0.512	0.347--0.772	0.243--1.22	0.327 +- 0.0207
9 Z' wide	0.624	0.419--0.959	0.321--1.47	0.37 +- 0.0275
10	0.292	0.192--0.452	0.145--0.767	0.171 +- 0.00293
11	0.252	0.176--0.391	0.125--0.62	0.136 +- 0.00245

Figure 53: Impact on limits different hypotheses of T' width, Z' width, and T' chirality, tZ final state.

	integral norm SF	MLE SF	total SF	diff in %
1btag mZ'	0,0934509126798	0,996022971801	0,093079255764850	0,460604615955876
2btag mZ'	0,124318746802	0,996022971801	0,123824327640304	-0,726937264255567
1btag HT	0,0925645406825	1,00092894896	0,092650528416299	
2btag HT	0,1246086977	1,00092894896	0,124724452820135	

Figure 54: Normalization SF comparison when calculated using HT or the mass of the Z' candidate.

mass of Z'	mass of T'	MLE SF	diff wrt no signal in %
1,5	0,7	0,998843660679	0,28319516294887
2	1,2	0,999723508279	0,371531238010383
2,5	1,5	1,00095028926	0,494699178482848
1,5	1,2	0,997776703324	0,176073401181589
2	0,9	0,999733282035	0,372512516181337
2	1,5	0,999719840768	0,371163022506942
1,5	0,9	0,998814818564	0,280299435057391
2,5	1,2	1,00051149185	0,450644229709273

Figure 55: Normalization SF in the hypothesis of a signal in the MLE fit.

m Z'	100% bW m T'	2.8% qcd norm prior obs limit	50% qcd norm prior obs limit	2.8% qcd norm prior exp limit	50% qcd norm prior exp limit	2.8% qcd norm prior -1sigma	2.8% qcd norm prior +1sigma	50% qcd norm prior -1sigma	50% qcd norm prior +1sigma
1500	700	0,73	0,72	0,64	0,65	0,45	0,96	0,43	1,01
1500	900	1,50	1,43	1,32	1,35	0,91	2,02	0,87	2,15
1500	1200	9,91	9,11	7,53	7,68	5,14	11,54	5,00	12,22
2000	900	0,19	0,19	0,34	0,35	0,24	0,51	0,23	0,54
2000	1200	0,26	0,25	0,48	0,48	0,32	0,73	0,33	0,77
2000	1500	0,89	0,94	1,75	1,76	1,20	2,80	1,16	2,77
2500	1200	0,29	0,25	0,22	0,23	0,14	0,33	0,15	0,36
2500	1500	0,28	0,31	0,22	0,22	0,15	0,33	0,14	0,36

Figure 56: Comparison of limits when the QCD normalization prior uncertainty is changed from 2.8% to 50%.

References

- [1] J. A. Aguilar-Saavedra, R. Benbrik, S. Heinemeyer, and M. Pérez-Victoria, “Handbook of vector-like quarks: mixing and single production”, *Phys. Rev. D* **88** (2013) 094010, doi:10.1103/PhysRevD.88.094010, arXiv:1306.0572.
- [2] CMS Collaboration, “Search for Vectorlike Charge 2/3 T Quarks in Proton-Proton Collisions at $\sqrt{s} = 8$ TeV”, *Phys. Rev. D* **93** (2016), no. 1, 012003, doi:10.1103/PhysRevD.93.012003, arXiv:1509.04177.
- [3] ATLAS Collaboration, “Search for pair and single production of new heavy quarks that decay to a Z boson and a third-generation quark in pp collisions at $\sqrt{s} = 8$ TeV with the ATLAS detector”, *JHEP* **11** (2014) 104, doi:10.1007/JHEP11(2014)104, arXiv:1409.5500.
- [4] ATLAS Collaboration, “Analysis of events with b-jets and a pair of leptons of the same charge in pp collisions at $\sqrt{s} = 8$ TeV with the ATLAS detector”, (2015). arXiv:1504.04605. Accepted by *JHEP* (2015).
- [5] ATLAS Collaboration, “Search for production of vector-like quark pairs and of four top quarks in the lepton-plus-jets final state in pp collisions at $\sqrt{s} = 8$ TeV with the ATLAS detector”, *JHEP* **08** (2015) 105, doi:10.1007/JHEP08(2015)105, arXiv:1505.04306.
- [6] J. Alwall et al., “The automated computation of tree-level and next-to-leading order differential cross sections, and their matching to parton shower simulations”, *JHEP* **07** (2014) 079, doi:10.1007/JHEP07(2014)079, arXiv:1405.0301.
- [7] D. Greco and D. Liu, “Hunting composite vector resonances at the LHC: naturalness facing data”, *Journal of High Energy Physics* **2014** (2014), no. 12, 1–50, doi:10.1007/JHEP12(2014)126.

- 442 [8] P. Artoisenet, R. Frederix, O. Mattelaer, and R. Rietkerk, “Automatic spin-entangled
443 decays of heavy resonances in Monte Carlo simulations”, *Journal of High Energy Physics*
444 **2013** (2013), no. 3, 1–19, doi:10.1007/JHEP03(2013)015.
- 445 [9] T. Sjöstrand et al., “An Introduction to PYTHIA 8.2”, *Comput. Phys. Commun.* **191** (2015)
446 159–177, doi:10.1016/j.cpc.2015.01.024, arXiv:1410.3012.
- 447 [10] M. L. Mangano, M. Moretti, F. Piccinini, and M. Treccani, “Matching Matrix Elements
448 and Shower Evolution for Top-Quark Production in Hadronic Collisions”, *JHEP* **01**
449 (2007) 013.
- 450 [11] The CMS Collaboration, “b-Tagging Offline Guide”, technical report, CERN, 2014.
- 451 [12] The CMS collaboration, “Identification of b-quark jets with the CMS experiment”,
452 *Journal of Instrumentation* **8** (2013), no. 04, P04013.
- 453 [13] CMS Collaboration, “Identification of b quark jets at the CMS Experiment in the LHC
454 Run 2”, CMS Physics Analysis Summary CMS-PAS-BTV-15-001, CERN, 2016.

DRAFT